Probing the intracluster medium at high angular resolution via radio-interferometric measurements of the Sunyaev-Zeldovich effect

Luca Di Mascolo

München 2020

Probing the intracluster medium at high angular resolution via radio-interferometric measurements of the Sunyaev-Zeldovich effect

Luca Di Mascolo

Dissertation
an der Fakultät für Physik
der Ludwig–Maximilians–Universität
München

vorgelegt von
Luca Di Mascolo
aus Fondi, Italy

München, den 1 April 2020

Erstgutachter: Prof. Dr. Rashid Sunyaev
Zweitgutachter: Dr. Klaus Dolag
Tag der mündlichen Prüfung: 28 Mai 2020

Contents

List of Figures

List of Tables

List of Abbreviations

ACA	Atacama Compact (Morita) Array
ACT	Atacama Cosmology Telescope
ALMA	Atacama Large Millimeter/Submillimeter Array
AMI	Arcminute MIcroKelvin Interferometer
AMiBA	Array for Microwave Background Anisotropy
BCG	Brightest Cluster Galaxy
BIMA	Berkeley-Illinois-Maryland Array
CARMA	Combined ARray for Millimeter-wave Astronomy
CMB	Cosmic Microwave Background
Dec	Declination
eROSITA	Extended ROentgen Survey with an Imaging Telescope Array
FIRST	Faint Images of the Radio Sky at Twenty-Centimeters
gNFW	Generalized Navarro-Frenk-White
MaDCoWS	Massive and Distant Clusters of WISE Survey
NVSS	NRAO VLA Sky Survey
MRS	Maximum Recoverable Scale
OVRO	Owens Valley Radio Observatory
RA	Right Ascension
RMS	Root Mean Square
SPT	South Pole Telescope
SRG	Spectrum-Roentgen-Gamma
SZ	Sunyaev-Zeldovich effect
SZA	Sunyaev-Zeldovich Array
VACA LoCA	Verification with the ACA: Localisation and Cluster Analysis
VLA	Very Large Array
VLASS	Very Large Array Sky Survey

Zusammenfassung

Die in dieser Dissertation präsentierte Arbeit widmet sich der Untersuchung der Physik von Galaxienhaufen mithilfe der Charakterisierung des Sunyaev-Zeldovich (SZ) Effekts in Beobachtung mit dem *Atacama Large Millimeter/Submillimeter Array (ALMA)* und dem *Atacama Compact Array (ACA)*. Die beispiellosen Fähigkeiten von ALMA+ACA haben dem Studium der Physik des Mediums innerhalb von Galaxienhaufen ein Fenster im Millimeter WellenLängenbereich eröffnet. Die bahnbrechenden Beobachtungen des SZ Effekts auf Skalen von einigen Winkelsekunden haben gezeigt, dass ALMA+ACA effektiv ein neues Beobachtungswerkzeug bereitstellen können, welches komplementär zu den eher traditionellen Beobachtungen von Röntgenlicht ist, da dazu verwendet werden kann, den physikalischen und thermodynamischen Zustand des Mediums in Galaxienhaufen bis auf die kleinsten physikalischen Skalen zu testen.

Von zentraler Bedeutung für den Einsatz von ALMA zur Abbildung von SZ Strukturen ist die herausragende Sensitivität und bisher unerreichte Winkelauflösung. Allerdings besitzt ALMA bisher noch keine Sensitivität für Signale, welche sich auf Skalen größer als 1-2 Winkelminuten erstrecken, da die Information über deren Präsenz durch die Verwendung von Interfermotrie stark heraus gefiltert wird. In der tat besitzen Messungen von Signalen durch Radio-interferometrie nur diejenigen Winkelskalen, welche den inversen Längen von individuellen Basislinien innerhalb des Arrays entsprechen. Daraus folgt, dass das Antennen Paar mit dem kleinsten Abstand innerhalb des Interferometers ein definitive obere Grenze für die maximal rekonstruierbare Größenskala in einer Beobachtung darstellt. Da sich die Größenskalen von Galaxienhaufen Längen erstrecken, welche über das Blickgeld von ALMA hinausgehen, verhalten sich SZ Signaturen als wären sie mit durch einen Hochpassfilter geschickt worden. Dementsprechend ist sowohl die richtige Interpretation der rekonstruierten Bilder als auch die Analyse von Rohdaten nicht trivial.

Die Herausforderung, dass ALMA Beobachtungen grundlegend die größten Skalen heraus filtern, verlangt weitere komplementäre Daten/Informationen von hoch aufgelösten ALMA Messungen mit einander zu kombinieren. Eine Möglichkeit mit der fehlenden Information auf grossen Skalen umzugehen ist es, die SZ Messungen von einer einzelnen Teleskop-Einrichtung zu betrachten. Tatsächlich haben diese Messungen im allgemeinen kleinere Winkelauflösungen als deren radio-interferometrie Äquivalent, jedoch können sie hinreichend grosse Skalen rekonstruieren und sind damit in der Lage den gesamten SZ Stahlungsfluss eines Galaxienhaufens zu bestimmen. Die Rekonstruktion des SZ signals aus der gemeinsamen analyse von Radio-interferometrischen und einzelnen Beobachtungen kann deshalb dazu verwendet werden, sowohl Einsichten in den physikalischen Zustand der kleinskaligen Struktur innerhalb von des Galaxienhaufen-Mediums zu erhalten, als auch global dessen Eigenschaften zu bestimmen. Die grosse Verfügbarkeit

von SZ Messungen des bekannten Galaxienhaufens RX J1347.5–1145 stellt die Möglichkeit für eine solche gleichzeitige Modellierung bereit. Gegeben, dass der SZ Effekt Information über die Elektronen-Druckverteilung innerhalb eines Galaxienhaufens entlang der Sichtlinie bereitstellt, erlaubte die Studie ein Modell der Druckverhältnisse innerhalb des Haufens auf bisher unerreichten Längenskalen zu erhalten. Durch den Vergleich mit Analysen von Messungen im RöntgenwellenLängenbereich, erlaubte dies sowohl neue Einsichten in die thermodynamischen Eigenschaften von RX J1347.5–1145 als auch dessen Entstehungsgeschichte.

Die Kombination aus SZ Daten und Röntgenbeobachtungen ist erkenntlicherweise von zentraler Bedeutung fur eine robuste Beschreibung des Gases und der Strukturen innerhalb eines Galaxienhaufens, welche wiederum Rückschlüsse auf die dynamische Natur des Haufens zulassen. Insbesondere kann eine gemeinsame Betrachtung von hochaufgelösten SZ und Röntgenbeobachtungen eines Schocks innerhalb innerhalb von Galaxienhaufen dabei helfen, sowohl mehrere fundamentale Plasma Eigenschaften (und damit Plasmaphysik an sich), als auch im weiteren Kontext die Eigenschaften von astrophysikalischen Prozessen einzugrenzen, wie z.B. die Entwicklung von Galaxien und deren Haufen, oder den Einfluss von Akkretionsprozessen in der näheren Umgebung. Vielerseits gilt der bogenförmige Schock im sogenannten Bullet Cluster (1E0657-56) als das "Textbuch Beispiel" eines Idealfalls für eine SZ Studie. Die Rekonstruktion der Schock Eigenschaften erlaubte hier insbesondere die möglichen Erhitzungsmechanismen von Elektronen innerhalb des Schocks zu bestimmen.

Letztendlich können ALMA+ACA als eine mächtige Kombination zur direkten und relativ günstigen Bestätigung bei der Identifikation von Galaxienhaufen dienen, welche über andere Mittel (wie z.B. Weitfeld Studien in anderen WellenLängen or CMB experimenten) beobachtet wurden, insbesondere durch die Messung derer SZ Signale. Obwohl ALMAs Abbildungsgeschwindigkeit signifikant kleiner ist als die von Experimenten zur Erhebung von SZ Strukturen, erlauben einem die Winkelauflösung und Sensitivität von ALMA doch eine einfache Messung des SZ Effekts in Systemen mit hoher Rotverschiebung. Die erst Pilotstudie einer Galaxienhaufen Stichprobe des VACA LoCA (engl. für "*Verification with the Atacama Compact Array – Localisation and Cluster Analysis*") erlaubte bereits eine erste Beurteilung von ACA Fähigkeiten eine robuste Detektion von Galaxienhaufen mit hoher Rotverschiebung samt Massenbestimmungen durchzuführen.

Abstract

The work presented in this thesis is devoted to investigating the physics of galaxy clusters through the characterization of their Sunyaev-Zeldovich (SZ) effect signal observed by the Atacama Large Millimeter/Submillimeter Array (ALMA) and the Atacama Compact Array (ACA). The unparalleled capabilities of ALMA+ACA have definitely opened a millimeter-wave window on the physics of the intracluster medium. The pioneering observations of the SZ effect over scales of a few arcseconds demonstrated that ALMA+ACA can effectively provide a new observational tool, complementary to the more traditional X-ray observations, for probing the physical and thermodynamic state of the intracluster medium down to the smallest physical scales.

Central for employing ALMA+ACA to map SZ structures are its outstanding sensitivity and angular resolving power. However, ALMA+ACA currently offers no sensitivity to any signal extending on scales larger than 1-2 arcminutes, as such information is severely filtered out through the interferometric response. A radio-interferometer can in fact provide measurements of signals with angular sizes solely corresponding to the inverse of the lengths of the individual baselines within the array. It follows that the pair of antennae at the smallest distance within an interferometer poses a hard limit on the maximum scale recoverable in a given observation. As galaxy clusters cover scales often larger than the field of view of ALMA, the result is a heavily high-pass filtered view of their SZ signature. In turn, both the proper interpretation of the reconstructed images and the analysis of the raw data become non trivial.

To overcome the issue related to the large-scale filtering effect inherent to ALMA, it is key to combine the high-resolution ALMA+ACA measurements with complementary data or information. One possibility to tackle the lack of information on large scales is to consider SZ measurements from single-dish facilities. In fact, single-dish measurements generally have angular resolutions lower than radio-interferometric ones, but can recover sufficiently large angular scales to constrain the total SZ flux from a galaxy cluster. The reconstruction of the SZ signal from the joint analysis of radio-interferometric and single observations can thus be used to get insights into the physical state of small-scale structures within the intracluster medium as well as its global properties. The rich availability of SZ measurements of the renowned galaxy cluster RX J1347.5–1145 offered the opportunity to test such joint modelling approach. As the SZ effect provides information on the line-of-sight integral of the electron pressure distribution within a cluster, the joint study allowed to get a model of the intracluster pressure over an outstanding range of scales. Through the comparison with an independent analysis of X-ray measurements, this allowed for gaining novel insight into the thermodynamic properties of RX J1347.5–1145, as well as its formation history.

The combination of SZ data with X-ray information is clearly central for obtaining a robust description of the intracluster gas and of any intracluster structures that attest to the dynamical nature of galaxy clusters. In particular, a joint SZ+X-ray high-resolution view of the shock fronts within galaxy clusters can help constraining a number of plasma properties fundamental to plasma physics on its own, as well as in the broader context of astrophysical processes, e.g., cluster and galaxy evolution, and the impact of merger and accretion processes of the cluster environment. Widely regarded as the "textbook example" of a cluster merger bow shock, the shock front in the "Bullet Cluster" (1E0657-56) represented the ideal test case for such an SZ study. The reconstruction of the shock properties specifically allowed for inferring the possible electron heating mechanisms taking place within the shocked gas.

Finally, ALMA+ACA can serve as a powerful combination for providing direct and relatively inexpensive confirmation of galaxy clusters identified by other means (e.g., wide-field surveys at other wavelengths or with cosmic microwave background experiments) through the measure of their SZ signal. Although ALMA and ACA's mapping speeds are significantly lower than that of a SZ survey experiment, the angular resolution and sensitivity of ALMA+ACA allow one to easily measure the SZ effect from high-redshift systems. The study of a first pilot sample of galaxy cluster from the "*Verification with the Atacama Compact Array – Localisation and Cluster Analysis*" programme provided a first assessment of ACA's ability to get robust detections of high-redshift galaxy clusters and constraints on their masses.

Chapter 1

Introduction

The large-scale cosmic structures we observe today originate from the inexorable gravitational collapse of over-dense regions in our Universe (Peebles 1980). The current paradigm (Bond et al. 1996) states that the mass assembly of any astronomical systems begins as a consequence of the gravitational instability of density fluctuations arising during the inflationary expansion of the early Universe (Mukhanov 2005). These perturbations in the primordial density field represent the seeds for the subsequent hierarchical formation of the cosmic structures (Gott & Rees 1975, Press & Schechter 1974, White & Rees 1978, White & Frenk 1991). In this scenario, a sequence of merger episodes between smaller-scale structures and accretion processes of surrounding matter leads the distribution of matter in the Universe to arrange along a large-scale filamentary structure — the cosmic web (Shandarin & Zeldovich 1989, Bond et al. 1996, Kravtsov & Borgani 2012).

Sat at the intersections of cosmic web filaments are galaxy clusters, representing the very final stage of cosmic structure formation. With total masses ranging between 10^{14} and 10^{15} $M_{\odot}$ and extending over scales of few megaparsecs, they are the largest gravitationally bound objects ever formed across cosmic time. Despite the name, the cool baryonic matter in the form of stars within the thousands of cluster galaxies is however only a minor fraction ($\sim$ 3%) of the total matter content of a galaxy cluster. This is in fact dominated by collisionless dark matter ($\sim$ 85%; White et al. 1993), whose gravitational field provides the main driver to the non-linear evolution of large-scale structures. The rest ($\sim$ 12%) is composed of diffuse baryonic gas, the intracluster medium, permeating the entire space between the cluster galaxies. In the absence of non-gravitational processes able to deplete galaxy clusters of baryonic matter (e.g., star-formation or active galactic nuclei feedbacks, gas clumping; Simionescu et al. 2011, Gonzalez et al. 2013, Eckert et al. 2016), no other physical mechanisms can induce mass segregation over spatial scales typical of galaxy clusters (White et al. 1993, Evrard 1997). It follows that the fraction of baryonic matter in a galaxy clusters is expected to reflect the one of the entire Universe. From a cosmological point of view, galaxy clusters can therefore provide a representative view of the matter content of the Universe, as well as being ideal and highly biased tracers of structure formation across cosmic time (Bahcall & Cen 1992, Bahcall & Fan 1998, Voit 2005). In fact, their consequent role as pivotal tools for cosmological studies is now well-established (e.g., Vikhlinin et al. 2009, Allen et al. 2011, Pratt et al. 2019).

On the other hand, the proper characterisation of the thermodynamic and physical state of the

intracluster medium is crucial for comprehending the observable properties of galaxy clusters. Their formation history has indeed a major role in shaping the intracluster medium, as the infall of diffuse gas and substructures in the cluster potential wells induces dynamical processes (e.g., gas sloshing, shock and cold fronts, turbulent motion; Markevitch & Vikhlinin 2007, Zuhone & Roediger 2016, Gaspari & Churazov 2013) affecting a galaxy cluster across a wide range of scales. At the same time, feedback mechanisms from the stellar population and active galactic nuclei have an impact on the innermost regions of galaxy clusters (Churazov et al. 2000, McNamara & Nulsen 2007, 2012), regulating their otherwise catastrophic radiative cooling (Fabian 1994). The possibility of observing such extreme phenomena in conditions not accessible on Earth or in other astrophysical systems further positions galaxy clusters as unique laboratories for testing plasma physics on astrophysical scales.

Many of the advances in the characterisation of the physical and thermodynamic properties of galaxy clusters have been possible thanks to the observation of the X-ray emission dominated by thermal bremsstrahlung from the hot ($10^7 - 10^8$ K) and low-density ($10^{-2} - 10^{-3}$ cm^{-3}) intracluster gas. Since the original identification by the UHURU satellite of galaxy clusters as luminous X-ray sources (Kellogg et al. 1972, Forman et al. 1972), X-ray observatories have had a profound and transformative impact on our understanding of the physics of the intracluster medium and evolution of galaxy clusters (Sarazin 1986).

On the opposite end of the electromagnetic spectrum, radio observations have long provided an alternative view on the intracluster medium. More or less extended radio emissions are often observed in the direction of galaxy clusters. In the core regions, the plasma expelled from the active galactic nuclei at the centre of galaxy clusters (Churazov et al. 2000, McNamara & Nulsen 2007) is visible in the form of radio lobes (Tadhunter 2016), sometimes coincident with X-ray cavities (Fabian 2012, Gitti et al. 2012). On larger scales, diffuse radio emissions and relics (Feretti et al. 2012) have provided the evidence that galaxy clusters harbour populations of non-thermal electrons (Feretti & Giovannini 2008, Brunetti & Jones 2014) gyrating in the weak large-scale magnetic fields ($0.1 - 10$ μGauss) permeating the intracluster medium (Brüggen et al. 2012, van Weeren et al. 2019).

The last decades has however witnessed important developments in millimetre and submillimetre facilities, which opened a new window for the detailed study of the dynamical and astrophysical processes operating in the intracluster gas. The dramatic improvements on both the observational and instrumental side achieved in the past years has in fact allowed for mapping with unprecedented resolution and sensitivity the peculiar signature imprinted in the ubiquitous cosmic microwave background (CMB) through its interaction with the hot electrons residing within galaxy clusters, the so-called *Sunyaev-Zeldovich effect*.

1.1 The Sunyaev-Zeldovich effect

The Sunyaev-Zeldovich (SZ) effect is the result of the scattering of CMB photons with the energetic electrons moving freely in the gravitational well of a galaxy cluster (Zeldovich & Sunyaev 1969, Sunyaev & Zeldovich 1972). As the energy of the CMB photons is negligible with respect to the one of the ICM electrons, the CMB radiation is inverse-Compton scattered

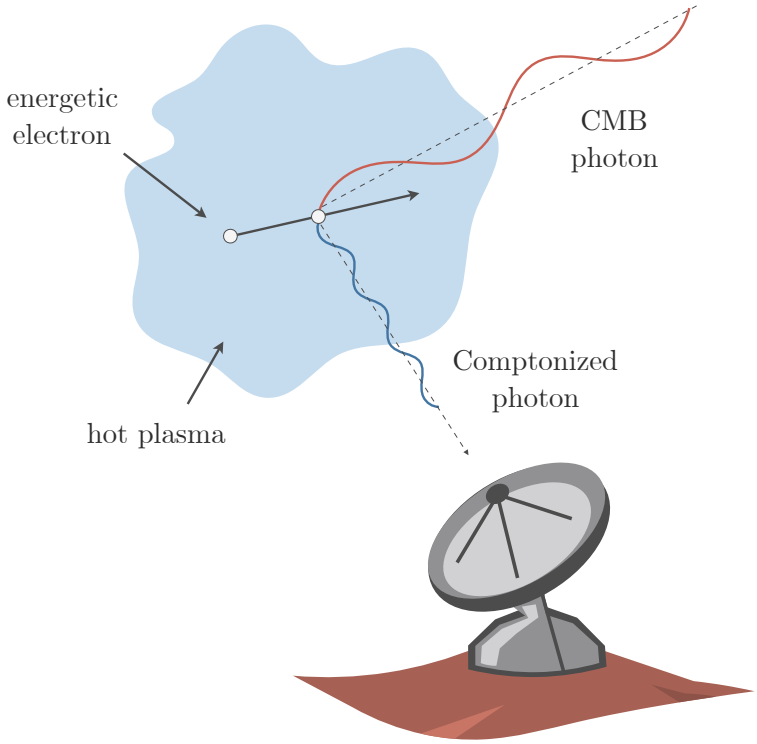

Figure 1.1: Schematic diagram of the thermal SZ effect. The figure is adapted from Mroczkowski et al. (2019b) and is an updated version of the classic illustration by L. van Speybroeck.

to higher frequencies. The net results are a distortion of the CMB spectrum and the consequent variation of the CMB surface brightness at a given frequency measured in the direction of a galaxy cluster (or any reservoir of hot electrons). The characterisation of the SZ signal can thus provide valuable information on the distribution of the hot electrons and, then, of the baryonic matter within a galaxy cluster. This has made the SZ effect a powerful observational tool both for complementing X-ray observations and for bringing an independent and unique view of the intracluster medium.

The specific details of the spectral distortion induced in the CMB is entirely dependent on the velocity distribution of the intracluster electrons. Given the complexity, it is thus clear how it should be more correct to talk about the SZ signal as the result of a multiplicity of effects. In this section, I provide an overview of the basic theoretical concepts behind several flavors of the SZ effect, while I will focus on their importance in the framework of high-resolution studies of the intracluster physics later on in the next chapters. The discussion presented henceforth is based mostly on the latest review by Mroczkowski et al. (2019b), to which I contributed and refer for further details.

1.1.1 Thermal component

The dominant contribution to the SZ signal from a galaxy clusters is generally referred as *thermal SZ effect* and arises due to thermal electrons characterised by an isotropic Maxwell-Boltzmann velocity distribution (see Figure 1.1). Zeldovich & Sunyaev (1969) originally computed the expected CMB spectral distortion due to the thermal SZ effect by solving the Kompaneets equation (Kompaneets 1957) for a low-energy blackbody radiation field undergoing single-scattering events off an isotropic distribution of thermal electrons. At a given frequency ν, the variation imprinted in the surface brightness of the primary CMB is

$$\delta i_{\rm tsz}(\nu) = i_0 \, \frac{x^4 e^x}{(e^x-1)^2} \left[x \frac{e^x+1}{e^x-1} - 4 \right] y, \tag{1.1}$$

where x and i_0 denote the dimensionless frequency $x = h\nu/k_{\rm B}T_{\rm CMB}$, and the CMB surface brightness normalization $i_0 = 2(k_{\rm B}T_{\rm CMB})^3/(hc)^2$. Here, h and $k_{\rm B}$, are respectively the Planck and Boltzmann constants, c is the speed of light, and $T_{\rm CMB} = 2.725$ K the primary CMB temperature (Fixsen 2009). Note that the explicit dependence of the SZ effect on the specific direction of observation is here omitted for the sake of readability.

The thermal Compton parameter y measures the magnitude of the CMB spectral distortion due to the SZ effect, and is proportional to the line-of-sight integral of the thermal electron pressure $P_{\rm e}$ from the observer to the last scattering surface. For an electron gas with temperature $T_{\rm e}$, optical depth $\tau_{\rm e}$ and density $n_{\rm e}$, it is indeed possible to write

$$y \equiv \int \frac{k_{\rm B}T_{\rm e}}{m_{\rm e}c^2} \, {\rm d}\tau_{\rm e} = \int \frac{k_{\rm B}T_{\rm e}}{m_{\rm e}c^2} \, n_{\rm e}\sigma_{\rm T} \, {\rm d}\ell = \frac{\sigma_{\rm T}}{m_{\rm e}c^2} \int P_{\rm e} \, {\rm d}\ell, \tag{1.2}$$

with $P_{\rm e} = n_{\rm e}k_{\rm B}T_{\rm e}$. Here, ${\rm d}\ell$ is the coordinate in the direction of the line of sight, while the constants $\sigma_{\rm T}$ and $m_{\rm e}$ denote the Thomson cross-section and the electron rest mass, respectively. The thermal SZ effect can thus provide important information on the electron pressure distribution inside galaxy clusters.

From an observational point of view, the thermal SZ effect features a distinct spectral signature, that allows one to exploit it for accurately discriminating between the thermal SZ signal, CMB, or other astrophysical contaminants (e.g., unresolved radio and dusty sources, diffuse emission from our Galaxy; Planck Collaboration XXII 2016, Madhavacheril et al. 2019). In particular, as can be seen in Figure 1.2, the scattering of the CMB radiation to higher frequencies induces a decrement in the photon count at frequencies lower than the cross-over value for which the thermal SZ signal is null ($\nu_{\rm null} \simeq 217$ GHz). On the other hand, as the number of photons in a scattering process is conserved, the thermal SZ spectrum at frequencies above $\nu_{\rm null}$ manifests itself as increment with respect to the surface brightness of the primary CMB.

Equations (1.1) and (1.2) show that the thermal SZ surface brightness is independent of redshift, making the thermal SZ effect not affected by redshift-dimming. Of course, this does not account for the evolution of the large-scale structure across cosmic time, which could introduce an effective variation with redshift of the observed SZ effect. Nevertheless, the redshift-independence of surface brightness of the thermal SZ effect makes this an unparalleled probe of the astrophysical processes taking place in the warm and hot gas populating the large-scale structures within our

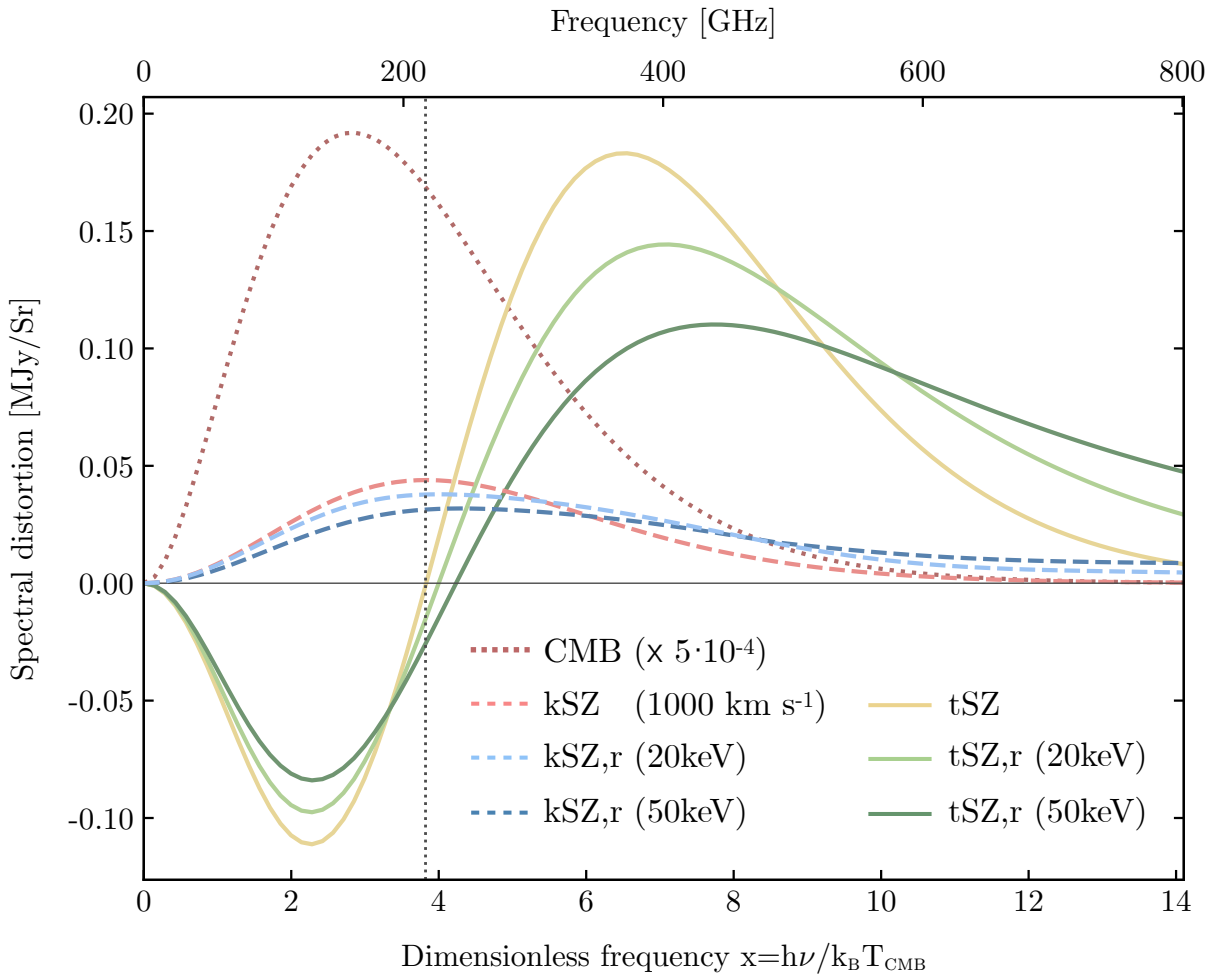

Figure 1.2: Spectral signatures of the thermal (solid) and kinematic (dashed) components of the SZ effect. The SZ signals are computed assuming representative values for the optical depth ($\tau_e = 10^{-2}$) and the Compton parameter ($y = 10^{-4}$). For a comparison, the primary CMB spectrum is also included (dotted dark red curve; for display purposes, it is scaled by a factor of $5 \cdot 10^{-4}$). The vertical line denotes to the null of the non-relativistic SZ effect ($\nu_{\rm null} \simeq 217$ GHz). The figure is adapted from Mroczkowski et al. (2019b).

Universe[1]. Further, the integrated SZ signal can provide a direct measure of the thermal content of the intracluster medium. The spherically integrated Compton parameter $Y_{\rm sph}$ is in fact proportional to the total thermal energy of a galaxy cluster (Mroczkowski et al. 2009),

$$Y_{\rm sph}(<r) = \frac{\sigma_{\rm T}}{m_{\rm e}c^2}\int_o^r P_{\rm e}(\eta) 4\pi\eta^2 {\rm d}\eta = \frac{2}{3}\frac{\sigma_{\rm T}}{m_{\rm e}c^2}\frac{1}{1+1/\mu_{\rm e}} E_{\rm th}(<r), \tag{1.3}$$

[1]It is worth noting that Churazov et al. (2015) showed how X-ray measurements, as a consequence of the evolution in the X-ray luminosity for a given mass and despite the intrinsic redshift-dependent dimming (see Section 1.2.1), are also nearly independent of the cluster redshift.

where, for simplicity, $P_e(r)$ is assumed to be spherically symmetric, and

$$E_{\rm th}(<r) = \frac{3}{2}\int_0^r (1+1/\mu_{\rm e})P_{\rm e}(\eta)4\pi\eta^2 {\rm d}\eta, \tag{1.4}$$

with $\mu_{\rm e}$ equal to the mean molecular weight of the electrons. Also, under the assumption of self-similar formation of galaxy clusters, the thermal energy of a virialized system is primarily determined by the gravitational potential well dominated by the dark matter halo (Kaiser 1986, Mroczkowski 2011). It follows that the thermal SZ effect offers a robust proxy of the total masses of galaxy clusters, key for using these as cosmological probes (see, e.g., Carlstrom et al. 2002, Kitayama 2014, Pratt et al. 2019).

1.1.2 Relativistic corrections

As already mentioned, the expressions presented in the previous section for thermal SZ effect are derived in the limit of non-relativistic electrons. However, the intracluster gas has temperatures $k_{\rm B}T_{\rm e} \gtrsim 5$ keV on average, resulting in electrons in thermal motion at average speeds around 10% of the speed of light. It is thus clear that, in such cases, the non-relativistic formulation of the thermal SZ effect discussed in the previous section does not hold and requires to be corrected for relativistic effects (see, e.g., Wright 1979, Rephaeli 1995, Challinor & Lasenby 1998, Itoh et al. 1998, Sazonov & Sunyaev 1998).

The spectral dependence of the thermal SZ effect corrected for different electron temperatures is shown in Figure 1.2. The net consequence is a broadening of the thermal SZ spectrum toward higher frequencies, which become more and more relevant as the electron temperature increases. On the one hand, this means that a proper characterisation of the pressure distribution of the intracluster medium through the observation of the thermal SZ signal would require an accurate determination of the electron temperature and, hence, of the resulting relativistic contribution to the thermal SZ spectrum. This is of course not possible in the case of single-band measurements and in the lack of external information on the electron temperature, and the reconstruction of a model for the electron pressure distribution of a galaxy cluster could then be biased significantly. On the other hand, the relativistic corrections to the thermal SZ effect allow for gaining fundamental information about the intracluster temperature via multi-frequency observations of galaxy clusters (Pointecouteau et al. 1998).

1.1.3 Kinematic component

The thermal SZ effect and its relativistic corrections just discussed represent the dominant contributions to the overall SZ signal studied in the analyses presented in this thesis. Hereafter, when referring to the generic *SZ effect* and unless specified otherwise, I will thus consider only its thermal component corrected for relativistic effects. Nevertheless, it is worth mentioning that a potential contamination may arise due to the SZ component induced by the interaction of the CMB radiation with a collection of electrons undergoing bulk motion with respect to the CMB rest frame (Sunyaev & Zeldovich 1980), the kinematic SZ effect (see Figure 1.3). This produces a

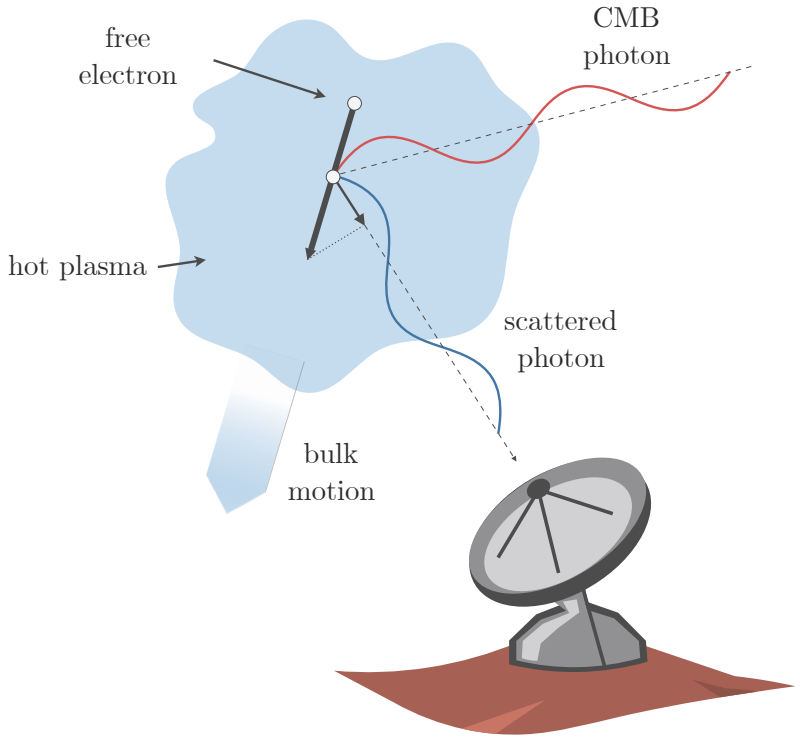

Figure 1.3: Diagram of the kinematic SZ effect (adapted from Mroczkowski et al. 2019b).

Doppler shift of the CMB spectrum (Figure 1.2) in the direction of an electron ensemble moving with a velocity with line-of-sight component $v_{\rm LOS} = c \cdot \beta_{\rm LOS}$. The resulting variation of the surface brightness can be written as

$$\delta i_{\rm ksz}(\nu) = -i_0 \frac{x^4 e^x}{(e^x - 1)^2} \int \sigma_{\rm T} n_{\rm e} \beta_{\rm LOS} \, {\rm d}\ell. \tag{1.5}$$

In analogous manner to the effect of redshift, the $\beta_{\rm LOS}$ is assumed to be negative (positive) for electrons moving toward (away from) the observer. The characterisation of the kinematic SZ can thus provide an immediate insight into the dynamical state of galaxy clusters or parts of them, helping in tracing the formation history of the large-scale structures. However, the spectral distortion is indistinguishable from the spectrum of the fluctuations in the primary CMB. This makes the robust reconstruction of the kinematic SZ signal challenging. Further, as for the case of relativistic corrections discussed above, any unaccounted motion of or within the intracluster medium may cause either global or localized variations of the observed SZ signal, potentially affecting the characterisation of the cluster pressure distribution.

Several additional effects may enter the total budget of the measured SZ signal, e.g., relativistic corrections to the kinematic term, the SZ effect from non-thermal, highly energetic electrons (as the ones filling the cavities inflated by active galactic nuclei or producing diffuse radio structures; Enßlin & Kaiser 2000, Colafrancesco et al. 2003), or the effects induced by multiple scatterings (Sunyaev & Zeldovich 1980, Chluba et al. 2014). However, these are generally negligible with

respect to the leading thermal and kinematic SZ signatures. I refer to the review by Mroczkowski et al. (2019b) and references therein for a thorough and extended discussion.

1.2 The SZ effect at subarcminute resolution

The ability to map the formation of large-scale structures nearly independently of their redshift, as well as the direct connection with thermal content of virialised systems has made the SZ effect a standard observational tool for cosmological studies. Indeed, the thermal SZ effect is now routinely used for detecting galaxy clusters in wide-field surveys up to redshifts $z \sim 2$ (e.g., Planck Collaboration XXVII 2016, Marriage et al. 2011, Hasselfield et al. 2013, Hilton et al. 2018, Bocquet et al. 2019, Huang et al. 2020, Bleem et al. 2020). However, the possibility of employing galaxy clusters in cosmological applications heavily relies on the accurate estimation of the cluster masses. On the one hand, the cross-calibration of SZ-derived masses with multiple tracers of the mass of galaxy clusters (e.g., X-ray-based masses, weak gravitational lensing; Pratt et al. 2019) can provide critical advances in our understanding of the systematics entering the mass-observable scaling relations. On the other, the rich phenomenology of astrophysical processes observed in galaxy cluster environments results in non-negligible deviations from the standard assumption of hydrostatic equilibrium (e.g., Battaglia et al. 2012, Shi et al. 2015, Biffi et al. 2016, Ansarifard et al. 2020). Thus, a deeper insight into the physical and thermodynamic state of the intracluster medium over a wide range of scales is key in improving our ability to derive reliable mass estimates. Furthermore, as detailed in the introduction to this chapter, the study of the processes taking place in the intracluster gas offers the unique opportunity to probe extreme plasma mechanisms in regimes not accessible by other means. In order to actually investigate the small-scale properties of galaxy clusters, observations capable of probing the intracluster medium down to tens of kiloparsecs are paramount.

1.2.1 Complementarity with X-ray observations

Due to limitations both in angular resolution and sensitivity of past SZ facilities, the study of the internal structure of galaxy clusters via the SZ effect has long been limited to a few remarkable and nearby systems. X-ray observations have played a major role in driving the advances in modelling the intracluster medium (Sarazin 1986, Markevitch & Vikhlinin 2007, Böhringer & Werner 2010, Vikhlinin et al. 2014, Bykov et al. 2015, Gu et al. 2018 are a few reviews of past and state-of-art applications of X-ray measurements for the study of cluster physics). Nevertheless, the significant advances in millimetre- and submillimetre-wave instrumentation achieved in the last few years have opened a new opportunity for accessing the SZ signal from galaxy clusters at an angular resolution and with overall integration times comparable to X-ray observations. This means that SZ experiments can provide information on the thermodynamic properties of the intracluster medium complementary with and at some level competitive to X-ray measurements.

The X-ray surface brightness due to thermal bremsstrahlung emission can be written as (in

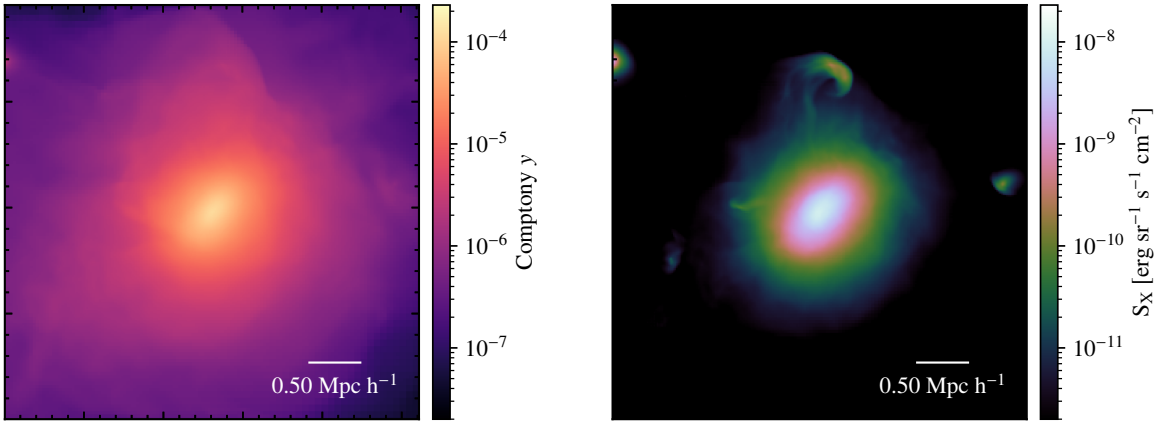

Figure 1.4: Comparison of the thermal SZ effect (left) and X-ray emission (right) maps for a galaxy cluster extracted from the *Omega500* cosmological hydrodynamical simulation (Nelson et al. 2014). The difference in the extents of the two signals is evident, as well as the presence of more prominent, higher contrast structures in the X-ray surface brightness than in the SZ image (adapted from Sehgal et al. 2019).

units of counts arcmin^{-2} s^{-1}; Rybicki & Lightman 1979)

$$S_{\rm X} = \frac{1}{4\pi(1+z)^3} \int n_{\rm e}^2 \Lambda_{\rm ee}(T_{\rm e}, Z) {\rm d}\ell, \tag{1.6}$$

where $\Lambda_{\rm ee}$ is the emissivity within a given energy band and Z is the heavy element abundance (metallicity) of the X-ray-emitting gas. For given metallicity and electron temperature, deprojection and forward modelling of the measured X-ray surface brightness thus allow for constraining the electron density field within galaxy clusters. On the other hand, the temperature of the intracluster electrons governs the high-energy cut-off in the energy spectrum of the thermal bremsstrahlung emission. The analysis of the X-ray spectra hence provides leverage on the intracluster temperature (and gas metallicity), offering a prompt observational tool for disentangling the effects of density and temperature on the measured X-ray emission (see, e.g., Sarazin 1986, Böhringer & Werner 2010).

Figure 1.4 offers a comparison of the thermal SZ and X-ray signals from the same galaxy cluster. A first immediate difference lies in the fact the SZ effect covers radii larger than the corresponding X-ray emission. This is a direct consequence of their different scaling with the electron density distribution, which makes the X-ray surface brightness ($\propto \int n_{\rm e}^2 {\rm d}\ell$) drop faster than the SZ effect ($\propto \int n_{\rm e} {\rm d}\ell$) with the distance from the cluster cores. This implies that, by means of the thermal SZ effect, one can easily access the low-density outskirts of galaxy clusters, central for studying the accretion processes in the cosmic large-scale structures (Walker et al. 2019). Second, in the lack of major disturbances as, e.g., merger shocks, the SZ effect is expected to appear smoother than the X-ray emission. Isobaric perturbations dominate the innermost regions of (relatively) relaxed clusters, and hence do not generate any noticeable structures in the pressure-sensitive thermal SZ footprint of the intracluster medium (Arévalo et al. 2016, Churazov

et al. 2016, Zhuravleva et al. 2016). The different line-of-sight dependencies on the electron density and temperature of the X-ray and SZ signals from a galaxy cluster represents one of the advantages in their joint analysis. This can in fact be used to infer the three-dimensional geometry of a galaxy cluster (Sereno et al. 2012), as well as on the level of clumping in the intracluster gas or any substructure in it (Fusco-Femiano & Lapi 2014, Tchernin et al. 2016). The combination with kinematic SZ effect could then further help in deriving information on the formation history of a galaxy cluster.

On the other hand, the limited energy windows of X-ray telescopes can make the reconstruction of cluster temperature distributions unreliable in the case of very high temperatures. As it will be shown later in Chapter 3 of this thesis, this may happen, for example, in the presence of merger shocks, in which the post-shock temperature could be boosted to values exceeding 20 keV. The combination of the constraints on density and pressure obtained respectively from X-ray and SZ data can clearly overcome such limitation. In the case of multi-frequency measurements of the SZ spectrum, additional independent constraints on the electron temperature can even be derived from the SZ data alone by means of the relativistic corrections to the SZ effect (e.g., Erler et al. 2018). An independent reconstruction of the electron pressure from the SZ effect can also help in studying the behavior of the intracluster medium through contact discontinuities. These are expected to be in pressure equilibrium with the environment. Any deviation from a smooth SZ signal through such a front would be the direct evidence of non-thermal pressure support (Markevitch & Vikhlinin 2007). Similarly, the comparison of X-ray and SZ observations represents a valuable approach for shedding light on the physical properties of the observational features associated with the merging history of a galaxy cluster (e.g., sloshing, gas compression; see Chapter 2 for an application to the notorious galaxy cluster RX J1347.5–1145, among the most X-ray luminous clusters ever discovered in an X-ray survey), as well as on the fluctuations of the thermodynamic properties of the intracluster medium (Churazov et al. 2016).

1.2.2 Radio-interferometric observations of galaxy clusters

High-angular resolution measurements of the SZ effect by single-dish facilities such as MUSTANG-2 on the 100-meter Green Bank Telescope, with a full width at half maximum (FWHM) beam size of 9 arcsec at 90 GHz (Dicker et al. 2014), or the NIKA2 instrument on the IRAM 30-meter telescope, with 17.5 arcsec and 11 arcsec FWHM beams respectively at 150 GHz and 260 GHz (Adam et al. 2018a), now allow the characterisation of pressure substructure in a growing number of clusters. In particular, both parametric (e.g., Adam et al. 2014, Romero et al. 2015) and non-parametric methods (e.g., Ruppin et al. 2017, Romero et al. 2018, Romero et al. 2020) have proven to provide a reliable description of the ICM pressure profile, while structure-enhancement filtering techniques have been successfully applied for detecting discontinuities in cluster SZ surface brightness maps (Adam et al. 2018b).

Nevertheless, radio interferometers remain the only instruments so far capable of measuring the SZ effect with an angular resolution better than 5 arcsec (at the expense of a mapping speed generally lower than single dishes and a severe high-pass filtering effect; see discussion below). The history of SZ studies is actually studded with interferometric measurements of the SZ effect. The Very Large Array (VLA; Moffet & Birkinshaw 1989) and the Ryle telescope (Jones et al. 1993,

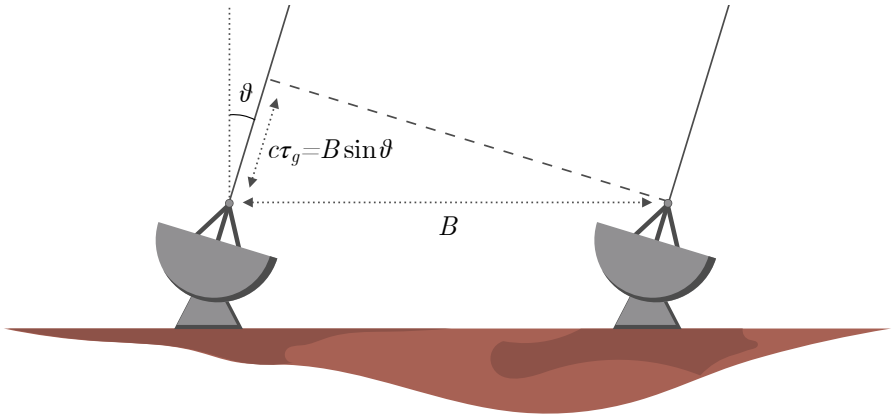

Figure 1.5: Schematic illustration of a single-baseline interferometer. The signal from an infinitely distant astronomical source arrives on the baseline element on the left with a delay of $\tau_g = B \sin\vartheta/c$ with respect to the antenna on the right (Thompson et al. 1986).

Grainge et al. 1993) were the first to image the SZ signal from galaxy clusters. The Owens Valley Radio Observatory (OVRO) array and the Berkeley-Illinois-Maryland Array (BIMA; Carlstrom et al. 1996) performed an extensive observational program, resulting in a first statistically relevant sample of SZ measurements from clusters in the redshift range $0.17 < z < 0.89$ (Carlstrom et al. 2002). This was then succeeded by the numerous observations by the Sunyaev-Zeldovich Array and the Combined Array for Millimeter-wave Astronomy (SZA & CARMA, respectively; Muchovej et al. 2007), the Arcminute MicroKelvin Interferometer (AMI; Zwart et al. 2008) and the Array for Microwave Background Anisotropy (AMiBA; Lin et al. 2009). Nevertheless, it was with the advent of the Atacama Large Millimeter/Submillimeter Array (ALMA; Wootten & Thompson 2009) and the complementary 7-meter Atacama Compact (Morita) Array (ACA; Iguchi et al. 2009) that interferometric SZ observations have started rivaling X-ray measurements in term of both resolution and sensitivity. Currently, only a handful of pioneering studies of the SZ effect with ALMA have however been performed: images at unprecedented angular resolutions have been obtained for two of the most famous galaxy clusters, RX J1347.5–1145 (Kitayama et al. 2016, Ueda et al. 2018) and the Phoenix cluster (Kitayama et al. 2020), while Gobat et al. (2019) measured the SZ decrement from the distant cluster Cl J1449+0856 ($z = 1.99$); the observations of the "El Gordo" Cluster by Basu et al. (2016) provided the first high-resolution detection of a merger shock; finally, Lacy et al. (2019) found the first putative evidence of SZ signal induced by the thermal wind originating from active galactic nuclei (later confirmed at comparable significance by Brownson et al. 2019).

Basics of radio-interferometry

In the simplest scenario, a radio-interferometer is composed by a single pair of antennae, i.e., a baseline, located at a distance B from each other and observing the same source in the direction ϑ (here measured with respect to the zenith; Figure 1.5). Assuming the observed source to be distant enough so that its signal is characterised by a planar wavefront, this will reach one of the two

antennae with a delay of $\tau_g = B \sin\vartheta/c$ with respect to the other element of the pair. The geometric delay τ_g measures the phase coherence of the incoming signal, i.e., the cross-correlation fringe phase, equal to $\phi = 2\pi\nu\tau_g$ for an interferometer operating at a frequency ν. A variation in the source direction ϑ would then correspond to a shift of the fringe phase $\Delta\phi = (2\pi\nu/c)B\cos\vartheta\Delta\vartheta$. The angular scale ϑ_b recovered by a single baseline is thus the one corresponding to the fringe period $\Delta\phi = 2\pi$,

$$\vartheta_b = \frac{\Delta\vartheta}{2\pi} = \frac{1}{B\cos\vartheta}\frac{c}{\nu} = \frac{\lambda}{B\cos\vartheta}, \tag{1.7}$$

where, trivially, $\lambda = c/\nu$ is the wavelength of the incoming wavefront. In terms of resolving power, the inverse proportionality of the minimum resolved scale with respect to the baseline length is analogous to the dependence of the resolution of a single dish with its size ($\sim \lambda/D$ for a dish of diameter D). Roughly speaking, a radio-interferometer hence behaves like a single dish of diameter equal to the length of the longest baseline, with the advantage of allowing for achieving a superb angular resolutions without the requirement of building a large-aperture telescope. However, as it will be discussed in the next section, this comes with the major drawback of high-pass filtering the measured signal on scales larger than the one corresponding to the dish size of the individual interferometric elements.

A measurement of the signal from the same sky position collected by the different antennae of a given interferometric baseline is obtained by considering their coherence over a a period of time equal to the geometric delay τ_g. For a generic source with surface brightness $i(\boldsymbol{x}, \nu)$ in the direction $\boldsymbol{x}$ and observed at a frequency ν, the resulting cross-correlation function can be written as (Bracewell 1958, Thompson et al. 1986)

$$V_0(\boldsymbol{u}, w, \nu) = \int \frac{1}{\sqrt{1-|\boldsymbol{x}-\boldsymbol{x}_0|^2}} A(\boldsymbol{x}, \nu)\, i(\boldsymbol{x}, \nu) \mathrm{e}^{2\pi j\left[\boldsymbol{u}\cdot(\boldsymbol{x}-\boldsymbol{x}_0)+w\left(\sqrt{1-|\boldsymbol{x}-\boldsymbol{x}_0|^2}-1\right)\right]} \mathrm{d}\boldsymbol{x}, \tag{1.8}$$

and takes the name of *(complex) visibility*. Here, $\boldsymbol{u} = (u, v)$ is the two-dimensional Fourier space coordinate vector — position in the so-called uv-plane — which represents the spatial wavelengths corresponding to the projection of the baselines on the plane of the sky. The coordinate w is instead the baseline vector component parallel to the line of sight and measured in the direction of the phase reference position $\boldsymbol{x}_0$. The function $A(\boldsymbol{x}, \nu)$ describes the (normalised) attenuation of the sky map in a given direction $\boldsymbol{x}$ induced by the non-uniform beam response pattern of an antenna, and is a function of frequency. In general, the primary beam function vanishes rapidly as a function of the distance from the phase centre, so that the resulting single-pointing field of view is limited mainly to the region where $|\boldsymbol{x} - \boldsymbol{x}_0| \ll 1$. This further implies that it is possible to approximate the observed surface brightness as being distributed on the plane tangent to the sky at the position $\boldsymbol{x}_0$. In such case, $w = 0$ and the position-dependent denominator can be approximated by unity[2]. The visibility function can then be simplified as follows,

$$V_0(\boldsymbol{u}, \nu) \approx V_0(\boldsymbol{u}, 0, \nu) = \int A(\boldsymbol{x}, \nu)\, i(\boldsymbol{x}, \nu)\, \mathrm{e}^{2\pi j \boldsymbol{u}\cdot\boldsymbol{x}} \mathrm{d}\boldsymbol{x}, \tag{1.9}$$

[2]The field of view of typical ALMA observations of galaxy clusters cover up to a few arcminutes. As a reference, in the specific case of the 7-meter ACA, the full-width-half-maximum of the primary beam is roughly 1.5 arcmin, and the corresponding w-correction is $\sqrt{1-|\boldsymbol{x}-\boldsymbol{x}_0|} - 1 \lesssim 10^{-6}$.

where, without loss of generality and for ease of notation, I set $\boldsymbol{x}_0 = 0$. The above equation implies that, in the limit of such flat-sky approximation, an interferometric measurement can be directly related to the Fourier transform of the sky surface brightness attenuated by the antenna response pattern[3]. In such case, the inverse relation between the observed visibilities and the source surface brightness $i(\boldsymbol{x}, \nu)$ holds:

$$i(\boldsymbol{x}, \nu) = V_0(\boldsymbol{u}, 0, \nu) = A^{-1}(\boldsymbol{x}, \nu) \int V_0(\boldsymbol{u}, \nu)\, \mathrm{e}^{-2\pi j \boldsymbol{u}\cdot\boldsymbol{x}} \mathrm{d}\boldsymbol{x}. \tag{1.10}$$

In a real observation, the visibility measurements are of course corrupted by noise. The root-mean-square noise level in the reconstructed surface brightness $i(\boldsymbol{x}, \nu)$ is (Thompson et al. 1986)

$$\sigma_{\mathrm{rms}} = \frac{2k_{\mathrm{B}}T_{\mathrm{sys}}}{A_{\mathrm{eff}}\sqrt{N_{\mathrm{b}}t_{\mathrm{int}}\Delta\nu}}. \tag{1.11}$$

which represents the sensitivity of a radio-interferometer to a point-like source. Here, T_{sys} is the system noise temperature (and accounts for both atmospheric and instrumental contributions), and A_{eff} the effective collecting area of a single element of the array composed of N_{b} baselines. The terms t_{int} and $\Delta\nu$ instead are the integration time and the bandwidth of the observation, respectively, and their increase represents a critical factor for improving the signal-to-noise ratio of the measurements from a given radio-interferometer.

A high-pass filtered view of the SZ effect

In practice, the finite number of baselines composing a radio-interferometer limits the measurement of the sky visibility function to a few uv-modes, exactly corresponding to the collection of baseline projections over the observation period. Specifically, at every instant of the whole integration time, an interferometric array of M elements will populate the uv-plane with $N_{\mathrm{b}} = M(M-1)/2$ points. The specific projection of a baseline on the sky is however dependent on the position of the observed source, and Earth's rotation makes it change during any extended observations. Along with the expected improvement in the signal-to-noise ratio of an interferometric measurement, a longer integration can thus be used to gain a denser coverage of the uv-plane. The resulting uv-plane scans correspond to arcs of an elliptical locus determined by the hour angle and declination of the observed field (roughly, as the declination δ_0 increases, the scanning track changes from a circle around the uv-space origin to an ellipse offset along the v axis by a factor $\cos\delta_0$; Thompson et al. 1986). Multi-frequency observations can provide further aid in filling in the uv-plane. As the measured cross-correlation phase is a function of wavelength (see Equation 1.7 and related discussion), each uv-space point of a given observation with frequency bandwidth $\Delta\nu$ is smeared radially over a range of uv-distances $\Delta|\boldsymbol{u}| = B * \Delta\nu/c$. See Figure 1.6 for an illustration of the different effects of the integration time and bandwidth on the uv-plane coverage.

[3]The same result can be derived by means of the van Cittert-Zernike theorem, originally formulated in the framework of optical interferometry (van Cittert 1934, Zernike 1938). It states that the mutual coherence of a distant incoherent source, i.e., the time-averaged cross-correlation of the electric fields measured at two separate positions, equals its complex visibility.

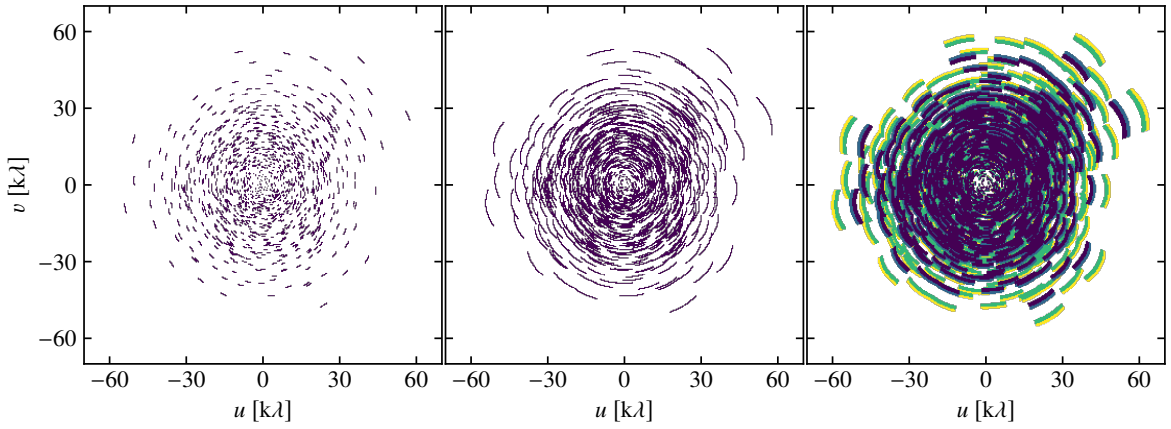

Figure 1.6: Example of the improvement obtained in the total coverage of the *uv*-plane when increasing the integration time from 30 minutes (left) to two hours (middle), and in the case of a broad-band multi-frequency observation (right). The array configuration and the spectral coverage (84 – 88 GHz and 96 – 100 GHz) have been chosen to reflect the typical set-up employed in the observation of the SZ effect with ALMA. As the interferometric visibilities correspond to the Fourier transform of a real signal, they are described by a complex Hermitian function (i.e., $V(-\boldsymbol{u}) = V^{\dagger}(\boldsymbol{u})$, where $\dagger$ denotes the conjugate operation). To better highlight the single features in the *uv* distributions, only half of the corresponding Hermitian visibility function is thus plotted (hence causing the asymmetry observed in the *uv* patterns).

It is possible to account for the incomplete coverage of the visibility space performed by the whole ensemble of baselines over the entire observing period through the introduction of a sampling function $\boldsymbol{S}(\boldsymbol{u}, \nu) = \sum_{\mathrm{b}} \delta_{\mathrm{D}}\{\boldsymbol{u} - \boldsymbol{u}_{\mathrm{b}}(\nu)\}$, where $\boldsymbol{u}_{\mathrm{b}}$ is the *uv*-plane coordinate corresponding to the given projected baseline b operating at a frequency ν. The measured visibility function can then immediately be written as $V(\boldsymbol{u}, \nu) = \{\boldsymbol{S} \cdot V_0\}(\boldsymbol{u}, \nu)$. It follows that the inverse Fourier transform in Equation (1.10) is no longer valid, and the inversion of the visibility equation would have solution

$$i_{\mathrm{D}}(\boldsymbol{x}, \nu) = i(\boldsymbol{x}, \nu) * B_{\mathrm{D}}(\boldsymbol{x}, \nu) = A^{-1}(\boldsymbol{x}, \nu) \int \{\boldsymbol{S} \cdot V_0\}(\boldsymbol{u}, \nu)\, \mathrm{e}^{-2\pi j \boldsymbol{u}\cdot\boldsymbol{x}} \mathrm{d}\boldsymbol{x}, \tag{1.12}$$

where $*$ denotes the convolution operation. The convolution kernel $B_{\mathrm{D}}(\boldsymbol{x}, \nu)$ is generally referred as the *dirty beam*, and is given by the inverse Fourier transform of the sampling function $\boldsymbol{S}(\boldsymbol{u}, \nu)$,

$$B_{\mathrm{D}}(\boldsymbol{x}, \nu) = \int \boldsymbol{S}(\boldsymbol{u}, \nu)\, \mathrm{e}^{-2\pi j \boldsymbol{u}\cdot\boldsymbol{x}} \mathrm{d}\boldsymbol{x}. \tag{1.13}$$

As a consequence of the missing information on all the scales corresponding to unmeasured *uv*-modes, the pattern of the dirty beam may present significant side-lobe structures (see Figure 1.7). The resulting *dirty image* $i_{\mathrm{D}}(\boldsymbol{x}, \nu)$ would hence correspond to a heavily filtered version of the true surface brightness $i(\boldsymbol{x}, \nu)$. This issue, generally referred as *missing-flux problem*, is actually twofold: first, the sparse coverage of the Fourier plane results in poor constraints for some angular scales within the range probed by the interferometer; second, the shortest baseline achievable

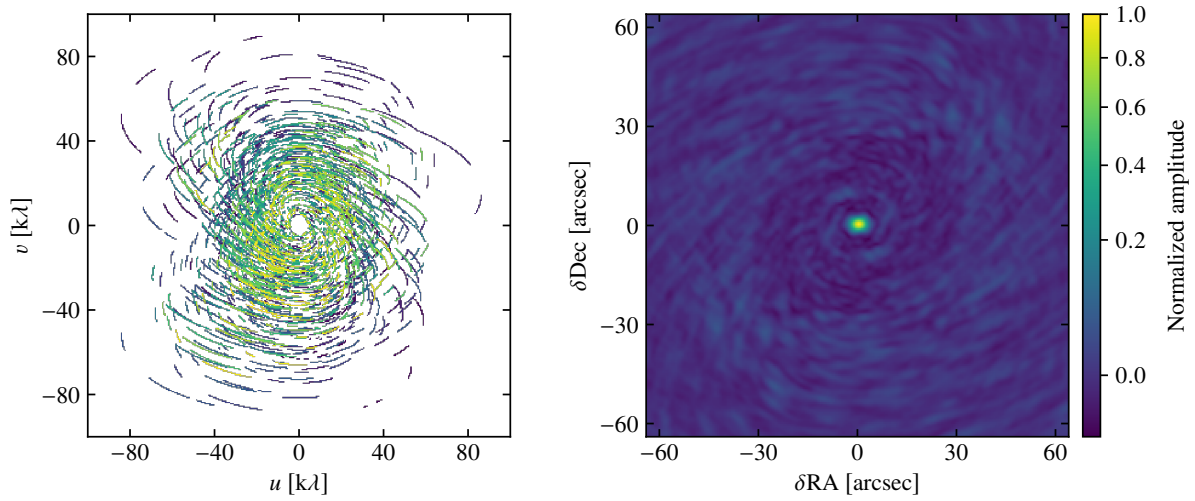

Figure 1.7: Example of sparse visibility function (left) and corresponding dirty beam pattern (right). For display purposes, only single-frequency data are considered. The different colors in the visibility pattern correspond to individual baselines. As for Figure 1.6, the asymmetry in the *uv*-coverage arises from the fact that only one from each pair of conjugate visibilities is plotted.

is essentially determined by the shadowing limit, when one antenna is in front of another as seen from the source. This sets a hard upper limit on the maximum recoverable scale of an interferometric observation.

In general, most of the sources in typical interferometric observations cover only a small fraction of the field of view of a radio-interferometer, and the filtering effects of the large angular scales are generally negligible (however, as discussed below, this is not the case for galaxy clusters). On the other hand, several deconvolution techniques aimed at tackling the missing flux issue on the smaller angular scales are now available, and can provide a robust mitigation of the effects of the dirty beam side-lobes on the reconstructed maps. At present, the CLEAN algorithm (Högbom 1974) represents, along with its various implementations, the de-facto standard deconvolution method. It is based on an iterative procedure operating, at each iteration, on the dirty map after subtraction of the *CLEAN image*. This is obtained by matching a point-source (or Gaussian; Cornwell 2008) component to the residual dirty map, and it is then added to the CLEAN map after being smoothed by an ideal beam (generally equal to a Gaussian with same full-width-half-maximum of the central lobe of the dirty beam).

Regardless of the clear success and strengths of deconvolution algorithms, any analyses of deconvolved interferometric images present a few major limitations. First, both the Fourier inversion and the non-linear deconvolution of the *uv*-space data introduce non-trivial correlations in the image-space noise. In fact, although visibilities are characterised by random, uncorrelated Gaussian noise, the numerous side-lobe structures of the dirty beam correlate both the signal and the noise over the entire image constructed by CLEAN. Second, any chosen weighting and gridding schemes (key for applying computationally inexpensive discrete Fourier transforms for inverting the sparse visibilities; Thompson et al. 1986), along with the specific image-reconstruction tech-

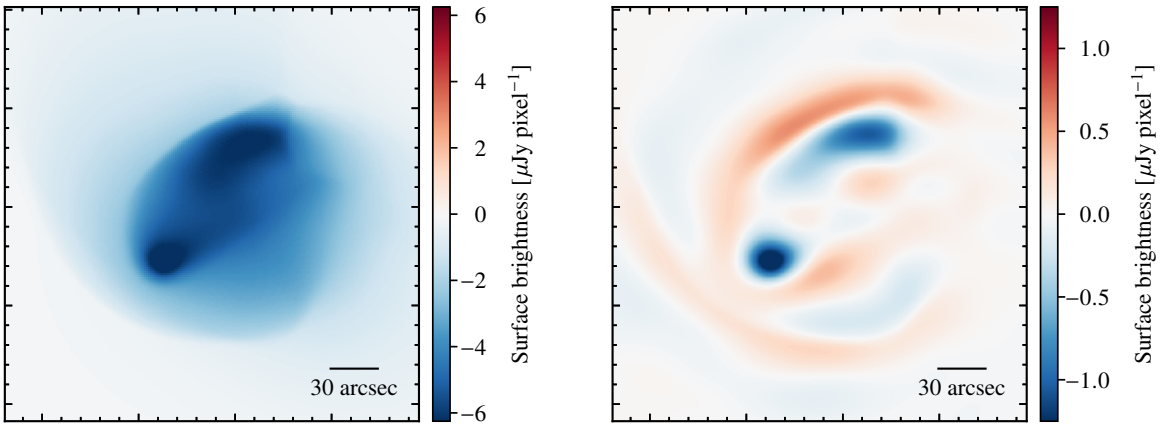

Figure 1.8: Mock interferometric observation of the simulated "El Gordo" Cluster (courtesy of C. Zhang; see Zhang et al. 2015 and Zhang et al. 2018 for a thorough description of the simulation employed to generate the map in the left panel). The filtered map (right) is generated applying a natural weighting scheme to the raw visibilities and without deconvolving for the incomplete sampling of the *uv*-space. In order to better highlight the interferometric filtering alone, the simulated observation is noise-free.

nique, may possibly introduce artefacts. These couple with the difficulties in obtaining a robust extrapolation of any information over angular scales larger than the one corresponding to the shortest baseline.

A straightforward solution to all the issues related to the deconvolution of the interferometric data consists in fitting the visibilities directly in Fourier space through a forward-modelling procedure. As already mentioned, the visibility data exhibit nearly Gaussian noise, and modelling in Fourier space allows for full knowledge of the instrument sampling function. Further, it allows for exploiting extensively the multi-frequency nature of the interferometric data, and, hence, for constraining the spectral dependence of the measured signals. In order to fully exploit the potentialities of visibility modelling, a range of tools have been developed (see, e.g., `uvmultifit` by Martí-Vidal et al. 2014 or `galario` by Tazzari et al. 2018).

Nevertheless, the short-spacing problem remains particularly relevant for sources covering large fractions of, or extending beyond, the field of view of the instrument. In the case of galaxy clusters, this manifests itself in a significant high-pass spatial filtering of the extended signal due to the SZ effect. A simulation of the effects of the interferometric filtering on the SZ signal from a galaxy cluster is showed in Figure 1.8. While the small-scale features are generally preserved, it is evident how the bulk of the SZ signal is entirely filtered out. This implies that radio-interferometers, while powerful instruments for probing the internal structure of the intracluster medium, can provide only limited constraints on the global properties of galaxy clusters.

1.3 This thesis

The work presented in the following chapters of this thesis is aimed at exploring the actual potentialities of radio-interferometers and, in particular, of ALMA+ACA in probing the intracluster medium via observations of the SZ effect at high angular resolution.

Unfortunately, the complexities inherent to interferometric measurements pose serious challenges in the exploitation of radio-interferometers for constraining the physical and thermodynamic properties of galaxy clusters. The severe filtering effect introduced by the sparse and incomplete sampling of the *uv*-plane discussed in the previous section impedes a prompt interpretation of the outcome of interferometric images of the SZ effect in the direction of galaxy clusters. Among the major limitations is the short-spacing issue. This can not be overcome by means of interferometric data alone, as any solution aimed at improving the coverage of the *uv*-plane would in fact fill this only over the range of *uv*-modes comprised between the ones corresponding to the minimum spacing set by the shadowing limit of the array and its maximum baseline. In order to get a sensible understanding of the measured SZ signatures from galaxy clusters, it is crucial to include complementary information from external data.

The combination of the radio-interferometric measurements of the SZ with single-dish observations at lower angular resolution can provide a powerful means of extending the spatial dynamic range of the data and of filling the short-spacing region of the *uv*-plane. Several techniques — feathering, deconvolution informed by total flux measurements, synthetic short-spacing (I refer the reader to Stanimirovic 2002 for an overview) — have been developed to include short-spacing information at different steps of the interferometric imaging process, but these still rely on highly non-linear deconvolution algorithms. For this reason, I have developed a modelling technique for performing a joint analysis of interferometric observations and large-scale data from single-dish facilities. To avoid any biases induced in the interferometric images by the deconvolution processes, the reconstruction of the SZ signal from the interferometric data is performed directly on the raw visibilities and builds upon the *uv*-space modelling methods introduced in the previous section. Indeed, analogous approaches have already been shown over the past two decades to provide a reliable technique for studying interferometric observations of the SZ effect (see, e.g., Carlstrom et al. 1996, LaRoque et al. 2006, Feroz et al. 2009, Mroczkowski et al. 2009, Basu et al. 2016, Abdulla et al. 2019 for an incomplete list of examples of applications of the interferometric modelling technique).

In Chapter 2, I report the results of a test of such joint analysis on a combination of ALMA, Bolocam, and *Planck* observations of the SZ effect from the galaxy cluster RX J1347.5–1145, a very hot and luminous cluster showing signatures of a merger. The joint image-visibility analysis allowed for probing the SZ effect and, hence, the electron pressure distribution over an outstanding dynamic range of spatial scales, from $\sim$ 30 kpc to well beyond the outskirts of the cluster. The consequent reconstruction of global pressure model provided the means for highlighting the presence of local pressure disturbances within RX J1347.5–1145. The direct comparison of the small-scale structures observed in the resulting SZ images and the information retrieved from a multi-band X-ray analysis on their equation of state have then been key to constrain the complex thermodynamic state of the intracluster medium.

In the absence of large-scale SZ data, prior knowledge about any key physical parameters

obtained from observations at different wavelengths (e.g., X-ray, optical) can of course be readily incorporated in the modelling process. In particular, the combination of X-ray and SZ data at such high angular resolution yields a powerful probe of the physical conditions of the intracluster medium in the vicinity of shocks within galaxy clusters. This has been pivotal in the analysis presented in Chapter 3 of the thermal SZ effect from the western, most-prominent shock front in the Bullet Cluster (1E0657-56). In fact, ALMA+ACA data are primarily sensitive to the electron pressure difference across the shock fronts. To constrain the shock properties, the difference measured in the Bullet Cluster data had to be combined with the value for the pre-shock electron pressure derived from an independent *Chandra* X-ray analysis.

Finally, Chapter 4 includes a test of the capabilities of ACA observations to provide robust validation of cluster detections via the thermal SZ effect. In fact, the verification of the presence of ionised intracluster medium, indicative of a collapsed and nearly virialised system, is fundamental for providing the direct confirmation of galaxy clusters discovered in wide-field surveys. The studied data set comprises a pilot sample of ten galaxy clusters from the Massive and Distant Clusters of WISE Survey (MaDCoWS). The test of the *Verification with the ACA – Localisation and Cluster Analysis* (VACA LoCA) programme demonstrates that the ACA can robustly confirm the presence of the virialised intracluster medium in galaxy clusters.

Chapter 2

Joint ALMA-Bolocam-*Planck* SZ study of RX J1347.5–1145

The content of this chapter was originally published as ***Di Mascolo, L.****, Churazov, E., & Mroczkowski, T., 2019, MNRAS, 487, 4037*

As discussed in the previous chapter, radio-interferometric measurements of the SZ effect are severely affected by the spatial filtering effects over scales larger than the one corresponding to the shortest baseline in the observation. Additional large-scale constraints are required in order to correctly derive a global description of the pressure distribution in galaxy clusters. Several studies (see, e.g., Romero et al. 2018) have already shown the importance of joint analysis of both low- and high-resolution observations when attempting to obtain information over a broad range of spatial scales. In general, all previous studies of the SZ effect I am aware of that have combined SZ data from instruments sampling different spatial frequencies have either been limited to image-space or to interferometric SZ data exclusively.[1] In this chapter, I extend the analysis for combining both interferometric and single-dish measurements by modelling the thermal SZ effect signal from galaxy clusters through the joint fitting of SZ imaging and interferometric data.

As test case, I apply the joint image-visibility model reconstruction technique to single-dish and interferometric observations of the SZ effect from the galaxy cluster RX J1347.5–1145 (z = 0.451). It is among the most massive and X-ray luminous clusters ever observed, which have made it the ideal target of observations over a broad range of wavelengths (Figure 2.1). In particular, due to the availability of a number of millimetre measurements of the SZ effect in the direction of the cluster, covering several frequencies and spatial resolutions, it provides an excellent test bed for probing the applicability of the combined study of radio-interferometric and single-dish data.

RX J1347.5–1145 is a massive galaxy cluster discovered in the ROSAT X-ray all-sky survey (Schindler et al. 1995, Voges et al. 1999). The studies based on the low angular resolution ROSAT

[1] I note however that there have been several studies over the past two decades relying on joint likelihood analyses of X-ray surface brightness imaging data with interferometric SZ observations (e.g., Reese et al. 2000, LaRoque et al. 2006, Mroczkowski et al. 2009).

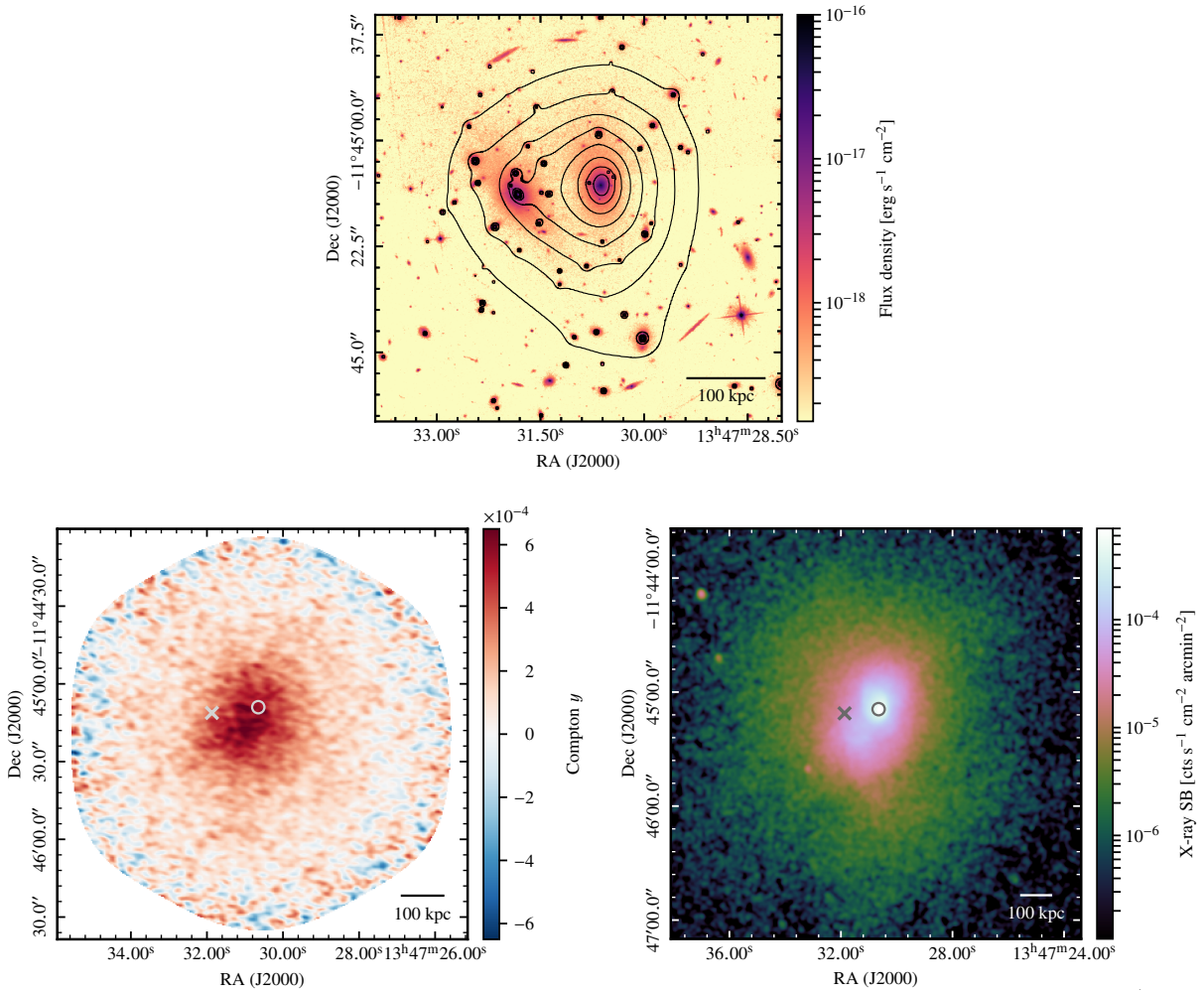

Figure 2.1: Multi-wavelength view of the galaxy cluster RX J1347.5–1145. Shown are the HST-ACS optical image (top), the Compton y image of the SZ effect created by feathering the ACA, ALMA, and Bolocam data (bottom left; see Section 2.1 for a description of the SZ data), and the *Chandra* 0.5-3.5 keV X-ray surface brightness (SB) map (bottom right). Overlaid in the top panel are the contours from the Zitrin et al. (2015) light-traces-matter lensing κ-map. The circle and the cross in the X-ray and SZ images indicate respectively the positions of the western (wBCG; $13^{\rm h}47^{\rm m}30\overset{\rm s}{.}65, -11°45'9\overset{''}{.}00$) and eastern (eBCG; $13^{\rm h}47^{\rm m}31\overset{\rm s}{.}87, -11°45'11\overset{''}{.}20$) of the two dominant cluster galaxies observed in the optical map. Note that each panel has a different scale and center.

X-ray data initially highlighted a spherical, strongly peaked surface brightness profile, suggesting the cluster to be dynamically relaxed and characterised by a cool central region (Schindler et al. 1997). However, the high-resolution measurements of the SZ effect in the direction of RX J1347.5–1145 performed by the Nobeyama Bolometer Array (NOBA; Komatsu et al. 2001) provided early indications of a significant enhancement of the SZ signal to the south-east of the X-ray emission peak (i.e., the "south-eastern SZ excess"). Subsequent X-ray observations

of the cluster by *Chandra* (Allen et al. 2002), *XMM-Newton* (Gitti & Schindler 2004), and *Suzaku* (Ota et al. 2008) confirmed the existence of a south-eastern extension in the proximity of the core region, manifesting temperatures higher than the average value of the surrounding intracluster medium. The evidence of a disturbed SZ morphology was further supported by the high-resolution SZ imaging of both single-dish observations (Mason et al. 2010, Adam et al. 2014) and radio interferometric data (Plagge et al. 2013, Kitayama et al. 2016), which additionally allowed for identifying a potential pressure discontinuity east of the X-ray peak (Mason et al. 2010, Adam et al. 2018b). The analyses of, for example, Korngut et al. (2011) and Plagge et al. (2013) further determined that the excess could account for $\sim 9-10\%$ of the total thermal energy of the cluster, assuming the bulk pressure distribution of the cluster can be described by a spherically-symmetric model.

The current interpretation of the observed cluster morphology relates the south-eastern structure to gas that has been stripped away and shock-heated as a consequence of a major merging event. In this scenario, the involved subcluster is assumed to be moving in the south-west-north-east direction and to strongly perturb the main, initially-relaxed, cool-core cluster component. This is also consistent with the results of the weak- and strong-lensing analyses of optical data (Bradač et al. 2008, Köhlinger & Schmidt 2014, Zitrin et al. 2015, Ueda et al. 2018), which show that the projected mass density has a primary peak centred near the active galactic nucleus embedded in the cool core, and an additional component elongated towards a secondary peak at or near the brightest cluster galaxy (BCG) to the east of the X-ray peak (hereafter "eBCG" to distinguish it from that coincident with the cluster core, which I refer to as "wBCG"; see the top panel of Figure 2.1, which includes the lensing contours from Zitrin et al. 2015). Furthermore, optical spectroscopic analysis constrains the dynamics of the merger to take place mainly in the plane of the sky (Miranda et al. 2008, Lu et al. 2010). This is corroborated by the small difference in the redshifts of the two dominant BCGs, measured to be of the order of ~ 100 kms^{-1} (Cohen & Kneib 2002). On the other hand, a radio mini-halo has been detected in the direction of the cool-core region (Gitti et al. 2007, Ferrari et al. 2011), and has been considered as an indication of the possible occurrence of sloshing gas within the cluster core. In fact, diffuse radio emission has been found to be spatially correlated with the cold fronts generated by the sloshing gas motions (Mazzotta & Giacintucci 2008, ZuHone et al. 2013). However, although the comparison of the observed X-ray surface brightness and hydrodynamic simulations further favors the scenario of the sloshing gas and south-eastern substructure as due to a plane-of-sky merger, the cluster merger dynamics and geometry are still subjects of debate (Johnson et al. 2012, Kreisch et al. 2016). More recently, Ueda et al. (2018) combined X-ray, strong-lensing and interferometric SZ observations to study RX J1347.5–1145. Along with confirming the correspondence of the SZ enhancement with stripped gas that has been shock-heated to high temperatures, they also reported that the sloshing in the cluster core seen in X-ray data is not accompanied by large pressure variations, suggesting subsonic gas velocities in this region. The compact structure of the characteristic spiral pattern observed in the cool-core region has been considered as an indication that it has been plausibly induced by a secondary, minor interaction instead of the major merger related to the south-eastern substructure.

Throughout this chapter, I assume a flat ΛCDM cosmology with $\Omega_m = 0.308$, $\Omega_\Lambda = 0.692$, and $H_0 = 67.8$ km s^{-1} Mpc^{-1}, consistent with the *Planck* cosmological results (Planck Collaboration

	ALMA	ACA
Average RMS	12 μJy beam^{-1}	83 μJy beam^{-1}
Resolution	(4.1, 2.4) arcsec	(20.5, 11.1) arcsec
MRS	58.8 arcsec	99.7 arcsec
FoV	62 arcsec	107 arcsec
Frequency	84-88 GHz, 96-100 GHz	84-88 GHz, 96-100 GHz
Reference	Kitayama et al. 2016	Kitayama et al. 2016

Table 2.1: Details of the interferometric observations used for modelling RX J1347.5–1145. The noise RMS reported here is the average noise level measured from the dirty images generated by adopting a natural weighting scheme, while the resolution is provided in terms of the FWHM major and minor axes of the resulting synthesised beam. The maximum recoverable scale (MRS) is measured as the inverse of the shortest array baseline in units of wavelengths.

XIII 2016). Within this cosmology, 1 arcsec corresponds to a physical scale of 5.94 kpc at the redshift of RX J1347.5–1145.

2.1 Data and analysis overview

Here I present the set of single-dish and interferometric observations of employed in the joint analysis. A summary of the observations can be found in Table 2.1 and Table 2.2.

2.1.1 Atacama Large Millimeter Array

RX J1347.5–1145 was observed by both the main ALMA 12-meter array and 7-meter ACA during Cycle 2. The galaxy cluster was mapped employing seven mosaic pointings, each using four 2 GHz wide spectral windows. The spectral windows were centred at 85, 87, 97, and 99 GHz, that is in ALMA Band 3, which ranges 84-116 GHz. The combination of the two arrays resulted in visibilities covering the *uv*-plane between 2.1 and 115.9 kλ, corresponding to spatial scales of 1.66 arcmin and 1.78 arcsec, respectively (Figure 2.2). I refer to Kitayama et al. (2016) for a more detailed description of the combined ALMA+ACA observation of RX J1347.5–1145.

I performed manual calibration of the ACA and ALMA measurement sets using the Common Astronomy Software Applications (`CASA`, McMullin et al. 2007) version 4.7.2, obtaining calibrated visibilities consistent with the data presented in Kitayama et al. (2016). I also assume an uncertainty on the overall flux calibration of 6% for both the ALMA and ACA data given the variance of the measured calibrator fluxes. All the interferometric images presented in this chapter, which are not used for analysis, were generated with `CASA` version 5.3.0.

Rather than modelling the full data sets, I consider spectral window-averaged visibilities for each of the fields. These are computed considering the weighted average of both the *uv* coordinates and complex values of the visibility points over a set of optimal bins defined as in Hobson et al.

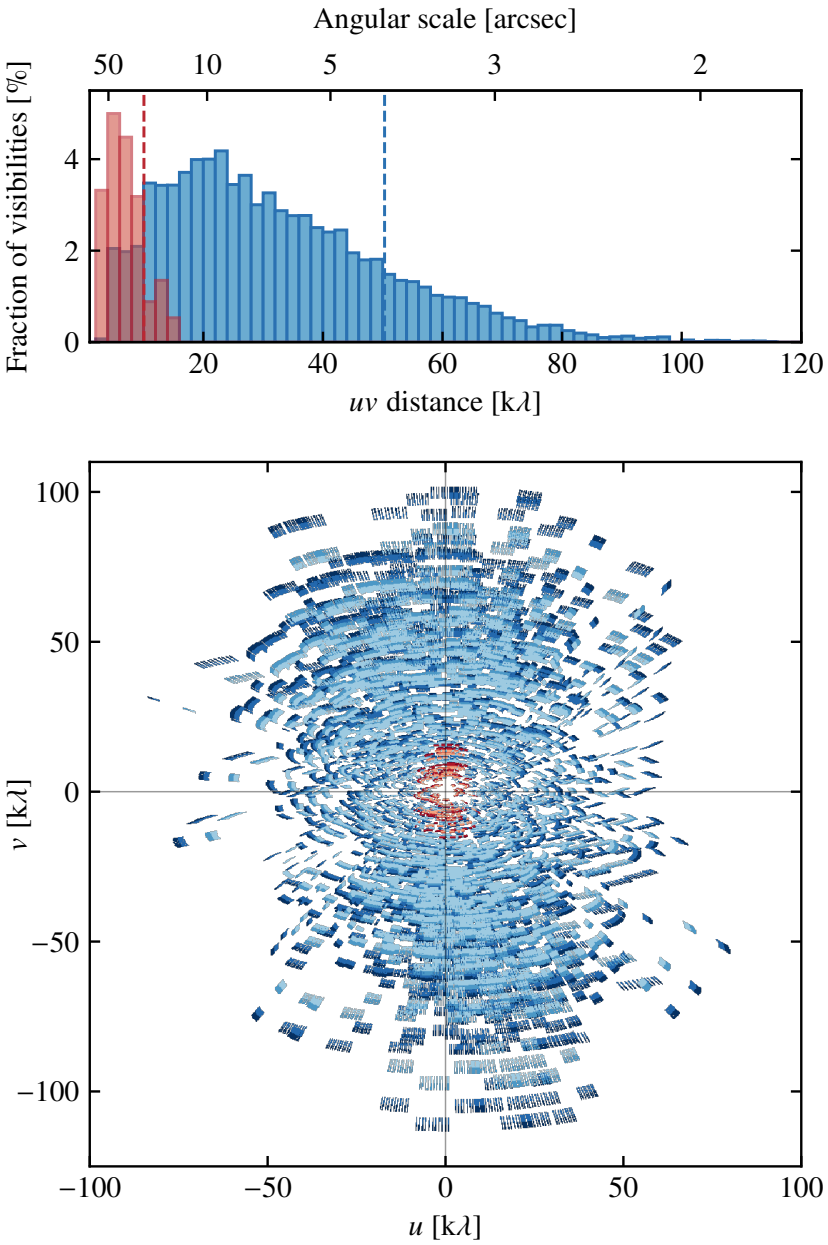

Figure 2.2: Histogram of the sampled *uv* distances (top) and coverage of the *uv*-plane (bottom) for the interferometric observation of RX J1347.5–1145 with the ALMA 12-meter (blue) and ACA 7-meter (red) arrays. The different shades of each colour indicate separate spectral windows. The vertical lines in the top panel refer to the major axis FWHM of the synthesised beams obtained by imaging the ACA and ALMA data separately, and adopting natural weights. I computed the fraction of visibilities per bin in *uv* distance with respect to the cumulative number of both ACA and ALMA data points.

(1995). I assume a top-hat frequency response over each spectral window. The primary beam model images obtained by running the CLEAN task independently for each pointing are used for accounting for primary beam attenuation when fitting the interferometric data.

The CMB multipoles corresponding to the scales probed by the ALMA+ACA observation are larger than $\ell = 6750$. Above such value, the amplitude of the anisotropies intrinsic to the primary CMB is smaller than 1 μK_{CMB}. This results to be of the order of only a few percent of both the ACA and ALMA instrumental noise, even when the presence of correlated visibilities that would enhance the significance of the CMB signal is properly taken into account. Hence, I assume the CMB term in the ALMA+ACA noise covariance matrix to be negligible. On the other hand, confusion noise may still be important. Confusion from radio sources is expected to be of the order of 1 μJy beam^{-1} for ACA and 10 nJy beam^{-1} for ALMA (see Equation 3.163 in Condon & Ransom 2016). These are below the noise levels reported in Table 2.1. However, confusion due to the emission from background dusty galaxies may not be negligible. Scaling the Lindner et al. (2011) measurement of confusion at 1.1 mm and in a 15.6 arcsec beam (comparable to the ACA beam size), I estimate the contribution from dusty star-forming galaxies in the cosmic infrared background is $\sim$ 15 μJy beam^{-1} in the ACA data. Here, I am assuming a dust emissivity spectral index of -2.5. For the ALMA 12-meter data, if I conservatively assume the sources are uncorrelated (see Béthermin et al. 2017, for discussion), I estimate the CIB contribution to be $\sim$ 1 μJy beam^{-1}. Therefore, any correlation between the data introducing off-diagonal components in the individual blocks of the noise covariance matrix is subdominant with respect to the instrumental noise. For simplicity, I then assume the ALMA+ACA block of the noise covariance matrix to be diagonal, and assign a weight to each point of the visibility function corresponding to the spectral window average of the theoretical post-calibration weights (Wrobel & Walker 1999).

2.1.2 Bolocam

I complement the ALMA+ACA data with the publicly available observation of RX J1347.5–1145[2] by Bolocam. The 144-element bolometer array provided measurements with a resolution of 58 arcsec at a reference frequency of 140 GHz, an uncertainty of 5% on the flux calibration, and pointing accuracy to 5 arcsec. An overview of the reduction process and data products is provided in Sayers et al. (2013). Along with the map of RX J1347.5–1145, the data products comprise a set of 1000 realizations of the 140 GHz astronomical sky, including contributions from both the CMB and unresolved, point-like sources. I used them for computing the generalised covariance matrix of the Bolocam noise to be adopted in the computation of the likelihood function.

2.1.3 *Planck*

Supplementary information about the large-scale morphology of RX J1347.5–1145 can be inferred from the *Planck* data.

[2] https://irsa.ipac.caltech.edu/data/Planck/release_2/ancillary-data/bolocam/

	Bolocam	*Planck*
Average RMS	0.38 mJy beam^{-1}	$1.2 \cdot 10^{-6}$ [Compton y]
Resolution	58 arcsec	10 arcmin
Largest scale	8.9 arcmin[b]	Full-sky
FoV	14 arcmin	Full-sky
Frequency	140 GHz	—[c]
Reference	Sayers et al. 2013	Planck Collaboration I 2016

Table 2.2: Details of the single-dish observations used for modelling RX J1347.5–1145. The largest mode recovered by Bolocam is the spatial scale corresponding to the transfer function HWHM frequency. In the case of the *Planck* data, instead of considering single-frequency images, I employ the MILCA Compton y map generated by combining all the *Planck* HFI data (100-857 GHz).

Instead of modelling each frequency map separately, I extracted $2^\circ \times 2^\circ$ cutouts patches from all the *Planck* High Frequency Instrument (HFI) full-sky maps from the 2015 public release (Planck Collaboration I 2016), smoothed to an effective resolution of 10 arcmin FWHM, and used them to generate a Compton y image of RX J1347.5–1145. I applied a component separation method analogous to the modified Internal Linear Combination algorithm (MILCA) discussed in Hurier et al. (2013). Since the map is generated under the requirements of removing the CMB contributions and minimising the variance in the reconstructed thermal SZ signal, I can consider the residual noise to be dominated by the uncertainties in the reconstructed Compton parameter y map. Moreover, the associated noise covariance matrix is assumed to be diagonal, with elements equal to the pixel-by-pixel MILCA estimates of the residual RMS noise level.

The *Planck* Compton y map is also used for computing the cylindrically integrated Compton parameter $Y_{\rm cyl}$ over a solid angle up to an angular radius of 15 arcmin. I obtain

$$Y_{\rm cyl}(15\ \text{arcmin}) = (3.24 \pm 0.54) \times 10^{-3}\ \text{arcmin}^2, \tag{2.1}$$

where the uncertainties are obtained as the RMS of the same integral computed at random positions around the galaxy cluster (Adam et al. 2015). I compare this value to the one computed by integrating over the model Compton y map properly smoothed to the 10 arcmin FWHM resolution of *Planck*.

2.1.4 Computing the joint likelihood

One of the crucial steps in a joint Bayesian analysis of multiple observations is the computation of their joint likelihood. In the case of completely independent measurements, it would be enough to consider the product of the likelihood functions of the individual observations. However, potential contamination from astrophysical components other than (and uncorrelated with) the SZ signal explicitly modelled in the analysis could in fact introduce non-negligible covariance between different data sets, and should be accounted for in terms of additional contributions to the

generalised noise covariance matrix. This is the case of primary CMB anisotropies, or unresolved sources below the confusion limit of the instrument (see Appendix A.1.3 for a discussion). As a consequence, the joint likelihood function in the simplified form is valid for independent data, and calculating it for a mixture of imaging and visibility data may be a non-trivial exercise. Nevertheless, it turns out that for the data employed in this study, the impact of the cross-data correlations on the parameter reconstruction is minimal, and the simplified form of the joint likelihood function consisting of the product of single likelihoods can still be used.

Since the *Planck* Compton parameter y map has been explicitly built to minimize the signal from astrophysical components other than the SZ effect, I can assume the generalised noise covariance matrix does not include any terms arising from the correlation of the *Planck* map with the ALMA+ACA and Bolocam observations. In particular, as reported in Remazeilles et al. (2011), the high signal-to-noise ratio of the CMB signal in all of the *Planck* HFI maps guarantees the MILCA algorithm is able to efficiently remove the corresponding contamination from the recovered thermal SZ map. On the other hand, ACA, ALMA, and Bolocam may in turn not be independent, as any contaminating signal would be common to all the corresponding data sets. However, as discussed before, the CMB plays a negligible role in the noise budget of the ACA and ALMA measurements when compared to the instrumental noise. Therefore, I assume the contribution to the joint likelihood from off-diagonal blocks of the CMB component of the generalised covariance matrix to be negligible. Furthermore, as in, for example, Feroz et al. (2009), I assume the confusion from unresolved sources to be characterised by an uncorrelated angular power spectrum. Hence, considering the limited overlap in the scales probed by the different observations, the confusion covariance matrix can be considered to be block diagonal. The ACA, ALMA, and Bolocam data can then be considered to be independent of each other, and I compute the joint likelihood function as the product of the likelihoods of each data set.

I tested the validity of the above assumptions by running the model reconstruction technique on a sample of mock observations, including either correlated or independent CMB realizations for each of the simulated data sets. In both the cases, I have been able to recover the input model parameters. Moreover, I found no significant difference between the correlated and uncorrelated CMB simulations, therefore allowing each data set to be treated as independent from the others. The joint log-likelihood is therefore computed as the product of the individual likelihoods of each of the data sets presented in the previous sections.

2.1.5 Hyperparameters

The reconstruction of a model from the simultaneous analysis of multiple observations relies on the assumption of having perfectly calibrated data. However, systematics in the overall calibration may introduce non-negligible relative scaling factors between the different measurements. I can account for possible miscalibration offsets simply by multiplying the models for each of the data subsets by a scaling hyperparameter κ.

On the other hand, the statistical uncertainties associated with the image- and Fourier-space observations may suffer from distinct systematic effects that could bias the reconstruction of the model parameters. Therefore, I can weight the likelihood of each of the data sets by a hyperparameter η, whose estimate is driven directly by the statistical properties of the measurements. As

discussed in Hobson et al. (2002), such parameter is set to have an exponential prior, as derived by assuming to have no prior knowledge about the weighting factors, apart from the requirement of a unitary expectation value.

2.1.6 Implementation details

The fitting pipeline is written in `python` and uses primarily standard packages (e.g., `NumPy`, `SciPy`). The Fourier transforms are computed using the `FFTW` library (Frigo & Johnson 2012) and its `python` wrapper `pyFFTW`. All the common astronomical tasks are managed exploiting the community-developed package `AstroPy` (Astropy Collaboration 2018).

A Monte Carlo Markov Chain (MCMC) approach is adopted for performing the simultaneous forward-modelling of images and visibilities. In particular, I make use of the specific implementation of the affine-invariant ensemble sampling technique (Goodman & Weare 2010) provided by the `python` package `emcee` (Foreman-Mackey et al. 2013). The Message Passing Interface (MPI) protocol is used to parallelize the pipeline.

I evaluate the synthetic visibilities for the extended components using the modelling tool provided in the `galario` Python library (Tazzari et al. 2018). It can generate an interferometric model by sampling Fourier-space data defined on a regular grid at the positions of the sparse, observed visibilities using a bilinear interpolation algorithm. I modified the core `galario` library to allow for a more robust and accurate description of sources that extend significantly over the field of view or are at large offsets from the phase center direction of the interferometric data (see Appendix A.3 for a discussion).

2.2 Reconstruction of the pressure profile

I discuss here the results of the reconstruction of a model for the pressure profile of RX J1347.5–1145 by applying the joint modelling technique discussed above and detailed in Appendix A to a set of interferometric and image-domain data of the cluster SZ signal. The ability to discriminate between global thermodynamic properties and local perturbations to them is useful for providing a better understanding of the physical and dynamical state of the cluster. The wide range of spatial scales probed by a combination of single-dish and interferometric observations provides the unique opportunity to build an inclusive description of the physical and thermodynamic state of RX J1347.5–1145.

RX J1347.5–1145 is a clear example of a disturbed cluster for which it is not possible to obtain an unambiguous definition of a geometric center for the intracluster medium distribution. This is not an isolated case. The optical image is, for example, reminiscent of the Coma cluster, which also possesses two very bright elliptical galaxies separated by some 200 kpc (e.g., Vikhlinin et al. 1997). Unlike RX 1347.5–1145, neither of the two galaxies in Coma is embedded in a cool core. As a result, the definition of the cluster centroid in Coma is equally problematic in both X-ray and SZ images, while for RX 1347.5–1145 the center is often chosen to coincide with the cool core. This issue may be crucial when reconstructing an accurate physical model of a galaxy

cluster, since different specific choices of the reference position for modelling the thermodynamic profiles may lead to different implications for the derived cluster properties.

As baseline pressure model, I employ a generalised Navarro–Frenk–White (gNFW) profile. Hydrodynamic simulations have shown that it can describe reasonably well the radial pressure profile of a galaxy cluster (Nagai et al. 2007). This motivated its extensive application in a number of SZ studies for parametrizing the observed electron pressure distributions (e.g., Mroczkowski et al. 2009, Sayers et al. 2013, 2016a, Romero et al. 2018, Shitanishi et al. 2018). The gNFW pressure model can be written as a function of radial distance r from the centroid of the galaxy cluster $(x_{\rm gNFW}, y_{\rm gNFW})$ as follows:

$$P_{\rm e}(r) = P_{\rm ei} \left(\frac{r}{r_{\rm s}}\right)^{-\gamma} \left[1 + \left(\frac{r}{r_{\rm s}}\right)^{\alpha}\right]^{(\gamma-\beta)/\alpha} , \tag{2.2}$$

where $P_{\rm ei}$ is a pressure normalisation factor and γ, α, and β are the slopes at small, intermediate, and large scales with respect to a characteristic radius $r_{\rm s}$. It is easy to extend the above equation to the case of a cluster with projected eccentricity ε by substituting the ratio $(r/r_{\rm s})$ with a generalised ellipsoidal distance $\xi = \xi(r_{\rm s}, \varepsilon)$. The details are presented in Appendix B.

As discussed at the beginning of this section, RX J1347.5–1145 is thought to have undergone a major merger almost entirely in the plane of the sky. For this reason, I do not include any kinematic SZ contribution to model the cluster sub-components or its bulk motion. I refer to Zemcov et al. (2012), and Sayers et al. (2016b, 2019) for discussions about the kinematic SZ effect in RX J1347.5–1145.

2.2.1 Spherically symmetric SZ profile centered at the X-ray peak

The numerous analyses of the X-ray emission from RX J1347.5–1145 have shown that the peak of the X-ray surface brightness is located at the position of the cool-core region, only a few kiloparsecs away from the wBCG. In the major merger scenario introduced before, this has been generally considered as the center of the primary cluster component. Therefore, I first apply the fitting pipeline jointly to the ALMA+ACA, Bolocam, and *Planck* data for modelling the thermal SZ signal from the region corresponding to the cool core observed as a strong cusp in the X-ray surface brightness maps of RX J1347.5–1145. In particular, I fit a spherically symmetric gNW pressure profile whose centroid is set at the position of the peak in the observed X-ray brightness distribution, $(13^{\rm h}47^{\rm m}30\overset{\rm s}{.}593, -11°45'10\overset{''}{.}050)$. The parameters are fixed at the values reported in Arnaud et al. (2010) for the sample of a cool-core pressure profile, namely $\alpha = 1.2223$, $\beta = 5.4905$, and $\gamma = 0.7736$. The pressure normalisation $P_{\rm ei}$ and the profile characteristic radius $r_{\rm s}$ are left free to vary and are assigned wide uninformative uniform priors. Since I am interested in modelling only a portion of the cluster, I do not consider here any prior on the integrated SZ signal. Moreover, the data are not sensitive enough and do not provide sufficient spectral information for deriving any constraint on the electron temperature distribution through the measure of the level of relativistic corrections in the observed SZ effect. Therefore, I fix the electron temperature to $T_{\rm e} = 7$ keV, characteristic for the inner ~ 50 kpc region around the wBCG as derived from the analysis of *Chandra* data (discussed in Section 2.2.2). In order to remove the contamination from

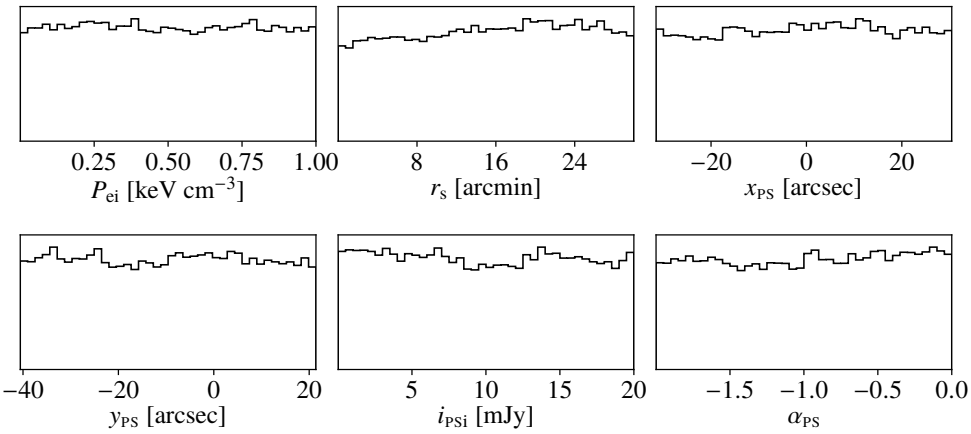

Figure 2.3: Marginalised posterior distributions for the prior-only run for the parametric modelling of the cool-core region of RX J1347.5–1145. A description of the model parameters and the corresponding priors can be found in Section 2.2.1 and references therein.

the bright radio source observed at the center of the cluster, I additionally include in the model a point-like component for which I assume a power-law spectral dependence. All the corresponding parameters — source coordinates x_{PS} and y_{PS}, flux normalisation i_{PSi}, spectral index α_{PS} — are constrained simultaneously with the cluster pressure profile, and set to have uniform priors: the source position is constrained to the most central of the ALMA fields, while I consider a wide uninformative range for the normalisation parameter based on previous measurements of the source flux around 100 GHz (Sayers et al. 2016b); similarly, the source spectral index is assumed to be negative but larger than -2, and thus to have a broad prior around the typical value for synchrotron radiation. Furthermore, I include both weighting and scaling hyperparameters in the analysis, providing Gaussian priors for the latter, with unitary mean values and standard deviations equal to the flux calibration uncertainties for each of the data sets.

A summary of the priors on the model parameters can be found in Table 2.3. I find that no biases are introduced by the specific choice of the prior distributions. This has been performed by sampling the posterior distribution obtained in the case of a constant likelihood, as it would be in absence of data. As the sampler explores only the prior space, such test can provide fruitful insight into any effects on the parameter reconstruction introduced by the specific choice of the prior distributions. The results of the data-free run are shown in Figure 2.3.

The posterior probability density function resulting from the MCMC sampling of the parameter space is shown in Figure 2.4. The best-fitting parameters and the corresponding uncertainties for both model components are defined by considering the medians and the central credibility intervals of the marginalised posterior distribution of each model parameter (see Table 2.4 for a summary). A synthetic realization for each of the observations employed in the modelling process is then generated and subtracted from the raw data sets. The poorer resolution and sensitivity of both the *Planck* and Bolocam data limit the possibility of observing any significant residual structure. Therefore, although the analysis has been performed jointly on all the available SZ data sets, I present in Figure 2.5 only the maps obtained from the residual ALMA+ACA measurements.

Parameter	Units	Cool-core	Global
$x_{\rm gNFW}$	arcsec	$\delta[0.00]$	$\mathcal{U}[-72.78, 72.50]$
$y_{\rm gNFW}$	arcsec	$\delta[0.00]$	$\mathcal{U}[-85.04, 66.63]$
$T_{\rm e}$	keV	$\delta[7.00]$	$\delta[12.50]$
$P_{\rm ei}$	keV cm^{-3}	$\mathcal{U}[0.00, 1.00]$	$\mathcal{U}[0.00, 1.00]$
$r_{\rm s}$	arcmin	$\mathcal{U}[0.00, 30.00]$	$\mathcal{U}[0.00, 30.00]$
ε	–	$\delta[0.00]$	$\mathcal{U}[0.00, 1.00]$
θ	degrees	$\delta[0.00]$	$\mathcal{U}[-90.00, 90.00]$
α	–	$\delta[1.2223]$	$\delta[1.2223]$
β	–	$\delta[5.4905]$	$\delta[5.4905]$
γ	–	$\delta[0.7736]$	$\mathcal{U}[0.00, 5.00]$
$x_{\rm PS}$	arcsec	$\mathcal{U}[-31.53, 30.47]$	$\mathcal{U}[-31.53, 30.47]$
$y_{\rm PS}$	arcsec	$\mathcal{U}[-40.58, 21.42]$	$\mathcal{U}[-40.58, 21.42]$
$i_{\rm PSi}$	mJy	$\mathcal{U}[0.01, 20.00]$	$\mathcal{U}[0.01, 20.00]$
$\alpha_{\rm PS}$	–	$\mathcal{U}[-2.00, 0.00]$	$\mathcal{U}[-2.00, 0.00]$
κ_i	–	$\mathcal{N}[1.00, \sigma_i]$	$\mathcal{N}[1.00, \sigma_i]$
η_i	–	$\mathcal{E}[1.00]$	$\mathcal{E}[1.00]$

Table 2.3: Summary of the prior distributions for the parameters of the spherical cool-core (Section 2.2.1) and ellipsoidal (Section 2.2.3) models. The parameters δ and $\mathcal{U}[a, b]$ denote respectively a Dirac delta function and a uniform distribution in the interval $[a, b]$, while $\mathcal{N}[\mu, \sigma]$ is a normal distribution with mean μ and standard deviation σ; $\mathcal{E}[1.00]$ is instead the exponential distribution with unitary expectation value discussed in Section 2.1.5. The coordinates of the gNFW and point-source model components are provided in terms of the angular distance from the peak in the X-ray surface brightness, ($13^{\rm h}47^{\rm m}30\overset{\rm s}{.}593, -11°45'10\overset{''}{.}050$), while the flux normalisation of the power-law spectral model is measured at the reference frequency $\nu_{\rm PS} = 90$ GHz. The values of the σ_i entering the priors of the scaling hyperparameters κ_i for each of the data sets analysed can be found in Section 2.1.

Notice that the model subtraction from interferometric data is performed directly in visibility space, and I only show the dirty images of the processed measurements for illustrative purposes.

The map obtained from the model-subtracted visibilities (middle right-hand panel of Figure 2.5) clearly shows a residual SZ signal at the position of the south-eastern substructure. Consistent with previous analyses (Adam et al. 2014, Ueda et al. 2018), the reconstruction of the spherically symmetric SZ model centered at the X-ray peak leads to the conclusion that the X-ray and SZ maps have coincident excesses, suggesting that this region is strongly overpressurized with respect to the cluster core.

Conversely, it is not possible to observe any signature of strong local deviations from the smooth gas pressure distribution within the cool core of the cluster. Indeed, no excess in the model-subtracted ALMA+ACA maps of the SZ signal is significantly detected in the direction

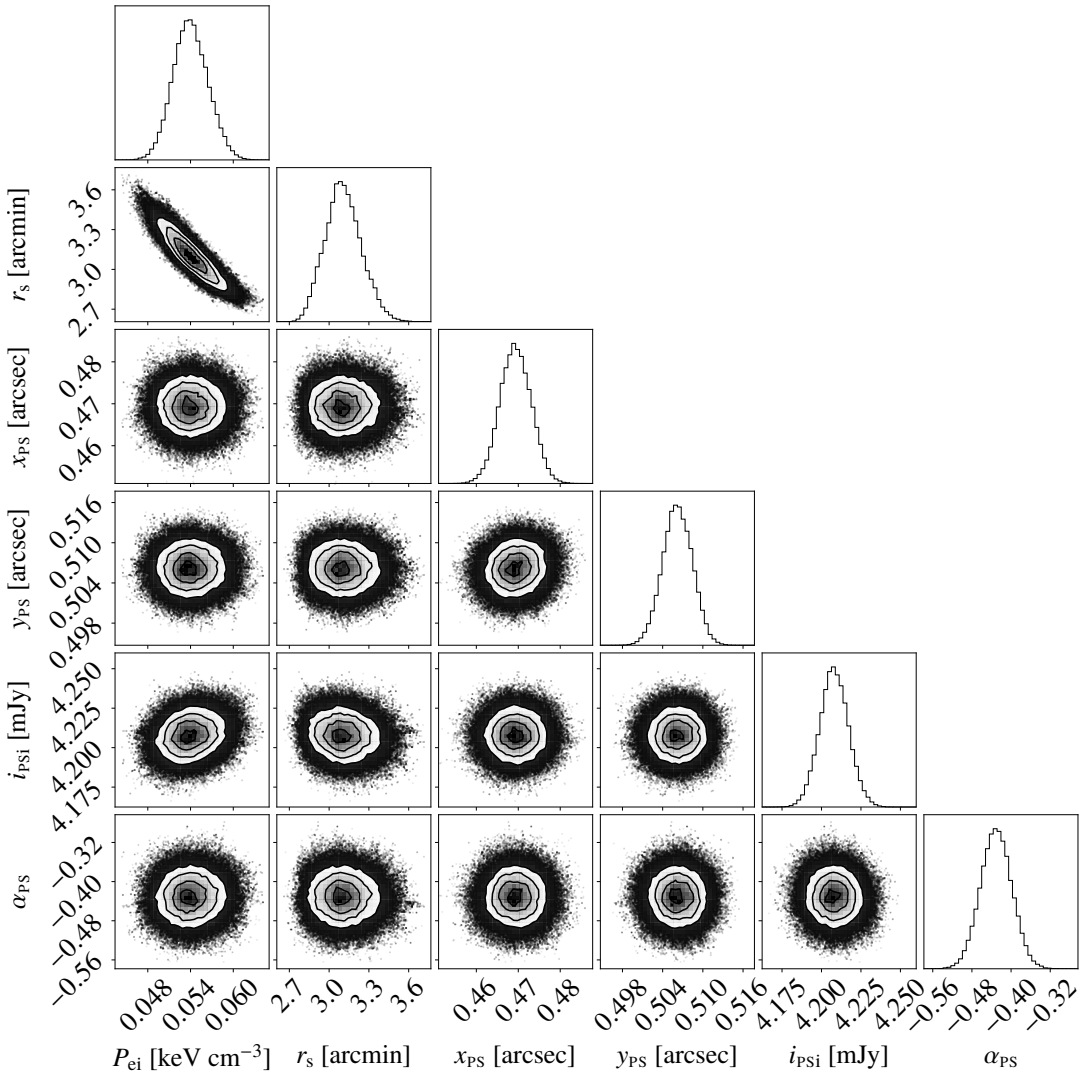

Figure 2.4: Bivariate posterior density functions and marginalised distributions of the MCMC parameters from the fit of the spherical gNFW pressure profile (P_{ei}, r_s) and power-law point source (x_{PS}, y_{PS}, i_{PSi}, α_{PS}). The phase space was sampled by 200 walkers in 2000 steps after a preliminary burn-in phase of 1000 steps. The reported contours correspond to 68%, 95%, and 99% confidence levels. The values of the respective best-fitting model parameters are presented in Table 2.4. The inferred position and the spectral index of the point-source model are reported as in Table 2.3.

of the region around the wBCG. In agreement with Ueda et al. (2018), this suggests that the occurrence of subsonic sloshing motions within the cool core.

Parameter	Units	Mean	16$^{\rm th}$ perc.	84$^{\rm th}$ perc.
$P_{\rm ei}$	10^{-2} keV cm^{-3}	5.39	5.16	5.65
$r_{\rm s}$	arcmin	3.10	2.97	3.24
$x_{\rm PS}$	10^{-2} arcsec	46.93	46.57	47.31
$y_{\rm PS}$	10^{-2} arcsec	50.62	50.40	50.84
$i_{\rm PSi}$	mJy	4.208	4.199	4.217
$\alpha_{\rm PS}$	–	−0.431	−0.462	−0.399

Table 2.4: Best-fitting parameters and 68% confidence interval of the spherical gNFW profile and the compact radio source with power-law spectral index. The reference values for the spatial coordinates and the compact source flux are defined as in Table 2.3.

2.2.2 Comparison of the spherically symmetric SZ and X-ray profiles centered at the X-ray peak

In this section, I compare the radial pressure profiles inferred through the joint image-visibility reconstruction of the spherical gNFW model and from the independent analysis of *Chandra* X-ray data. I employ archival Chandra observations (OBSIDs: 3592, 13516, 13999, 14407). The 0.5 – 3.5 keV image is shown in the middle panel of Figure 2.1. I obtain from the X-ray data an estimate of the radial profile of the cluster electron pressure by multiplying the radial profiles of deprojected electron density and temperature distributions generated using the procedure described in Churazov et al. (2003). A plot of the thermodynamic profiles of RX J1347.5–1145 is shown in Figure 2.6. The pressure model determined using the SZ observations is overlaid in the top panel, and shows good overall agreement with the X-ray profile within the uncertainties of the two independent determinations. However, an excess in the pressure distribution derived from the X-ray data with respect to the SZ model can be seen at $\sim$ 30 arcsec from the center, roughly at the distance where the south-eastern substructure is located. Such modest discrepancy is not surprising, given that any departures from the spherical symmetry may affect differently the radial pressure profiles derived from X-ray and SZ data. Note, also, that even the relativistic correction alone could modify the normalisation of the derived Compton parameter y by around 6%, if the change of the temperature from 7 keV in the core to 20 keV some 20 – 30 arcsec away was properly taken into account.

The broad agreement between the radial pressure profiles from the independent X-ray and SZ analyses provides a partial validation of the joint image-visibility modelling. It also suggests that the perturbations present in the cluster gas are not so extreme as to affect dramatically the reconstruction of the pressure profile at all radii (see, e.g., Khedekar et al. 2013 for a discussion of biases arising from inhomogeneities in the gas within galaxy clusters).

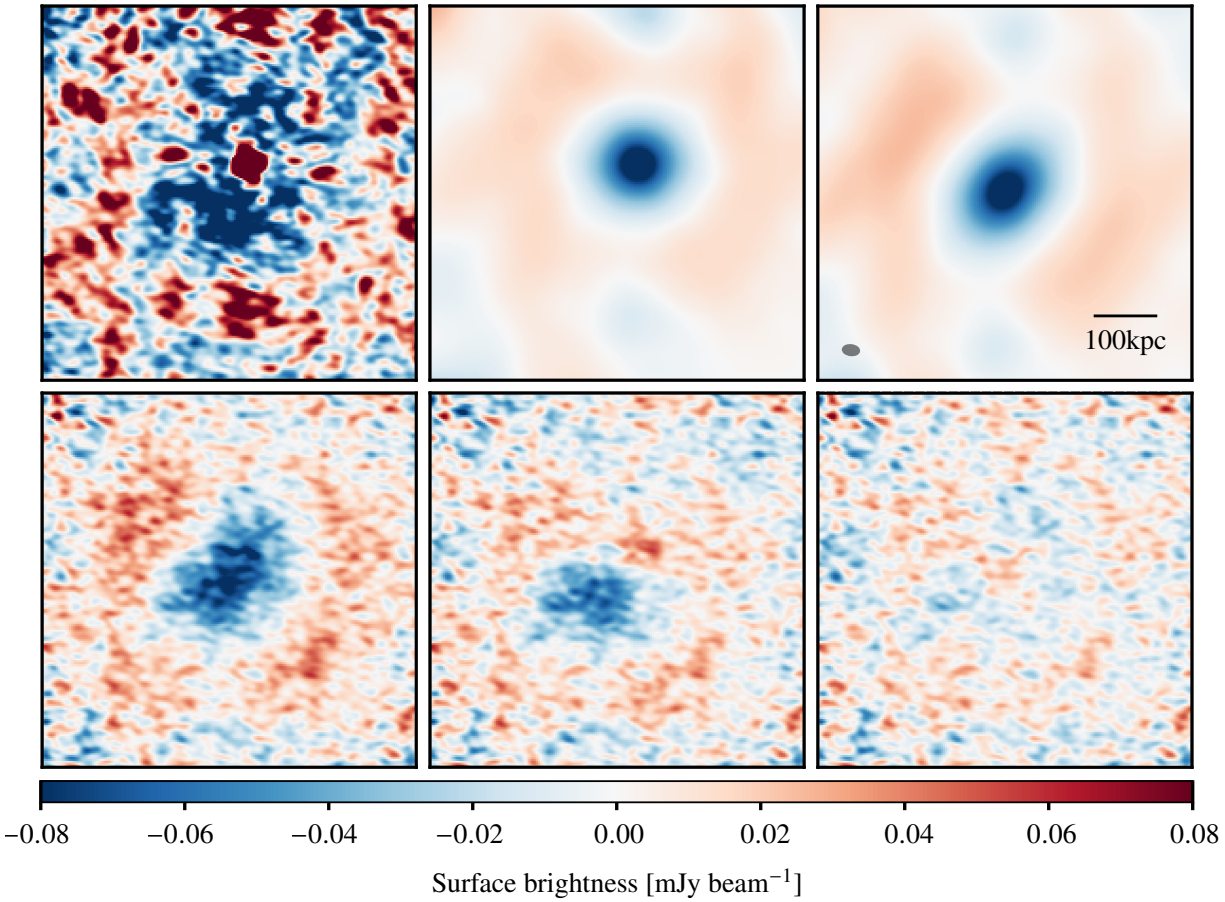

Figure 2.5: Images from the raw (top left) and point-source subtracted ALMA+ACA data (bottom left), X-ray centered spherical (top middle) and free-centroid ellipsoidal (top right) gNFW models and corresponding residual maps (bottom middle and right, respectively). All the images are the dirty maps of the corresponding visibilities, generated adopting a multi-frequency mosaic gridding approach with natural weighting of all the fields and spectral windows from both ACA and ALMA data. The resulting synthesised beam (4.11 arcsec × 2.44 arcsec at a position angle of 83.4°) and the reference spatial scale for the six maps are reported in the top right panel.

2.2.3 SZ-driven ellipsoidal model with free centroid

From the image of the X-ray surface brightness in Figure 2.1, it is evident that the peak of the X-ray emission is unambiguously associated with the cool and dense region around wBCG. Also, the pressure profile derived from the X-ray data (see Figure 2.6) clearly shows that the gas pressure is increasing towards the X-ray peak. The question arises whether one should expect a very prominent peak in the SZ signal at exactly the same location, which will then dominate the overall SZ signal. To answer this question I plot in Figure 2.6 the interpolated X-ray pressure profile $P(r)$ multiplied by r (dashed line). This quantity, $P(r) \times r$, characterises the contribution of a region with size $\sim r$ to the projected pressure map, i.e., the amplitude of a peak in the SZ

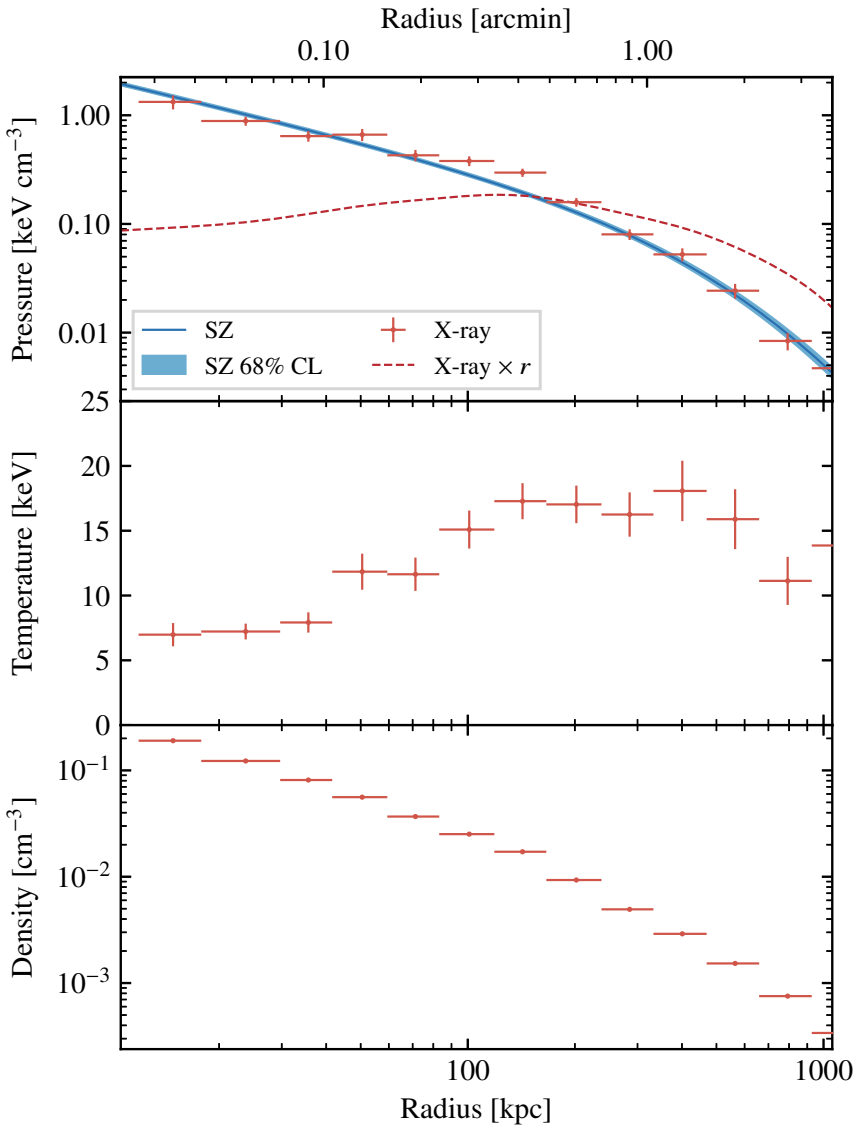

Figure 2.6: Azimuthally-averaged radial profiles of the deprojected thermodynamic properties of RX J1347.5–1145 based on *Chandra* X-ray data. The red, dashed line in the top panel represents the product of the radial distance and the pressure profile obtained by interpolating the deprojected pressure radial distribution. For a comparison, I also report the pressure model (blue line in the top panel) derived through the joint image-visibility analysis of the SZ observations discussed in Section 2.2.1.

images. It is found to be a growing function of the radius up to $r \sim 100$ kpc, implying that the central region is playing a sub-dominant role when compared to scales of the order of few hundreds of kiloparsecs in the projected pressure map. Considering that the typical inner slope for the pressure profile in cool-core clusters γ is less than 1, it is not surprising that no strong cusp is expected at the position of the cool core.

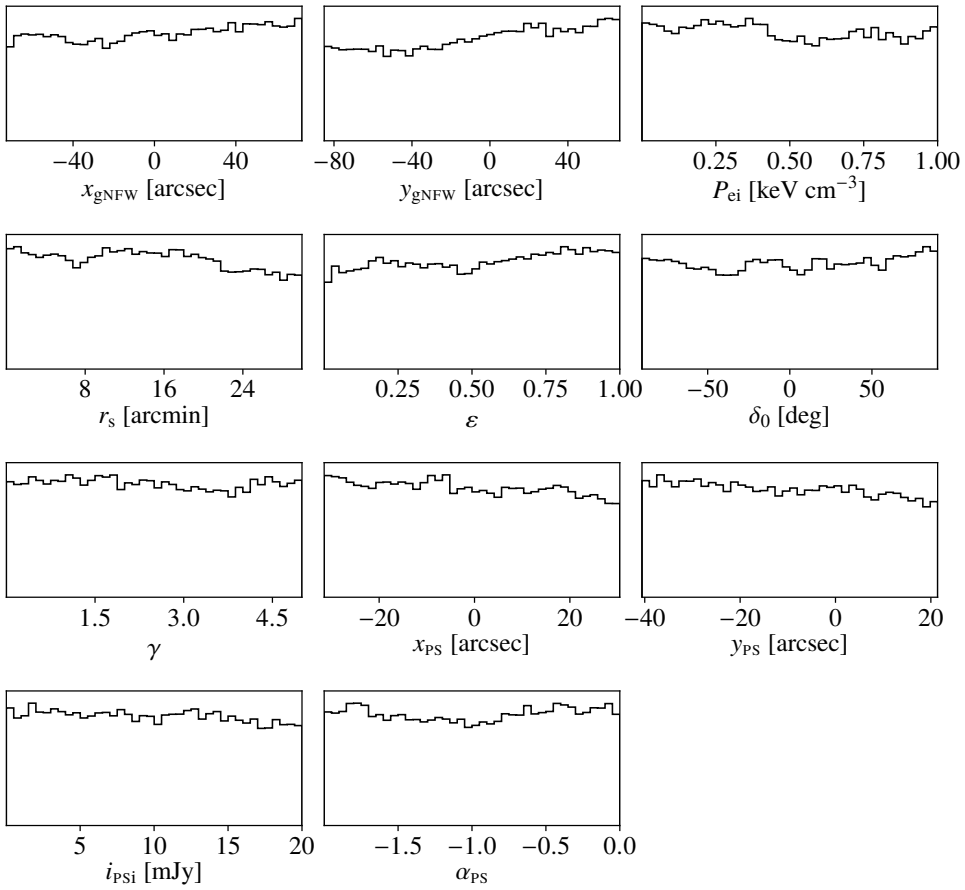

Figure 2.7: Same of Figure 2.3 but for the ellipsoidal model of Section 2.2.3.

The rather modest contribution of the core gas to the overall SZ effect signal makes the definition of a cluster centre from the sole inspection of RX J1347.5–1145 SZ images ambiguous. As seen when imaging the point source-subtracted visibilities in Figure 2.5, the distribution of the SZ signal is indeed fairly smooth across the cool-core region around wBCG. In fact, recent works generally agree that the SZ signal peaks at a location offset south-east of the X-ray surface brightness peak (e.g., Kitayama et al. 2016). I therefore relax all priors on the centroid position and the assumption of spherical symmetry and try to build a model for the pressure distribution based solely on the SZ data. I use the modelling set-up adopted in Section 2.2.1, but I substitute the spherical gNFW distribution, with centre fixed to the X-ray peak, with a free-centroid elliptical gNFW pressure profile, allowing for eccentricity and arbitrary orientation on the plane of the sky. The coordinates of SZ centroid are bounded to the combined ALMA+ACA mosaicked field of view by the introduction of uniform priors. Along with the pressure normalisation $P_{\rm ei}$ and the profile characteristic radius $r_{\rm s}$, I further allow the inner slope of the gNFW profile γ to vary. Again, the other two indices are fixed to the cool-core values of Arnaud et al. (2010). For this analysis, I now assume an electron temperature of 12.5 keV, estimated by averaging the X-ray temperature profile of Figure 2.6 within 1 arcmin from the position of the X-ray peak. Finally, I fit for the cylindrically integrated Compton y by assigning a Gaussian prior based on the value

Parameter	Units	Mean	16^{th} perc.	84^{th} perc.
x_{gNFW}	arcsec	5.62	5.39	5.87
y_{gNFW}	arcsec	−7.06	−7.34	−6.77
P_0	10^{-1} keVcm^{-3}	1.57	1.38	1.74
r_{s}	arcmin	2.39	2.31	2.52
ε	–	0.648	0.628	0.667
θ	degree	−36.2	−38.4	−34.1
γ	–	0.563	0.534	0.598
x_{PS}	10^{-2} arcsec	47.40	47.02	47.78
y_{PS}	10^{-2} arcsec	50.55	50.32	50.77
i_{PSi}	mJy	4.146	4.137	4.155
α_{PS}	–	−0.431	−0.465	−0.399

Table 2.5: Same of Table 2.4, but for the case of the ellipsoidal gNFW pressure profile.

derived from the *Planck* MILCA Compton y map. All the other free parameters of the gNFW model are assigned wide uninformative uniform priors. The specific details of the above priors on the model parameters are listed in Table 2.3. Again, the prior-only sampling shows no biases in the reconstruction of the model parameters due to the assumption on the corresponding prior distributions (Figure 2.7).

As with the previous case of the spherical profile, Figure 2.8 shows the posterior probability density function of the sampled parameters, while a summary of the best-fitting model parameters is reported in Table 2.5. The cluster pressure distribution appears to be described by a slightly eccentric profile. The inner slope of the gNFW model is found to be steeper than that reported by Arnaud et al. (2010) for both the universal and morphologically disturbed profiles, but still lower than for the cool-core sample of clusters. I tested this result by varying the intermediate and outer slopes, but found no significant changes in the estimated value of the inner parameter.

The map of the model-subtracted interferometric data, together with the image of the inferred best-fitting SZ distribution, is presented in the bottom panels of Figure 2.5. No residual structures highlighting possible overpressure in the intracluster medium within RX J1347.5–1145 are detected at a significant level with respect to the image noise. In particular, the residual amplitude of the SZ effect to the south-east is dramatically reduced when shifting the centroid away from the X-ray peak and allowing for ellipticity. This suggests that the SZ excess may be at least partially ascribed to purely geometric effects, which is a consequence of the intrinsic eccentricity of RX J1347.5–1145 in the inner $\sim$ 200 kpc region. It is worth noting that the centroid of the ellipsoidal pressure model is consistent with the position of the SZ peak reported by Kitayama et al. (2016). Since the presence of a strong local overpressure may easily result in a non-negligible offset between these positions, such fair agreement further suggests that the pressure structure may be more regular than could be derived from X-ray analyses.

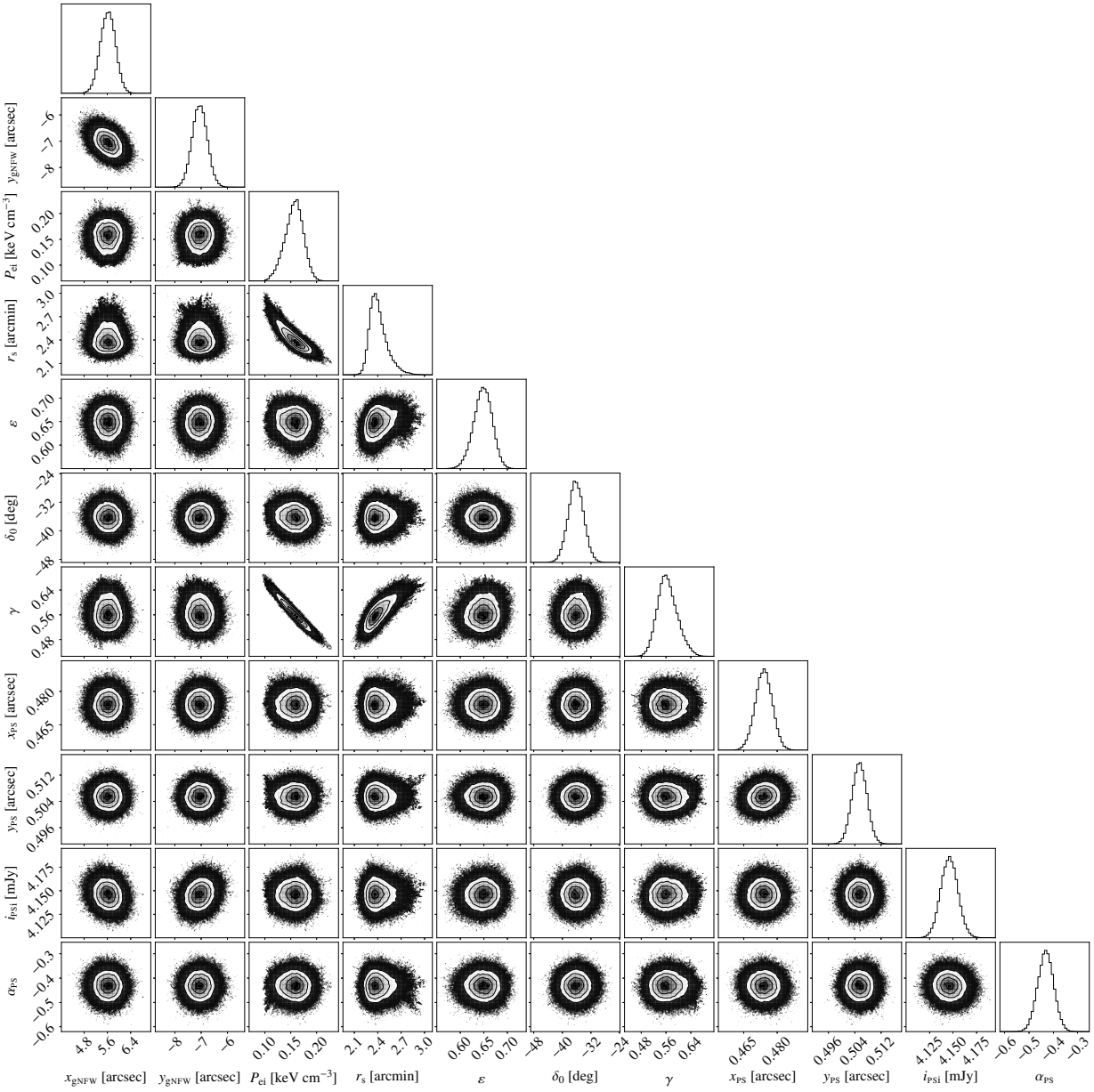

Figure 2.8: Same of Figure 2.4 but for the case of the ellipsoidal gNFW pressure profile. Due to the larger number of parameters, I had to increase the burn-in and sampling phases to 4000 and 8000 steps, respectively.

2.2.4 Compact radio source

I found that the reconstruction of the model for the central radio source is independent of the specific profile used to fit the underlying SZ signal. The position and the spectral index from the spherical and ellipsoidal profile fits are entirely consistent, while the discrepancy between the two estimates of the flux normalisation is within the flux calibration uncertainties of the

ALMA+ACA data. Moreover, the constraints on the central radio source are in good agreement with the parameters derived by Kitayama et al. (2016) using the same interferometric observations of this chapter, although the best-fitting model has a slightly steeper radio spectrum and larger normalisation at the same reference frequency of 92 GHz. Nevertheless, these differences are not enough to solve the tension with previous studies, which report fluxes of 4.9 ± 0.1 mJy at 86 GHz (CARMA; Plagge et al. 2013), 4.4 ± 0.3 mJy at 140 GHz and 3.2 ± 0.2 mJy at 240 GHz (Diabolo; Pointecouteau et al. 2001) against the corresponding estimates from the analysis presented in this chapter of respectively 4.29 ± 0.01 mJy, 3.48 ± 0.05 mJy, and 2.76 ± 0.09 mJy at 68% confidence level. The determination of the point-source parameters is principally driven by the interferometric data, and I assess that no significant bias is introduced as a consequence of a possible miscalibration of the ACA or ALMA measurements. For this reason, I repeat the above analysis on the ACA, ALMA and *Planck* observations, fixing all the model parameters to the best-fitting values of Table 2.3 but without marginalising over the scaling hyperparameters (see Sections 2.1.5 and 2.1.6). I exclude Bolocam from the test to avoid any systematics related to the unresolved radio source, while deriving a constraint on the scaling parameter mainly based on the cluster SZ signal. Since *Planck* data provide more frequency channels than parameters necessary to describe the SZ contribution, I assume any potential radio contamination is marginalised over as a result of the MILCA component separation. Further, the radio source flux is less than 2% of the total SZ flux on 15 arcmin scales (Equation 2.1), and residual radio source contamination is well within the statistical uncertainty of the *Planck* measurement. The modelling provides estimates of the *Planck* and ALMA+ACA scaling hyperparameters with ratio equal to 0.993 ± 0.038, therefore consistent with unity and supporting the general scenario that ascribes the discrepancies in the flux measurements to a long-term variability of the radio source (Kitayama et al. 2016). However, I have not been able to characterise any possible time dependencies due to the limited sampling over time provided by the observations used in the analysis.

2.3 Interpretation and discussion

The joint image-visibility SZ analysis has shown that it is possible to account for the SZ signal from the south-eastern SZ excess simply by allowing the centroid to vary freely, away from the X-ray peak, and by adopting an ellipsoidal model to describe the cluster pressure profile. This would imply that pressure distribution is more regular than one would derive when treating the south-eastern excess seen in the X-ray images as a significant overpressure with respect to the cluster cool core. While a fraction of the SZ effect from the south-eastern structure can certainly be ascribed to the elongated morphology of RX J1347.5–1145, it is important to consider that any signatures of overpressurized gas could possibly be pushed below the image noise level as a consequence of the overfitting of the SZ signal. This may indeed be a crucial issue arising due to the larger number of free parameters adopted when considering the free-centroid ellipsoidal model instead of the spherically symmetric pressure profile. It is worth highlighting that the two models are meant to describe different physical components, and a direct comparison based on statistical considerations would provide misleading results. To do this properly, the inclusion with the spherical model of an additional component to describe the south-eastern substructure would be

required. However, this would likely not provide a good description of RX J1347.5–1145, given the complex morphology of this merging cluster. Nevertheless, the lack of significant residuals in the free-centroid model-subtracted interferometric map represents an interesting result. The possibility of describing the pressure substructure observed south-east of the X-ray peak simply by means of a different model geometry implies the intracluster medium in RX J1347.5–1145 may be closer overall to pressure continuity than has been discussed in the previous studies. Specifically, this could be interpreted as hinting at a less violent merger history, or it could indicate that the disturbed X-ray morphology is a result of the merger being in a late stage. However, the SZ data employed in the analysis are not able to entirely rule out any of the above scenarios. Thus, I consider this result as further motivation for the interpretation I propose.

In order to gain a more thorough understanding of the physical properties of RX J1347.5–1145, I then compare the results from the SZ study to what can be inferred from *Chandra* X-ray imaging and spectroscopic analysis. Since the resolution of both Bolocam and *Planck* maps is too poor to allow for a direct comparison with X-ray data, I hereafter consider only the images generated using the ALMA+ACA data.

2.3.1 X-ray imaging constraints on the nature of the gas perturbations

The "X-ray arithmetic" method reported in Churazov et al. (2016) allows for the determination of the properties of small perturbations in X-ray images and, in particular, to differentiate between predominantly adiabatic and predominantly isobaric perturbations (see also Arévalo et al. 2016, Zhuravleva et al. 2016). This approach uses X-ray images in two different energy bands (typically 0.5-3.5 keV and 3.5-7.5 keV for *Chandra* data) and identifies in each image deviations relative to a suitable smooth underlying model. For adiabatically compressed regions, the fluctuations in density and temperature are correlated, while they are anti-correlated in the case of isobaric structures. As a consequence, the perturbations have different amplitudes in the two images, since the emissivity in the harder band is more sensitive to temperature variations. The relation between the amplitudes in two energy bands can be easily predicted for different types of perturbations, and it is straightforward to make a linear combination of two images that completely suppresses the perturbations of one type, leaving the amplitude of the other type unchanged. Note that the perturbations are identified in the maps divided by smooth underlying models, and therefore the prominence of a perturbation will depend on the accuracy of the model choice (for a similar case where the specific choice of the surface brightness model significantly affects the level of derived perturbations, see Bonafede et al. 2018).

The application of X-ray arithmetic to RX J1347.5–1145 is illustrated in Figure 2.9. The top right-hand panel shows the map from which adiabatic perturbations have been removed, revealing a prominent elongated structure to the south-west of eBCG. This coincides with the most prominent asymmetric excess seen in the X-ray image and, more clearly, in that divided by a spherically symmetric model centred at the X-ray peak (see top left- and bottom left-hand panels in the same figure). When calculating the best-fitting symmetric model, a 90° wedge to the south-east from wBCG was excluded from the analysis. The isobaric nature of this excess confirms the interpretation of this structure as low-entropy gas stripped from the subhalo associated with the eBCG and embedded in higher entropy ambient gas. Yet another isobaric structure is seen to the

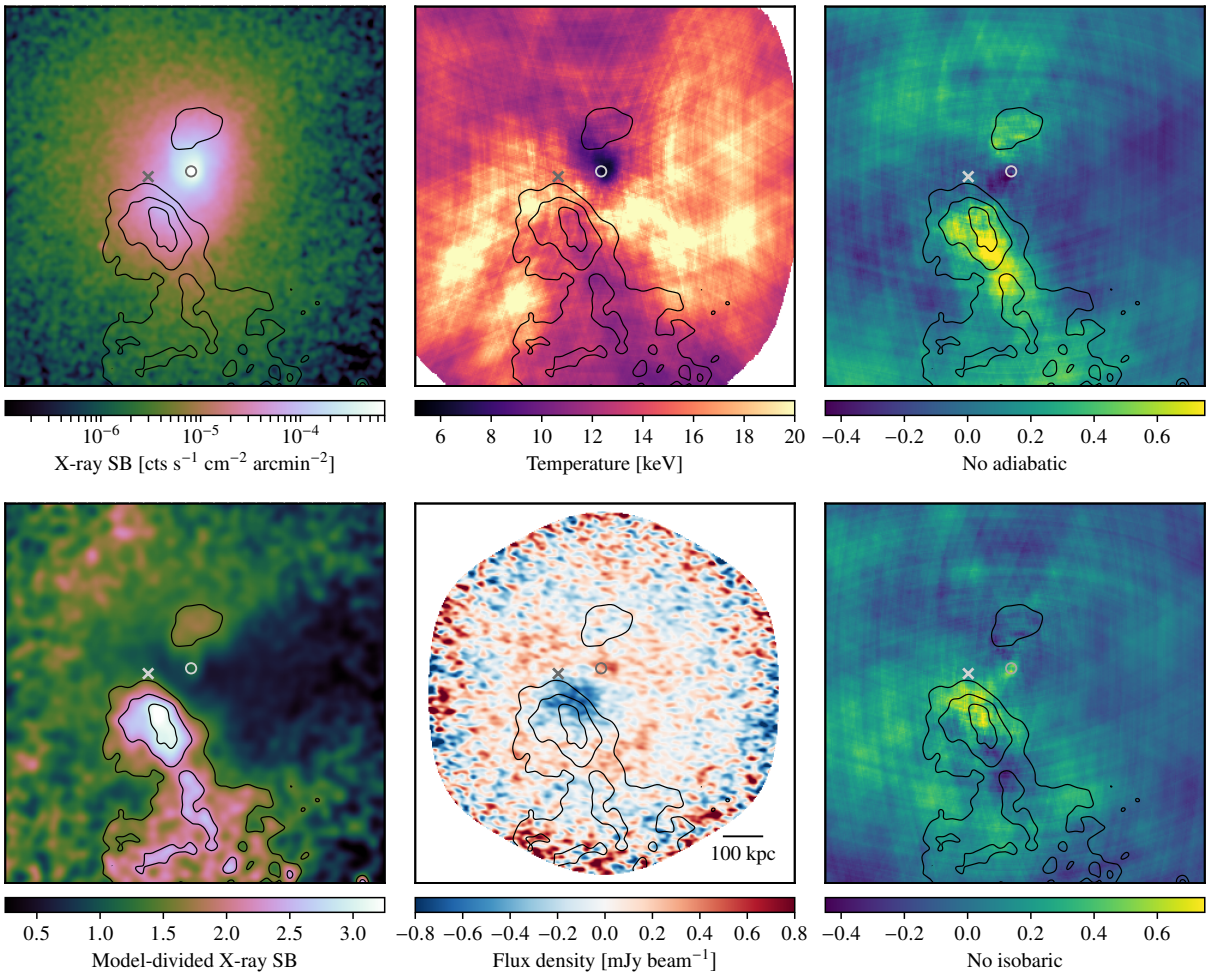

Figure 2.9: Raw (top left) and spherical model-divided (bottom left) X-ray surface brightness, temperature (top middle), spherical model-subtracted SZ effect (bottom middle), and X-ray images without adiabatic and isobaric perturbations (top and bottom right, respectively). The solid lines mark the significant structures in the model-divided X-ray map. As in Figure 2.1, the circle and the cross denote the positions of the brightest cluster galaxies wBCG and eBCG, respectively. I report in the bottom-middle panel the reference scale for all the above maps.

north of the wBCG, which could be due to subsonic sloshing of the gas.

The bottom-right panel shows the map free from isobaric perturbations. The remaining structures are less prominent than the isobaric ones. The most prominent adiabatically compressed region is located just in front of the stripped gas, halfway to the position of the eBCG. A comparison of these two images ("no adiabatic" and "no isobaric") suggests that the stripped gas forms an almost isobaric tail, but is moving with a substantial velocity to produce the overpressurized region ahead of it, which can also be identified in the temperature map. Thus, I do not expect the isobaric tail to produce any strong signal in the SZ map. The adiabatic region should instead show up as a local increase of the SZ signal. This is consistent with the presence of

the south-eastern excess in the model-subtracted SZ image (middle right-hand panel of Figure 2.5) when considering a spherically symmetric pressure model. In fact, the spatial correlation of the adiabatically compressed gas with the SZ structure is especially convincing when directly comparing the residual SZ substructures with isobaric-free X-ray maps (see Figure 2.9). However, the resulting residual is seen to be more extended than the adiabatically compressed region shown in the bottom right-hand panel of Figure 2.9, and to be slightly shifted towards the wBCG. I note, however, that this may arise as a consequence of the different line-of-sight dependencies of the X-ray and the SZ effect, which cause the latter to be generally observed in regions wider than X-ray emissions. On the other hand, the lack of any significant excess after subtracting the best-fitting ellipsoidal SZ model (bottom right-hand panel of Figure 2.5) supports the result that the south-eastern substructure is likely dominated by isobaric rather than adiabatic perturbations.

To make a crude estimate of the SZ signal expected from the south-eastern excess, I assume that it originates from a sphere of overpressurized gas with radius $\sim$ 90 kpc, shifted away from the wBCG by $\sim$ 130 kpc in the plane of the sky. Integrating the model of the X-ray emission based on the thermodynamic profiles shown in Figure 2.6, it is possible to infer that an excess $\delta I_{\rm X}/I_{\rm X} \sim 2$ observed in the X-ray surface brightness (see bottom left-hand panel of Figure 2.9) requires a density perturbation $\delta\rho/\rho \sim 1$. If one assumes that the perturbation is fully adiabatic, the pressure in the sphere would then be increased by a factor $[(\rho+\delta\rho)/\rho]^{5/3} \approx 3$. The corresponding enhancement of the SZ signal (integrated pressure profile along the line of sight in the direction of the sphere) is then $\delta y/y \sim 0.8$. If, instead, one uses the X-ray surface brightness excess $\delta I_{\rm X}/I_{\rm X} \sim 0.7$ seen in the "adiabatic" image (bottom right-hand panel in Figure 2.9), the expected SZ excess is $\delta y/y \sim 0.3$. These are of course only an order-of-magnitude estimates, given the complexity of the cluster and the assumptions made. Nevertheless, it can be compared to the value of $\delta y/y \sim 0.24$ obtained by dividing the ALMA+ACA residual map in the middle right-hand panel of Figure 2.5 by the spherical gNFW pressure profile and averaging over the circular region corresponding to the model gas sphere introduced before. This would suggest that, when subtracting the spherical model centred at the X-ray peak, it is more likely that the south-eastern substructure seen in the X-ray and SZ maps is predominantly related to isobaric rather than adiabatically compressed gas. Furthermore, this result is consistent with the previous one, that a simple, smooth ellipsoidal pressure profile is sufficient for describing at least partially the observed SZ excess. Anyway, it is worth noting that I do not interpret the nature of the south-eastern SZ structure to be wholly isobaric, but posit that the adiabatic component of the intracluster medium perturbations cannot be solely responsible for the observed structure. The clear spatial coincidence discussed above of the adiabatically compressed gas with the SZ excess would indeed support the possibility of a small contribution from the adiabatic perturbation. Of course, the value of fractional Compton y should be treated with caution, since a non-negligible level of contamination from the side lobes and the missing large-scale flux may reduce the actual amplitude of the SZ effect from the excess. Furthermore, the validity of the X-ray arithmetic methodology is in principle limited to small linear perturbations, while, in this study, I am employing it to characterise perturbations in a non-linear regime. As a result, the quantitative estimates of their amplitudes may be inaccurate, although still valid at the order-of-magnitude level. Moreover, I note that the method is able to provide the correct qualitative classification of the adiabatic or isobaric nature of the gas perturbations.

2.3.2 Gas velocities from X-ray temperatures

Additional information about the dynamical state of RX J1347.5–1145 can be derived by analysing its temperature distribution. The morphology of the X-ray temperature map, shown in the top middle panel of Figure 2.9, is reminiscent of the characteristic pattern produced by two subclusters moving with respect to each other with a non-zero impact parameter (see, e.g., Figure 7 in Ricker & Sarazin 2001, and Forman et al., in prep.). Indeed, the cooler structures to the north of the wBCG and to the south-west of the eBCG could be associated with the low entropy gas initially bound to infalling subhaloes and now trailing them. For the eBCG, the cooler gas has apparently already been stripped away. On the other hand, the hotter gas is observed to form an "S"-like pattern between the two subcomponents.

One can use the measured gas temperatures in order to constrain the velocities of the subhaloes. Indeed, for a body moving steadily through the homogeneous medium[3] and ignoring for simplicity the contribution of the gravitational potential, the initial gas temperature T_1 and the temperature $T_{\rm st}$ at the stagnation point in front of the body are linked by the Bernoulli equation,

$$\frac{v^2}{2} + \frac{\gamma_{\rm P}}{\gamma_{\rm P}-1}\frac{kT_1}{\mu m_{\rm P}} = \frac{\gamma_{\rm P}}{\gamma_{\rm P}-1}\frac{kT_{\rm st}}{\mu m_{\rm P}}, \tag{2.3}$$

where v is the velocity of the body, $\gamma_{\rm P}$ is the polytropic exponent, $\mu \approx 0.61$ is the mean atomic weight, and $m_{\rm P}$ is the proton mass. For subsonic motion with respect to the sound speed in the gas with temperature T_1, i.e., $c_{\rm s,1} = \sqrt{\gamma_{\rm P} k_{\rm B} T_1/\mu m_{\rm P}}$, the temperature gradually increases from T_1 far from the body to $T_{\rm st}$ at the stagnation point. Much of the temperature variation occurs over spatial scales comparable to the size of the body, where the velocity changes significantly. In terms of the temperature ratio, the Bernoulli equation yields

$$\frac{T_{\rm st}}{T_1} = 1 + \frac{\gamma_{\rm P}-1}{2}\mathcal{M}^2, \tag{2.4}$$

where $\mathcal{M} = v/c_{\rm s,1}$ is the body Mach number. When the velocity of the body is instead supersonic, a bow shock forms in front of it (see, e.g., Keshet & Naor 2016 or Zhang et al. 2019 for astrophysical applications). In this case, the gas temperature is T_1 ahead of the shock and jumps at the shock front to the temperature $T_{\rm sh}$, which is related to T_1 via the Rankine–Hugoniot condition

$$\frac{T_{\rm sh}}{T_1} = \frac{[2\gamma_{\rm P}\mathcal{M}^2 - (\gamma_{\rm P}-1)][(\gamma_{\rm P}-1)\mathcal{M}^2 + 2]}{(\gamma_{\rm P}+1)^2\mathcal{M}^2}. \tag{2.5}$$

Between the bow shock and the stagnation point, the temperature increases steadily from $T_{\rm sh}$ to $T_{\rm st}$.

It is then clear that the temperature ratio can be used to infer the gas velocity. A plot of the above relations between the two quantities for both subsonic and supersonic motions is shown in Figure 2.10. There, the velocity is scaled by the sound speed $c_{\rm s,2}$, based on $T_{\rm sh}$ (red curve) or $T_{\rm st}$ (black). In these units, the maximal values of $v/c_{\rm s,2}$ for $\gamma_{\rm P} = 5/3$ are $\sqrt{16/5} \approx 1.78$ based on the Rankine–Hugoniot condition and $\sqrt{3} \approx 1.73$ for the stagnation point (dashed horizontal lines in Figure 2.10).

[3] See Zhang et al. (2019) for the discussion of non-steady motion in a medium with pressure/density gradients

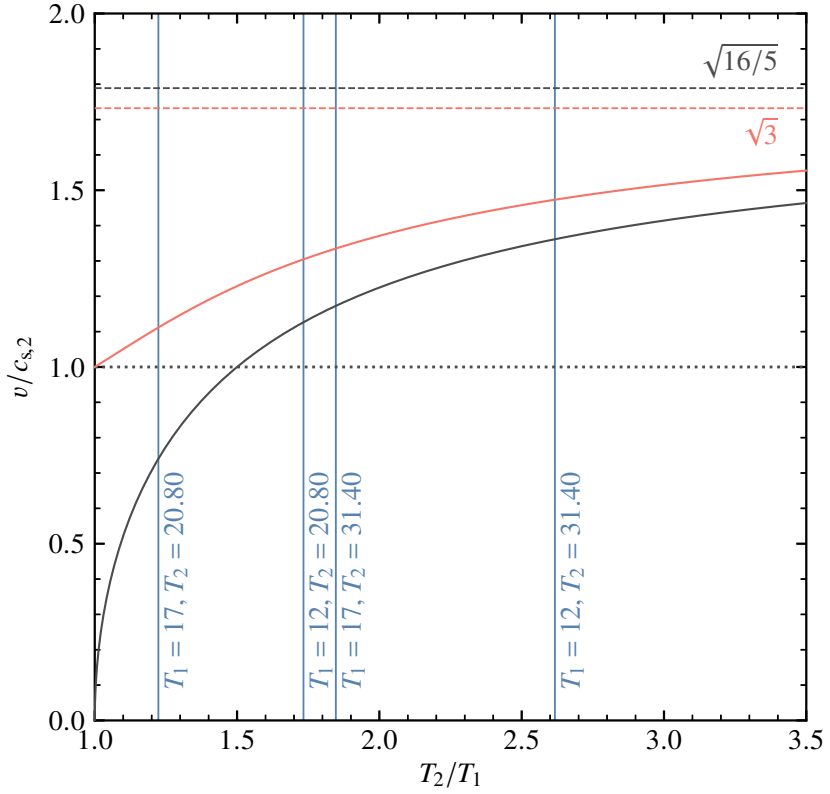

Figure 2.10: Relation between the temperature contrast and the body velocity for a steady motion in a homogeneous medium. T_1 is the upstream temperature far from the body, while T_2 is either the temperature at the stagnation point $T_{\rm st}$, or at the downstream side of the shock $T_{\rm sh}$. The body velocity is scaled by the sound speed in the gas with the temperature $T_2 = T_{\rm st}$ (black curve) and $T_2 = T_{\rm sh}$ (red curve). The blue vertical lines show the observational constraints coming from the *Suzaku* and *Chandra* data. See text for details. The intersections of the blue lines with the black and red lines show the velocity needed to provide the observed temperature ratio.

I first address the highest temperature gas, which should be associated with the compressed or shock-heated regions. The temperature map in Figure 2.9 suggests that $T \gtrsim 20$ keV in some regions (for various independent analyses of the X-ray data, see Gitti & Schindler 2004, Ota et al. 2008, Kreisch et al. 2016), which immediately implies that uncertainties on the temperature based on *Chandra* or *XMM-Newton* data are very large, especially on the upper side of the confidence interval. Better constraints are provided by the *Suzaku* satellite, which uses a combination of X-ray CCDs with an additional HXD instrument, sensitive to temperatures above 10 keV. Using *Suzaku*, Ota et al. (2008) found a hot component in the SE region with $T \sim 25$ keV. I note here that Ueda et al. (2018) found a higher temperature, $T \sim 29$ keV, for the hotter component in the SE region, although their procedure of fixing the temperature and the contribution of the "ambient" component, while scaling the model normalisation only by the area of the region, to derive the "excess emission" may bias the temperature high, since some of the volume along the line of sight is occupied by the hotter component. I have done several experiments by letting

the normalisation of the ambient component be free, which yields $T \sim 23$ keV. I emphasise again that the uncertainties of measuring the temperature of > 20 keV plasma with *Chandra* or *XMM-Newton* are very large. I therefore use only the results of *Suzaku*, $T = 25.3^{+6.1}_{-4.5}$ keV (for systematic uncertainties, see Ota et al. 2008).

Considerable uncertainty is associated with the choice of T_1, even though it is easier to measure lower temperatures with *Chandra*. Indeed, I have several options to choose from. For instance, I can simply use the radial temperature profile shown in Figure 2.6. At the distance of the south-eastern excess from the X-ray peak, the corresponding temperature is ~ 17 keV. Ueda et al. (2018) found a similar temperature of ~ 17.8 keV for the gas north-east of the excess region (ahead in their merger scenario; see region 2a in their Table 1). These values could be affected by the complicated temperature structure of the cluster. Alternatively, one can use a mass-temperature relation based on the lensing measurements to estimate T_1. To this end, I use the scaling relation from Vikhlinin et al. (2009), assuming that $M_{500} \approx 0.63 M_{200}$. For the mass of RX J1347.5–1145 $M_{200} \sim 1.5 \times 10^{15}\ h^{-1}\ M_\odot$ (Lu et al. 2010, Verdugo et al. 2012), the corresponding temperature is ~ 12 keV. However, if I use only the mass of the main subcluster $\sim 0.72 \times 10^{15}\ h^{-1}\ M_\odot$ (Ueda et al. 2018), I get ~ 7.6 keV. The latter value appears low, as the entire system is found to be permeated by higher gas temperatures, while the 12 keV gas can be observed in several places across the cluster. Therefore, I assume rather arbitrarily that T_1 is somewhere between 12 and 17 keV and ignore further uncertainties associated with it. Corresponding temperature ratios are shown in Figure 2.10 with the vertical lines. For $T_1 \sim 17$ keV, there are solutions that do not involve supersonic motions; the lowest velocity that can lead to $T_{\rm sh}$ at the lowest end allowed by *Suzaku* is ~ 2000 km s^{-1}. On the other hand, for $T_1 \sim 12$ keV the temperature ratio is larger than $\sim$2.6, implying that the gas velocities exceed ~ 4200 km s^{-1}.

Given that there are additional uncertainties associated with the temperature measurements (see, e.g., Ota et al. 2008), it is clear that neither subsonic, nor supersonic solutions, can be excluded by the X-ray temperature information alone.

2.4 Summary

In this chapter, I present first results of the analysis of heterogeneous measurements through simultaneous modelling of single-dish and interferometric observations of the SZ effect. The applicability of the joint image-visibility technique is demonstrated by modelling a mixture of single-dish and interferometric observations of the well-known galaxy cluster RX J1347.5–1145. I here briefly summarise the central results presented in this chapter.

- The combined analysis of ALMA, ACA, Bolocam, and *Planck* data has been crucial for probing the pressure profile of RX J1347.5–1145 over a wide range of spatial scales and, therefore, for deriving a comprehensive reconstruction of its thermodynamic properties. Simultaneously, it has allowed for fully exploiting the resolution and compact source sensitivity of an interferometer for modelling and removing astronomical source contamination.

- The global pressure distributions inferred from the X-ray analysis and from the joint SZ modelling, when constrained to be centered about the X-ray centroid, are in good

agreement out to ∼1 Mpc (see Figure 2.6). Along with providing validation for the modelling technique, this confirms the cool-core nature of the central region of this cluster as derived in previous independent analyses. Further, consistent with previous works, the imaging of the model-subtracted visibilities shows the presence, south-east of the X-ray peak, of a region overpressurized with respect to the cluster cool-core model. This has been generally identified as shock-heated gas.

- On the other hand, the reconstruction of the global pressure profile using no prior information on the geometry of the cluster has shown that a smooth, ellipsoidal pressure model, with centroid falling between the two BCGs, is able to describe the observed SZ signal. In this case, there is no strong evidence of shock-induced perturbations in the pressure distribution. This suggests the pressure distribution may be less disturbed than previously inferred from either the sole X-ray analysis or the X-ray-motivated SZ model. However, while no significant residual is apparent after subtraction of the best-fitting model, it is impossible to entirely rule out the presence of a shock discontinuity in the thermal pressure.

- By investigating the thermodynamic properties of RX J1347.5–1145, I find that the south-eastern substructure seen in the X-ray image is predominantly due to isobaric rather than adiabatic perturbations. Presumably, these perturbations are related to gas stripped away from the infalling subcluster during its passage through RX J1347.5–1145 intracluster medium. As no strong perturbations in the pressure distribution should be expected, this is consistent with the lack of significant residuals in the SZ map after subtracting the best-fitting ellipsoidal model. Further, this alleviates the need for highly supersonic velocities required to explain the south-eastern excess as entirely due to shock-induced gas compression. However, the analysis of the gas temperature distribution inferred from X-ray data cannot unambiguously differentiate between the possible subsonic or supersonic nature of the infall of the subcluster. Further, adiabatically compressed gas is still observed ahead of the southern isobaric region.

Future, more sensitive SZ data spanning a broader range of spatial scales will be required to conclusively measure or constrain any merger-induced pressure discontinuities, while deeper multiband kinematic SZ and X-ray micro-calorimetric data could test the assumption that the gas motion is predominantly in the plane of the sky. Deeper multiband SZ observations could also constrain the hottest intracluster medium temperatures, which are out of reach for current X-ray instruments, through measurements of the distortion in the thermal SZ due to relativistic corrections. Given ALMA's limited ability to probe scales larger than an arcminute at frequencies $\gtrsim$ 100 GHz, kinematic and relativistic SZ constraints will require improved single-dish photometric SZ imaging. The eventual extension of the modelling method to the combined reconstruction of both the SZ signal and X-ray emission will further improve the modelling of the thermodynamics of galaxy clusters, as well as provide insights into the internal structure of the intracluster medium, for example, gas clumpiness, line-of-sight extent, and turbulence. Furthermore, this will allow for the proper treatment of the relativistic corrections to the SZ effect.

The work presented in this chapter made use of Bolocam and Planck data hosted on the NASA/

IPAC Infrared Science Archive, which is operated by the Jet Propulsion Laboratory, California Institute of Technology, under contract with the National Aeronautics and Space Administration. The following ALMA data were further used: ADS/JAO.ALMA#2013.1.00246.S. ALMA is a partnership of ESO (representing its member states), NSF (USA) and NINS (Japan), together with NRC (Canada), MOST and ASIAA (Taiwan), and KASI (Republic of Korea), in cooperation with the Republic of Chile. The Joint ALMA Observatory is operated by ESO, AUI/NRAO and NAOJ. The scientific results are based in part on data obtained from the Chandra Data Archive. The research has made use of software provided by the Chandra X-ray Center (CXC) in the application packages CIAO, CHIPS, *and* SHERPA.

Chapter 3

An ALMA+ACA measurement of the shock in the Bullet Cluster

The content of this chapter was originally published as ***Di Mascolo, L.****, Mroczkowski, T., Churazov, E., Markevitch, M., Basu, K., Clarke, T. E., Devlin, M., Mason, B. S., Randall, S. W., Reese, E. D., Sunyaev, R., and Wik, D. R., 2019, A&A, 28, A100*

Mergers play a crucial role in the formation of galaxy clusters, which are situated at intersections of the Cosmic Web. These spectacular events can have a profound impact on the intracluster medium and the galaxies within these environments (see, e.g., Kravtsov & Borgani 2012). Mergers provide large-scale astrophysical laboratories for plasmas where the mean free path can be substantial (see, e.g., Markevitch & Vikhlinin 2007) and for measuring the self-interaction cross-section of dark matter (Markevitch et al. 2004, Randall et al. 2008, Wittman et al. 2018, Tulin & Yu 2018). For instance, the very existence of dark matter was conclusively demonstrated through the merging cluster 1E0657–56, or "Bullet Cluster", which exhibits spatial offsets between its baryonic and total mass peaks in the X-ray and gravitational lensing maps (Clowe et al. 2006, Bradač et al. 2006, Paraficz et al. 2016).

Key to identifying merging clusters is the detection of shocks in the intracluster medium. A "textbook example of a bow shock" is observed in the X-ray image of the Bullet Cluster (Markevitch et al. 2002). Using 500 ks of *Chandra* X-ray data, Markevitch (2006) reported a Mach number $\mathcal{M} = 3.0 \pm 0.4$ for the western, most-prominent shock in the Bullet Cluster, an estimate largely determined by the density jump conditions. I also note that Shimwell et al. (2015) revealed a second shock, on the eastern (opposite) side of the cluster, which we do not consider here.

Here I present deep, continuum ALMA observations, sensitive to the thermal SZ effect (Sunyaev & Zeldovich 1972 and Section 1.1.1), of the main shock in the Bullet Cluster. These observations include data from both the main ALMA 12-meter array and the 7-meter ACA. As the thermal SZ effect is linearly sensitive to the line-of-sight integral of the electron thermal pressure (see Chapter 1.1.1), these observations complement the X-ray constraints on plasma density and, less accurately, electron temperature, yielding a ground-based, millimetre-wave view of the shock properties.

All the results presented in this chapter have been derived assuming a flat ΛCDM cosmology with $\Omega_m = 0.30$, $\Omega_\Lambda = 0.70$, and $H_0 = 70.0$ km s^{-1} Mpc^{-1}. At the redshift of the Bullet Cluster ($z = 0.296$), 1″ corresponds to a physical scale of 4.41 kpc. Unless stated differently, all reported best-fitting parameters and their respective uncertainties are obtained from the 50$^{\text{th}}$, 16$^{\text{th}}$, and 84$^{\text{th}}$ percentiles of the marginalised posterior distributions, corresponding to the 68% credibility interval of the distribution.[1]

3.1 Data and analysis overview

3.1.1 ALMA+ACA observations

As part of ALMA Cycle 2 operations ALMA and the ACA observed the Bullet Cluster for a total of 3.1 and 5.9 hours of integration time respectively in Band 3 (project ID: 2013.1.00760.S, PI: T. Mroczkowski). These wideband observations span the frequency range 84 – 100 GHz in four 2 GHz-wide spectral windows, centred at approximately 85, 87, 97, and 99 GHz. The strategy employed consists of a single, deep observation centred approximately on the nose of the shock front, as inferred from the X-ray observations (Clowe et al. 2006, Markevitch 2006). The ALMA and ACA observations were respectively performed in 4 and 11 separate executions spanning 2014, obtaining root-mean-square noise levels of approximately 5 μJy and 45 μJy respectively (as measured in naturally-weighted imaging), and a synthesised beam with a main lobe of 4.01″ × 3.07″ FWHM (P.A. 81°).

I re-reduced the data using the ALMA pipeline (Shinnaga et al. 2015, Humphreys et al. 2016) in `CASA` 4.7 (McMullin et al. 2007), producing results consistent with the previous calibration using the script provided on data delivery. The re-reduction provided a cross-check of the earlier reduction, and was necessary due to backwards-compatibility issues and bug fixes in subsequent `CASA` releases. The data were calibrated using the default calibration strategy of the ALMA observatory, which has nominal uncertainty ≤ 5%. However, since the flux calibrators, which included quasars, differed for each execution, I performed a manual cross-check of the values for the designated flux calibrators as well as the phase calibrators, finding they were consistent for the dates spanned by the observations.

As broadly discussed in the previous chapters, the interferometric view of the sky leads to two major complexities: an incomplete sampling in Fourier space even for the modes accessible to the array, and the lack of recovery of angular scales larger than those corresponding to the shortest projected distances between array elements. Based on the *uv*-space coverage of the ALMA and ACA data presented here, the largest recoverable scales are respectively ≈ 40″ and ≈ 55″. As detailed in the next section, I choose to forward-model the observed SZ signal using X-ray-motivated priors to address such issues. Again, to avoid known deconvolution biases intrinsic to the CLEAN algorithm (Högbom 1974, Thompson et al. 2015 and discussion in Section 1.2.2), I perform the analysis directly in *uv*-space. I extend the interferometric SZ analysis techniques presented in the Appendix A to allow for fitting pressure discontinuities due to shocks. The

[1] In the case of Gaussian uncertainties, the 50$^{\text{th}}$ percentile corresponds to the median value, and the 16$^{\text{th}}$ and 84$^{\text{th}}$ percentiles correspond to -1σ and $+1\sigma$ deviations from this.

approach builds upon the work of Basu et al. (2016), but incorporates several advances in the parameter-space sampling technique as well as more sophisticated and flexible models allowed by the deeper X-ray and SZ observations. In brief, I build an image-space model of the SZ signal by integrating numerically the three-dimensional pressure distribution model, and applying the proper SZ frequency scaling. The dependence of the SZ signal on the electron temperature is taken into account when modelling the SZ spectrum (Itoh & Nozawa 2004, Chluba et al. 2012, and end of Section 3.1.2). The pixel scale is chosen to fulfil the Nyquist sampling criterion for the smallest scales probed. The SZ model image is then Fourier transformed and sampled to the position of the sparse interferometric data. The resulting synthetic visibilities are then employed in combination with the observed ones to evaluate the likelihood at each step of the Bayesian inference procedure.

However, I choose not to model the raw post-calibration data, instead binning the data in each spectral window following the optimal averaging scheme described in Hobson et al. (1995). This is crucial for gaining a significant reduction in data volume and hence computational time.

3.1.2 SZ model

A summary of the model priors introduced in this section can be found in Table 3.1. I test for biases in the parameter reconstruction arising from the specific choice for the distribution of priors by performing a *prior-only* run, which is done by setting the likelihood to a constant value regardless of the model fit (see Section 2.2). As expected, the result of this test simply returns the input distribution of priors.

Shock front

The common approach employed in the study of X-ray observations of shock fronts consists in describing them as spherical sectors within a specific region of the cluster image. This takes advantage of the image-space nature of the X-ray data to select a spatial region narrow enough to allow one to locally approximate the shock front as spherical. However, among the complexities of studying interferometric data is the difficulty of applying any spatial masking. This would entail convolution of the visibilities, inducing a non-trivial correlation between them. To avoid this, a complete two-dimensional model of the observed field is then required.

In order to allow more freedom in the description of the shock front than in the case of a spherical model, I describe the shock front as an axially-symmetric hyperbolic surface (see the dashed line in Figure 3.1), with central axis coincident with the direction of the merger and lying in the plane of the sky. Since the interferometric data alone cannot constrain the line-of-sight distribution of pressure, I consider the curvature of the front to be symmetric with respect to the line-of-sight and the plane-of-sky direction. Although this is likely a reasonable assumption, any deviations from cylindrical symmetry may introduce non-negligible systematic errors into the results. In particular, the derived downstream pressure $P_{\rm e,ds}$ will be related to the true pressure $P^{\rm true}_{\rm e,ds}$ as $P_{\rm e,ds} \approx P^{\rm true}_{\rm e,ds}\left(\ell^{\rm true}_{\rm LoS}/\ell_{\rm LoS}\right)$, where $\ell_{\rm LoS}$ and $\ell^{\rm true}_{\rm LoS}$ are respectively the assumed and true line-of-sight extents of the shock front. I present specific estimates for the ratio $\ell^{\rm true}_{\rm LoS}/\ell_{\rm LoS}$ when discussing the results in the next sections.

Param.	Prior	Details	Ref.
gNFW pressure model			
R.A.	delta	$\mu = 6^{\rm h}58^{\rm m}35\overset{\rm s}{.}6$	1
Dec.	delta	$\mu = -55°57'10\overset{''}{.}8$	1
$P_{\rm e,us}$	split-normal	$\mu = 8.65 \cdot 10^{-3}$ keV cm^{-3} $\sigma = (0.92 \cdot 10^{-3}$ keV cm^{-3}, $1.29 \cdot 10^{-3}$ keV cm$^{-3})$	2
$T_{\rm e,us}$	split-normal	$\mu = 9.40$ keV $\sigma = (1.00$ keV, 1.40 keV)	2
Shock front			
R.A.	split-normal	$\mu = 6^{\rm h}58^{\rm m}15\overset{\rm s}{.}5$ $\sigma = (2\overset{''}{.}3,\ 2\overset{''}{.}5)$	3
Dec.	split-normal	$\mu = -55°56'58\overset{''}{.}26$ $\sigma = (8\overset{''}{.}6,\ 8\overset{''}{.}3)$	3
θ	split-normal	$\mu = -98\overset{\circ}{.}14$ $\sigma = (4\overset{\circ}{.}52,\ 3\overset{\circ}{.}98)$	3
$\mathcal{M}$	uniform	min = 1, max = 10	–
α	uniform	min = −10, max = 0	–
Calibration			
$\kappa_{\rm ACA}$	normal	$\mu = 1.00$, $\sigma = 0.05$	–
$\kappa_{\rm ALMA}$	normal	$\mu = 1.00$, $\sigma = 0.05$	–

Table 3.1: Priors on the model parameters employed in the analysis. Here, μ and σ are the mode and the standard deviation of the probability distributions. The two values reported for σ in the case of split-normal priors represent the standard deviations of the lower and upper halves of the corresponding distributions. The parameters $(\text{R.A.}, \text{Dec.})_{\rm gNFW}$, $P_{\rm e,us}$, and $T_{\rm e,us}$ respectively define the centroid of the gNFW profile describing the upstream pressure distribution, and the upstream pressure, and the temperature normalisation (see Section 3.1.2 for a discussion). For the shock front, I use its nose position $(\text{R.A.}, \text{Dec.})_{\rm shock}$ as the reference point. Further, θ and $\mathcal{M}$ are the orientation of the shock axis and the Mach number (Section 3.1.2), while α is the slope of the downstream power-law profile (Section 3.1.2). Finally, $\kappa_{\rm ACA}$ and $\kappa_{\rm ALMA}$ are the ACA and ALMA calibration hyperparameters (Section 3.1.2).
(1) Clowe et al. 2006; (2) X-ray model from Markevitch 2006 and Markevitch & Vikhlinin 2007; (3) This analysis (see Section 3.1.2).

It is worth noting that the line-of-sight ratio is expected to scale approximately with the square root of the curvature radius of the shock surface, i.e., $\ell^{\rm true}_{\rm LoS}/\ell_{\rm LoS} \approx \sqrt{r_{\rm PoS}/r_{\rm LoS}}$ for line-of-sight

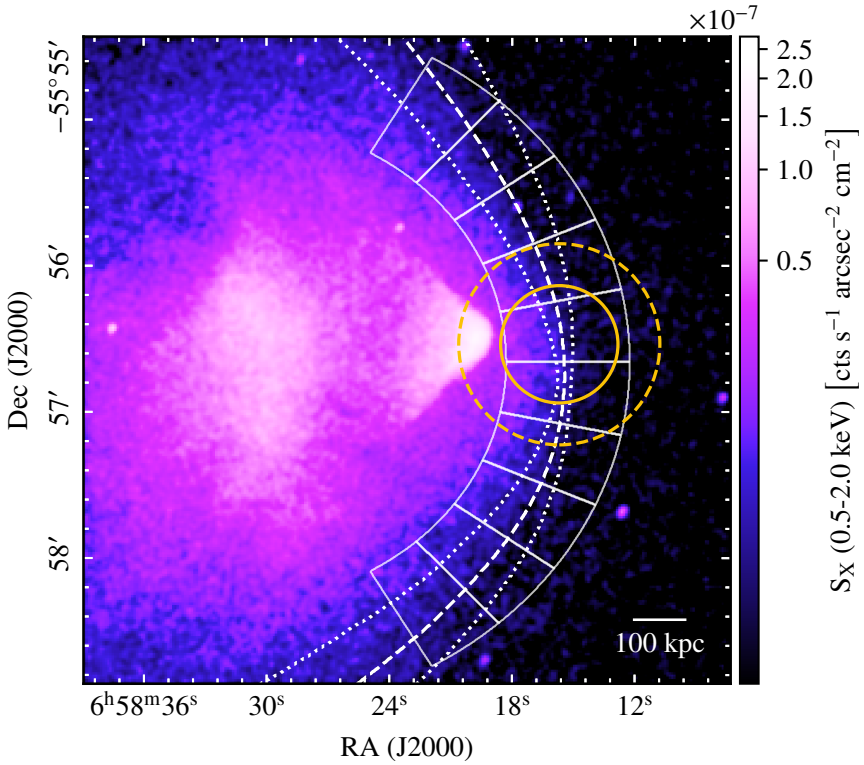

Figure 3.1: Cut-out of the 0.5 – 2.0 keV *Chandra* X-ray surface brightness map of the Bullet Cluster. The solid wedges represent the sectors employed to derive the hyperbolic shape best-matching the shock front geometry. The maximum-a-posteriori model is shown as a dashed line, while the dotted contours indicate the corresponding 95% credible interval. Further, the dashed and solid yellow circles denote respectively the ACA and ALMA full-width-at-half-maximum fields of view. For reference, the upstream and downstream gas lie respectively west (right) and east (left) of the shock front.

and plane-of-sky curvatures radii $r_{\rm LoS}$ and $r_{\rm PoS}$. In fact, as shown in Figure 3.1 and later on in this chapter, the available ALMA+ACA data (i) only probe a small region near the tip of the shock and (ii) any extended structures in this region are effectively filtered out. Therefore, a model that includes a jump of pressure across the shock front and is smooth otherwise should capture the most of the information contained in the ALMA+ACA data. To this end, I represent the electron pressure distribution $P_{\rm e}(\boldsymbol{x}, \ell)$ as a combination of two spatially smooth components, $P_{\rm e,0}(\boldsymbol{x}, \ell)$ and $P_{\rm e,1}(\boldsymbol{x}, \ell)$, where their sum is

$$P_{\rm e} = (1 - f_{\rm ds})\, P_{\rm e,0} + f_{\rm ds}\, P_{\rm e,1}. \tag{3.1}$$

Here $f_{\rm ds} \equiv f_{\rm ds}(\boldsymbol{x}, \ell)$ is equal to 1 in the downstream region and 0 in the upstream region (i.e., is a Heaviside step function). I note both that here and below, for simplicity, I omit the explicit coordinate dependence of P_e or y. Rearranging the terms and integrating along the line of sight, it is possible to obtain

$$y \propto \int P_{\rm e,0}\, {\rm d}\ell + \int (P_{\rm e,1} - P_{\rm e,0})\, f_{\rm ds}\, {\rm d}\ell. \tag{3.2}$$

Since the first term in the above expression corresponds to a smooth, large-scale pressure distribution its contribution to y is filtered out from the ALMA+ACA data. Moreover, the function $(P_{e,1} - P_{e,0})$ in the second term is also spatially smooth and would be filtered too without the step function f_{ds}. Therefore, the signal $\tilde{y}$ measured by ALMA+ACA in the vicinity of the shock tip is effectively defined by the second term in equation 3.2, which is set by the pressure jump at the shock front and the length-scale of the downstream region. Thus,

$$\tilde{y} \propto \int (P_{e,1} - P_{e,0})\, f_{ds}\, d\ell \approx (P_{e,ds} - P_{e,us})\, \ell_{LoS} = \Delta P_e\, \ell_{LoS}, \tag{3.3}$$

where ℓ_{LoS} is the line-of-sight extent of the probed post-shock region, and $P_{e,us}$ and $P_{e,ds}$ are the electron pressures measured just outside and inside the shock front, respectively (Section 3.1.2). Therefore, ALMA+ACA data effectively constrain a product of the electron pressure difference at the shock ΔP_e and the physical size of the region ℓ_{LoS}. The latter quantity can be easily determined if the merger is in the plane of the sky and the shock front possesses rotational symmetry. If the shape of the front can be approximated by a sphere with a radius R, then along the symmetry axis $\ell_{LoS} \approx \sqrt{2rh}$, where $h \ll r$ is the distance from the tip of the shock. While the calculations in this chapter were done without these simplifying assumptions, the equation 3.3 is useful to estimate the uncertainty introduced by the (unknown) geometry of the shock along the line of sight. In particular, if the curvatures in the sky plane r_{PoS} and along the line of sight r_{LoS} differ, the estimate of the pressure difference ΔP_e, which assumes $r_{LoS} = r_{Pos}$, will be biased by a factor $\sqrt{r_{LoS}/r_{PoS}}$ (the same argument is discussed in Wang et al. 2018).

A preliminary attempt to determine the shape of the shock front using SZ data alone shows that the parameters defining its geometry are heavily degenerate, and the small extent of the ALMA+ACA field of view does not allow for meaningful constraints. I would like to note this is a consequence of the sole parametrization of the shock geometry, since ALMA+ACA has proven to be able to identify edge positions with a beam-scale precision (Basu et al. 2016). I therefore derive a description of the morphology of the bow shock by finding the hyperbola that best describes the discontinuity observed in the *Chandra* surface brightness map. Analogous to Ueda et al. (2017), I find the best-matching shock geometry by minimising the variance of the X-ray image within a defined region. The model is assumed to be simply given by a step function in which the discontinuity has a hyperbolic shape. The values of the function inside and outside the front itself are set equal to the mean photon counts in the respective regions of the X-ray image. In order to gain better leverage on the azimuthal geometry of the shock front, I further split the region in several angular sectors (see Figure 3.1). The resulting maximum-a-posterior model for the hyperbolic surface is then employed for describing the profile of the shock front in all the following analyses. To account for a possible mismatch in the shock coordinates (e.g., due to astrometry errors) from the *Chandra* modelling with respect to ALMA+ACA, I allow for some additional freedom in the nose coordinates $(\mathrm{R.A.}, \mathrm{Dec.})_{shock}$ and axis orientation θ. Specifically, I assign each one priors based on the respective marginalised posteriors derived in the X-ray-matching step described above. Any asymmetry in the recovered parameter uncertainties is modelled by means of split-normal distributions (Wallis 2014).

Apart from its morphology, the main parameter defining the shock is the ratio of downstream to upstream pressure at the jump itself. In practice, for a fixed line-of-sight geometry, the available

ALMA+ACA data are mainly sensitive to the *absolute difference* of the downstream and upstream electron pressures near the nose of the shock, i.e., $\Delta P_e = P_{e,ds} - P_{e,us}$; the SZ signal associated with the large-scale distribution of the gas is effectively filtered out (see, e.g., Basu et al. 2016, and discussion in Section 3.2.2). Thus, the modelling of the ALMA signal remains only weakly sensitive to the assumed large-scale model. The immediate downside is the *relative* pressure jump at the shock, $x_P = P_{e,ds}/P_{e,us} = 1 + \Delta P_e/P_{e,us}$, which serves as a proxy for $\mathcal{M}$, is poorly constrained by the interferometric SZ data alone. In fact, due to the lack of information on the pressure normalisation, the marginalised posterior distribution of the Mach number inferred when performing an SZ-only analysis are found to entirely span the corresponding prior interval. To get a meaningful measure of the pressure jump from the ALMA+ACA data, I therefore employ an X-ray-informed analysis of the ALMA+ACA SZ observations as in Section 3.3 of Basu et al. (2016), and set the upstream electron pressure $P_{e,us}$ to the value derived by modelling the *Chandra* data in a narrow sector centred on the shock nose (Markevitch 2006).

I do not include any model components describing the "bullet" itself (i.e., the contact discontinuity, or cold front) or the subtle additional cold front between the bullet and the main shock reported by Markevitch (2006) and Markevitch & Vikhlinin (2007). The former lies outside the ALMA field of view, precluding any interesting constraints on the pressure difference (or lack thereof) across the cold front, while the latter is intrinsically faint, and is expected to be in thermal pressure equilibrium. For simplicity, I thus assume these features to have a negligible effect on the measurements of the shock itself, and therefore ignore them. Further, I assume a single power-law profile for the downstream electron pressure (see below). A future analysis, joint with X-rays, will allow more model freedom for trying to build a description of such features.

Bulk pressure distribution

To model the pressure distribution in the downstream region, I employ a power law radial profile with slope α, centred along the merger axis at a distance from the shock nose equal to the front curvature radius r_c,

$$P_e(r) = x_P P_{e,us} (r/r_c)^{\alpha}. \tag{3.4}$$

On the other hand, I consider the pre-shock pressure distribution to be relaxed, thus to be described by a spherical gNFW profile (Nagai et al. 2007):

$$P_e(r) \propto M_{500}^{a_P} P_{500}\, P_0\, (c_{500} r/r_{500})^{-c}\, [1 + (c_{500} r/r_{500})^{a}]^{(c-b)/a}, \tag{3.5}$$

where r_{500} and P_{500} are functions of M_{500}, the total mass contained within an average overdensity 500× the critical density of the Universe at that redshift (Arnaud et al. 2010). I constrain M_{500} so that the gNFW model always reproduces the X-ray value for the upstream pressure, $P_{e,us}$. For the main results reported here, the pressure normalisation P_0, concentration parameter c_{500}, mass-dependence index a_P, and slopes (a, b, c) are fixed to the values reported in Arnaud et al. (2010) for the universal pressure profile. However, I show below that the results for $\mathcal{M}$ are insensitive to the choice of gNFW parametrisation and position of the gNFW model centroid. I therefore simply fix the gNFW centroid's coordinates $(\mathrm{R.A.}, \mathrm{Dec.})_{gNFW}$ to the position of main lensing κ-map peak inferred by Clowe et al. (2006), which I note does not coincide with the centre of the post-shock profile.

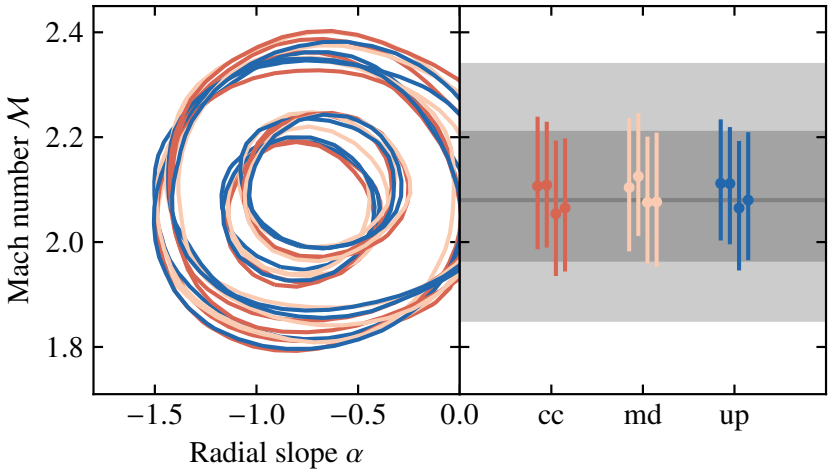

Figure 3.2: Bivariate posterior density function (left panel) for the inferred Mach number $\mathcal{M}$ and slope of the downstream pressure distribution α for a set of upstream pressure profiles and respective centroids. To facilitate comparison, the best-fitting $\mathcal{M}$ estimates are also plotted (right panel). I consider three different cases for the underlying gNFW profile by setting the slopes equal to the values reported in Arnaud et al. (2010) for the cool-core (cc; red), morphologically-disturbed (md; peach), or ensemble (up; blue) cluster samples. For each of them, the distribution centroid is then fixed to a number of different positions: far downstream and far upstream (right panel, left and mid-left points), respectively to arbitrary distances of 10′ east and 3′ west of the X-ray-derived shock nose coordinates; APEX-SZ centroid (mid-right point; Halverson et al. 2009); peak of the κ-map (right point; Clowe et al. 2006). In all the above cases, I assumed instantaneous shock heating of the electrons. The grey line in the right panel denotes the corresponding best-fitting $\mathcal{M}$ reported in Section 3.2.1, while the darker and lighter bands the respective 68% and 95% credibility intervals.

Though pressure perturbations driven by the primary merger are confined to be within the shock front, it is possible for the passage of its associated dark matter component to affect, through infall, the intracluster medium ahead of the shock (Springel & Farrar 2007). This may undermine the choice of the universal gNFW profile, reliable in the case of relaxed clusters, when describing the bulk pressure distribution. I tested against possible systematics introduced by this assumption. I found no significant deviations in the reconstructed parameters after changing either the slopes of the profiles or the position of the assumed centroids. The same applies to the structure of the gas on the downstream side as long as it is smooth, even though it may differ from expectations for a solid body moving through homogeneous fluid (see, e.g., Zhang et al. 2019). The outcome of the above tests is summarised in Figure 3.2. The net result is that, as a consequence of the interferometric filtering, the shock model is largely sensitive to the pressure conditions right at the front, and not to the properties of the bulk pressure distribution (see Section 3.2.2). Thus, I consider wide uninformative priors on both the Mach number and post-shock slope, and marginalise over the latter.

In order to account for the high temperatures measured in the system, relativistic corrections to the SZ spectrum (Itoh & Nozawa 2004) are included in the modelling. In fact, variations in the measured SZ signal of the order of 5% up to 15% are expected for an electron gas with temperature ranging from 9 keV to 30 keV as measured from the X-ray data. As for $P_{\rm e,us}$, I employ an X-ray-motivated prior on the upstream temperature $T_{\rm e,us}$. In addition, I incorporate the 5% uncertainties on the ACA and ALMA flux calibration by introducing normalisation hyperparameters $\kappa_{\rm ACA}$ and $\kappa_{\rm ALMA}$ (see Section 2). For all the modelling runs presented in the following sections, $\kappa_{\rm ACA}$ and $\kappa_{\rm ALMA}$ have been found to not deviate significantly from unity.

Given the plane-of-sky geometry of the merger involving the Bullet Cluster, any contribution from the kinematic SZ effect (Sunyaev & Zeldovich 1980) to the observed signal due to the motion of the single subclusters should be subdominant with respect to the thermal SZ effect. In fact, if I assume the velocity $v \approx 3000$ kms^{-1} inferred from the shock Mach number (Springel & Farrar 2007) to be measured with respect to the CMB rest frame and the merger direction to be oriented by around 8 degrees with respect to the plane of sky (Markevitch et al. 2004), I find that the contribution of the kinematic SZ effect to the total SZ signal from the post-shock region would be of the order of 3% of the corresponding thermal component. This would induce a systematic error on the estimate of the Mach number $\mathcal{M}$ lower than 2%. Given the small effect as well as the lack of robust constraints on the merger proper velocities and orientation, I then decide to not include the kinematic SZ effect in the model, keeping the merger axis aligned with plane of sky (see Section 3.1.2).

3.1.3 Implementation details

As noted earlier, the modelling algorithm and its specific implementation are detailed in Chapter 2 (see also references therein). However, I improved the posterior sampling algorithm by adopting the dynamic nested sampling by Higson et al. (2017). In particular, I employ the pure-Python implementation provided by `dynesty` (Speagle 2020).

3.2 Results

3.2.1 Instantaneous electron-ion temperature equilibration

I first consider a model for the shock front under the standard assumption of an instantaneous electron-ion temperature equilibration, i.e., $T_e = T_i$, at the shock front. This is consistent with the *Chandra* analysis by Markevitch (2006), who derived $\mathcal{M}_{\rm X} = 3.0 \pm 0.4$ from the density jump, and measured an electron temperature jump as expected if electrons reach the average post-shock temperature near-instantly. A more recent analysis of the same *Chandra* data by Markevitch (in prep.) provides an electron density jump $x_{\rm n} = 2.86 \pm 0.16$, assuming instantaneous electron heating ($T_{\rm e,ds} \approx 30$ keV) for converting the X-ray surface brightness to the density jump by accounting for the different emissivity in the post- and pre-shock regions (see, e.g., Ettori 2000 for a discussion about X-ray brightness modelling in the presence of temperature gradients). This corresponds to $\mathcal{M}_{\rm X} = 2.74 \pm 0.25$. The slight difference from the older estimate is due to a

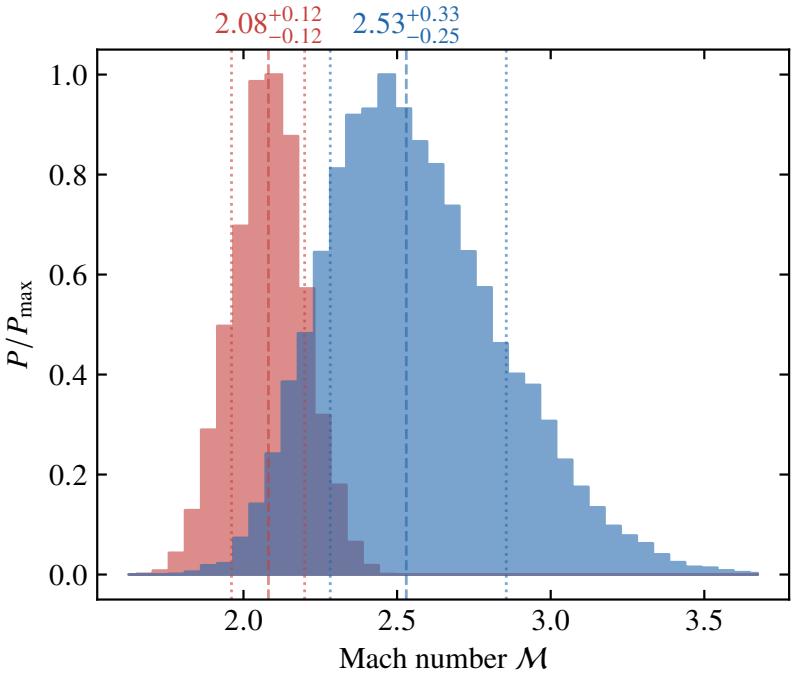

Figure 3.3: Marginalised posterior distributions for the shock Mach number $\mathcal{M}$ derived under the assumptions of instantaneous (red) and collisional (blue) electron-ion equilibration. The dashed and dotted lines indicates the median of the posterior distributions and the 68% credible intervals, respectively.

better-centred shock model and the inclusion of the azimuthal decline in $x_{\rm n}$ for angles away from the shock nose when projecting along the line of sight (as in Wang et al. 2018), based on the amplitude of the density jumps measured from the X-ray data in different sectors of the shock (Markevitch, in prep.).

The assumption of instantaneous heating implies that the nominal Rankine–Hugoniot condition can be used to relate $\mathcal{M}$ to the measured amplitude of the electron pressure jump $x_{\rm P}$ relative to the upstream value $P_{\rm e,us}$ as

$$\mathcal{M} = \left[\frac{(\gamma+1)\, x_{\rm P} + (\gamma-1)}{2\gamma} \right]^{1/2} . \tag{3.6}$$

Here, γ is the polytropic exponent, which I assume to be $\gamma = 5/3$, appropriate for non-relativistic fully-ionised gas. I further allow for the azimuthal variation of $\mathcal{M}$ along the shock front, whose scaling with the azimuthal angle is derived using the same density jump decline discussed above. The omission of such azimuthal dependence would cause the Mach number to be averaged down with respect to its maximum value due to the effect of the wings with lower $\mathcal{M}$. For the results provided in this and the following sections, I estimate that the inclusion of the X-ray-based model for the azimuthal variation of the shock pressure jump increases the value of the inferred Mach number by only 5-7%. However, more severe effects should be expected for observations with larger field of views, which would include values from farther in the wings.

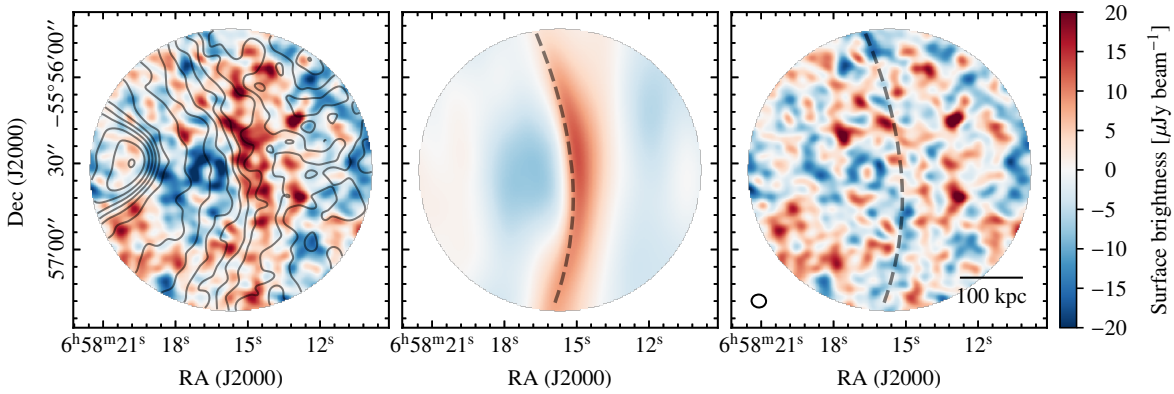

Figure 3.4: Dirty images of the raw (left), model (middle), and residual (right) ALMA+ACA interferometric data. They are generated by jointly gridding the ACA and ALMA data using a multi-frequency natural weighting scheme. For reference, this provides a synthesised beam of $4.07'' \times 3.01''$ FWHM (P.A. 81°; bottom-left corner of right panel). I cut off the fields at the 0.2 gain level of the joint ALMA+ACA antenna pattern. To better highlight the large-scale shock features, I avoid correcting for the primary beam attenuation and apply an additional 30 kλ taper. I note that the model subtraction is performed directly in Fourier space. The dashed line in the centre and right panels indicate the inferred position of the shock front. X-ray contours are overlaid on the left panel from Figure 3.1. I also note the positive signal at the shock front is not due to an increment of the SZ signal; rather it is an artifact of the high-pass filtering effects of ALMA+ACA (see also Figure 3.5).

I obtain $\mathcal{M} = 2.08^{+0.12}_{-0.12}$ (Figure 3.3). While the model relies on the X-ray priors on the pre-shock pressure and temperature, the derived Mach number is inconsistent at a 2.4σ level with the X-ray estimate $\mathcal{M}_{\rm X} = 2.74 \pm 0.25$. Projection effects may play a non-negligible role in biasing the SZ-based measurement of the Mach number. However, a strong ellipticity of the shock front shape $\ell^{\rm true}_{\rm LoS}/\ell_{\rm LoS} \lesssim 0.6$ (see Section 3.1.2) would be required to bridge the gap between SZ and X-ray estimates. In reality, an even larger ellipticity would be necessary, given that the X-ray estimates would also be affected by geometry, albeit with a different dependence. Another potential source of bias is the X-ray-motivated prior on the upstream pressure, which comes from deprojected density and temperature estimates, used to compute the relative pressure jump. While the definition of a centroid for X-ray deprojection remains ambiguous, I found only extreme choices would alter the results significantly. A joint-likelihood X-ray+SZ analysis may be required to find a consistent geometry that fully reconciles such discrepancies.

3.2.2 Collisional electron-ion temperature equilibration

Here I consider the possibility that the electron and ion temperatures do not equilibrate instantaneously in cluster shocks (i.e., $T_{\rm e} \neq T_{\rm i}$ immediately inside the shock front; see, e.g., Fox & Loeb 1997, Markevitch 2006, Russell et al. 2012, Wang et al. 2018). Ions carry the majority of the gas bulk kinetic energy in collisionless shocks, and are heated dissipatively on scales comparable to their gyro-radii, while electrons might remain much colder (Vink et al. 2015), unless there is some

process that equilibrates the ion and electron temperatures. The upper limit on the equilibration time scales is set by Coulomb collisions (Zeldovich & Raizer 1966), which for the downstream density and temperature in the Bullet Cluster is long ($\sim$ few 10^8 yr), occurring over a distance comparable to the offset between the shock and the cold front.

Under the assumption of conservation of the enthalpy flux, electrons equilibrate with ions to the Rankine–Hugoniot downstream temperature at a rate driven by Coulomb collisions (Fox & Loeb 1997)

$$\frac{\mathrm{d}T_\mathrm{e}}{\mathrm{d}t} = \frac{1}{t_\mathrm{eq}} \left(1 + \frac{n_\mathrm{e}}{n_\mathrm{i}}\right) \left(x_\mathrm{T} T_\mathrm{e,us} - T_\mathrm{e}\right), \tag{3.7}$$

where t_eq is the Coulomb collisional time-scale (Spitzer 1962), n_e and n_i are respectively the electron and ion densities, and x_T is the temperature ratio across the shock front. To build the SZ model, I convert the above equation in terms of the distance from the shock front by means of the downstream gas velocity $u_\mathrm{ds} = (\mathcal{M}/x_\mathrm{n})\, c_\mathrm{us}$, with c_us given by the upstream sound speed. Furthermore, I assume that electrons are first heated adiabatically (Vink et al. 2015), so that the electron temperature immediately inside the shock front equals $x_\mathrm{n}^{\gamma-1} T_\mathrm{e,us}$. As required by the conservation of charge neutrality across the shock front, the density jump x_n is also set to follow the Rankine–Hugoniot condition. In this case, the pressure jump x_P cannot be directly related to $\mathcal{M}$ as in Equation 3.6, and instead must be derived as the product of the density and temperature ratios at each three-dimensional model coordinate.

In the case of collisional equilibration, I find $\mathcal{M} = 2.53^{+0.33}_{-0.25}$ (Figure 3.3). This is consistent with $\mathcal{M}_\mathrm{X} = 2.57 \pm 0.23$, coming from the *Chandra* X-ray brightness fit if one uses the adiabatic-compression post-shock temperature ($T_\mathrm{e,ds} \approx 20$ keV) to convert to the density jump (Markevitch, in prep.). Unfortunately, due to the severe filtering of large spatial scales as well as the limited field of view, I am not able to put any significant constraint on the specific equipartition time-scale when treating t_eq as a free parameter. Instead, I find that assuming the electron-ion equilibration to be driven by Coulomb collisions is practically equivalent to setting $t_\mathrm{eq} = \infty$.

For illustrative purposes, I present in Figure 3.4 the dirty images of the raw ALMA+ACA data employed in the analysis, the interferometric model corresponding to the collisional electron-ion equilibration scenario, and the respective model-subtracted data. As shown in the right panel, it is not possible to identify residuals that differ at a significant level from noise-like features.

The analogous image for the instantaneous case is visually identical to Figure 3.4, and therefore is not shown. This is evident in Figure 3.5, where it is not possible to identify any significant difference between the filtered SZ models for the instantaneous- and collisional-equilibration scenarios. This confirms that the ALMA+ACA data are only sensitive to the properties of the pressure distributions near the shock edge, thus providing a direct estimate of the pressure difference across the shock front, i.e., ΔP_e rather than x_P. Moreover, the result is found to be practically independent of the specific assumption about the underlying gNFW profile, which is entirely filtered by the interferometric response (Figure 3.5).

The fact ALMA+ACA is only sensitive in practice to the electron pressure difference ΔP_e across the shock is also reflected in the lack of any significant difference between the Bayesian evidences of the instant equilibration and adiabatic heating models ($\Delta \log \mathcal{Z} = 1.30^{+0.71}_{-1.48}$). In fact, given that I cannot observe any large-scale feature in the SZ signal induced by the slow increase of

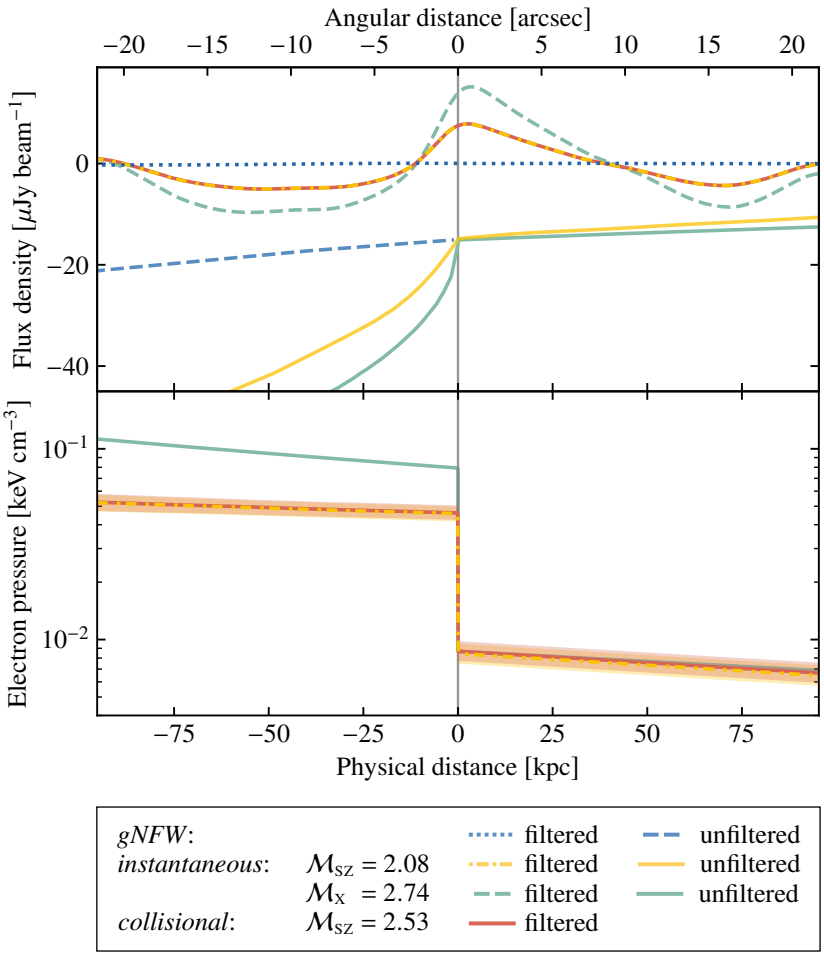

Figure 3.5: The figure provides a comparison of SZ signal profiles (upper panel) and the corresponding electron pressure profiles (lower panel) across the shock nose. The vertical grey line denotes the position of the shock front. I note that the upper panel contains both unfiltered input model fits for the SZ signal and the corresponding filtered (observed) profiles (see legend for details). As discussed in Section 3.2.2, the instantaneous (dash-dotted yellow) and collisional (solid red) shock models are indistinguishable after the spatial filtering of the interferometric ALMA+ACA observation, reflecting the fundamental limitation of ALMA+ACA to constrain any large-scale ($\gtrsim 1'$) component of the SZ signal. Again, I note that while I measure a decrement due to the SZ effect, the filtered (observed) profiles can exhibit both positive and negative excursions (analogous to the Gibbs phenomenon; see, e.g., Bracewell 1978). For comparison, I also report the input unfiltered model (solid yellow) for the instantaneous equilibration, and both the raw and filtered underlying gNFW profile (dashed and dotted blue lines, as noted in the legend). I also present the X-ray expectation for both the filtered and raw SZ signal profiles (dashed and solid green lines) and corresponding pressure profiles that I would expect for the case of instantaneous equilibration, using the value $\mathcal{M}_{X} = 2.74 \pm 0.25$ derived from fits to the X-ray data.

the post-shock electron temperature in the case of collisional equilibration, the different heating scenarios practically differ only in the way I convert the pressure difference to an estimate of the shock Mach number $\mathcal{M}$.

I recall here a subtle cold front is observed in the *Chandra* X-ray image between the shock and the bullet boundary, ~ 15 arcsec east from the shock. Since the total pressure across a cold front is expected to be approximately continuous, this was not included in the modelling of the downstream pressure profile. In fact, no apparent signature of such feature can be distinguished in the ALMA+ACA SZ observation. However, because the flow of the post-shock gas would not cross the cold front, it is unlikely that any electron-ion temperature non-equilibrium would extend past it. If indeed there is an electron-proton temperature difference in the post-shock region, I should expect the electron temperature (and, hence, pressure) to reach its equilibrium value. This would in turn result in a discontinuity in the SZ signal in the direction of the front itself. Future, more sensitive ALMA observations may search for such a feature.

3.3 Summary

In this chapter, I further demonstrate the ability of using deep, high-resolution ALMA+ACA observations of the SZ effect to characterise shocks in merging clusters (see, for comparison, Basu et al. 2016). For this purpose, I studied the SZ effect across the shock in the Bullet Cluster, chosen as it is widely regarded as the "textbook example" of a cluster merger bow shock.

The application of the interferometric modelling technique – using X-ray-motivated priors – has allowed for placing constraints on the electron pressure discontinuity across the shock. Assuming a Rankine–Hugoniot shock adiabat, the measured pressure jump implies a Mach number $\mathcal{M} = 2.08^{+0.12}_{-0.12}$, which is significantly lower than the one derived from *Chandra* data using the same geometric assumptions ($\mathcal{M} = 2.74 \pm 0.25$). An interesting physical possibility to reconcile the two measurements is to allow that the electron and ion temperatures do not equilibrate instantly after the shock passage has heated the electrons adiabatically. For a given Mach number, this would lower the post-shock electron temperature and thus the observed electron pressure jump. The Mach number would then become $\mathcal{M} = 2.53^{+0.33}_{-0.25}$, in agreement with the X-ray estimate that assumes the adiabatic temperature jump for conversion between the X-ray brightness and density. I note that *Chandra* X-ray data constrain the gas density (from which the Mach number is derived) and electron temperature across the shock separately, and its post-shock temperature prefers instant equilibration over adiabatic heating of the electrons (at $\sim 2\sigma$ confidence; Markevitch 2006). However, while *Chandra* is free from ALMA+ACA interferometric limitations and can probe the upstream and downstream gas directly, the Bullet post-shock temperature is above the range where *Chandra* can measure electron temperatures reliably, and hence suffer significant systematic uncertainties.

To summarise, ALMA+ACA has proven to provide a clean measurement of the differential jump in pressure due to the shock, and, in combination with data that can access larger scales, can provide compelling constraints on shock properties such as the Mach number. In particular:

- Interferometric observations cleanly measure the projected pressure jump due to the shock. However, due to the inherent spatial filtering of ALMA and the ACA, which recover scales

$\sim 0.5-1.1'$ in Band 3 (compared to θ_{500} $\sim 10'$, corresponding to r_{500} for the Bullet Cluster), X-ray priors on both the model geometry and upstream pressure are necessary in order to infer $\mathcal{M}$. On the other hand, the combination of SZ observations covering a broader range of spatial scales (i.e., from $0.1''-30'$) could provide an SZ-only view of the shock properties.

- Once the geometry is fixed, the key quantities which drive the analysis and the interpretations of the results are the pressure difference across the shock front, the normalisation of the pre-shock pressure, and the independent X-ray estimates of $\mathcal{M}$. I show their statistical uncertainties are small enough to allow for differentiating between the instantaneous and adiabatic heating scenarios. Nevertheless, neither model is unambiguously preferred. Although the two scenarios result in SZ-based estimates for $\mathcal{M}$ that deviate one from the other by $\approx 2\sigma$, I find that the difference of the respective Bayesian log-evidence is not significant enough to completely rule out one versus another.

- I extensively tested the modelling choices — varying the geometry, pre- and post-shock pressure slopes, and underlying pressure distribution — and find the results to be robust for a broad range of possible assumptions motivated by the X-ray analyses. However, the model does not fully describe the complex morphology observed in the X-ray surface brightness. Together with the uncertainties on the three-dimensional morphology of the cluster, this may limit the ability to elucidate the nature of electron heating across the shock front.

Together, these illustrate the fundamental complementarity of X-ray and SZ effect observations in the study of the physics of galaxy clusters. It is then clear that a simultaneous, joint-likelihood fitting of the SZ and X-ray data on the Bullet Cluster, extending the approach of incorporating X-ray information in the form of priors (see the discussion in Section 3.1.2, and Section 3.3 of Basu et al. 2016), would benefit the understanding of the overall morphology of the galaxy cluster, as well as provide further insights into the physical mechanisms for shock heating of the intracluster medium. A forthcoming work will present the results of a full joint-likelihood analysis of interferometric SZ and X-ray observations, as well as single-dish SZ measurements, building on the methodology discussed in Section 2. Meanwhile, upcoming results from NuSTAR (Wik et al. in prep) will better access the high photon energies corresponding to the high temperatures inferred from *Chandra*. Further, the number of observations of shocks with unambiguous geometry and sufficiently high Mach number that allow the detection of deviations from instantaneous electron heating is limited. Thus, along with improved modelling, observations of a larger sample of cluster shocks will be needed to improve our understanding.

This work made use of the following ALMA data: ADS/JAO.ALMA#2013.1.00760.S. ALMA is a partnership of ESO (representing its member states), NSF (USA) and NINS (Japan), together with NRC (Canada), MOST and ASIAA (Taiwan), and KASI (Republic of Korea), in cooperation with the Republic of Chile. The Joint ALMA Observatory is operated by ESO, AUI/NRAO and NAOJ.

Chapter 4

Verification with the ACA: Localisation and Cluster Analysis

The content of this chapter is based on the work originally published as ***Di Mascolo, L.****, Mroczkowski, T.,Churazov, E., Moravec, E., Brodwin, M., Gonzalez, A., Decker, B. B., Eisenhardt, P. R. M., Stanford, S. A., Stern, D., Sunyaev, R., Wylezalek, D., 2020, A&A, 638, A70*

Galaxy cluster richness has long been demonstrated to provide an observationally inexpensive proxy for cluster mass (see, e.g., Rykoff et al. 2012, Andreon 2015, Saro et al. 2015, Geach & Peacock 2017, Rettura et al. 2018, Gonzalez et al. 2019). Being practically independent of the specific dynamical state of galaxy clusters, properly calibrated mass–richness relations play a key role in obtaining mass estimates in lieu of data that could directly probe the mass distribution of a cluster. For cluster candidates discovered through optical and infrared selection criteria such as richness, it is essential to verify that the observed galaxy overdensities cannot be ascribed to spurious effects (e.g., line-of-sight projection of galaxies belonging to different haloes). Central to this aim is confirming the presence of a hot X-ray emitting intracluster medium heated by gravitational infall and nearly in virial equilibrium. X-ray confirmation, which has been the traditional tool for probing the intracluster medium, becomes exceedingly difficult and observationally challenging at high redshift due to cosmological dimming. I note, however, that at $z \gtrsim 1$ the dimming is expected to weaken due to evolution in the X-ray luminosity for a given mass (Churazov et al. 2015).

The thermal SZ effect (Sunyaev & Zeldovich 1972 and Section 1.1.1) offers an alternative, redshift-independent way to confirm the presence of the intracluster medium. I here provide a first test of the capabilities of the ACA in providing an SZ confirmation of cluster candidates identified in wide-field surveys. In particular, I consider a first pilot sample of the observational programme, *Verification with the ACA – Localisation and Cluster Analysis* (VACA LoCA), aimed at providing cluster verification and localisation of the intracluster gas within galaxy clusters selected from the Massive and Distant Clusters of WISE (Wright et al. 2010) Survey (MaDCoWS; Gonzalez et al. 2019).

All results discussed in this chapter have been derived in the framework of a spatially flat

ΛCDM cosmological model, with $\Omega_m = 0.30$, $\Omega_\Lambda = 0.70$, and $H_0 = 70.0\ \mathrm{km\,s^{-1}\,Mpc^{-1}}$. In this cosmology, one arcsecond corresponds to 8.01 kpc at the typical redshift $z \simeq 1$ of the VACA LoCA clusters. The best-fit estimates and uncertainties of any of the model parameters correspond respectively to the 50$^{\mathrm{th}}$ percentile and 68% credibility interval of the corresponding marginalised posterior probability distributions.

4.1 Data overview

Gonzalez et al. (2019) reports a preliminary, low-scatter mass-richness scaling relation for the MaDCoWS cluster sample based on the infrared richness estimates from observations with the Infrared Array Camera (IRAC; Fazio et al. 2004) on the *Spitzer Space Telescope* and masses derived from the SZ signal measured by the CARMA[1] (see Brodwin et al. 2015, Gonzalez et al. 2015, Decker et al. 2019). In order to improve the calibration of the mass-richness correlation, the VACA LoCA observations have been devised to target a sample of ten MaDCoWS galaxy clusters observable by ACA and representative of the median sample richness.

4.1.1 ACA observations

The ACA observations of the selected MaDCoWS clusters were carried out between May and October 2017 as part of ALMA Cycle 4 operations (project ID: 2016.2.00014.S, PI: M. Brodwin). In order to reach a target continuum sensitivity of around 80 μJy, the integration time on source for each of the pointings amounts to an average of 2.6 hours.

The overall frequency band was tuned to cover the range 89.5 – 105.5 GHz, using four Band 3 spectral windows in continuum mode with centres at approximately 90.5, 92.5, 102.5, and 104.5 GHz. This provided a good trade-off between probing the SZ signal spectrum near its minimum (i.e., maximum amplitude of the negative spectral distortion; see Figure 1.2) and probing the largest scales accessible by ACA Band 3 data. The resulting dynamic range of uv-plane distances in the ACA observations of the MaDCoWS clusters span, on average, between 2.64 and 17.23 kλ, corresponding respectively to angular scales from 1.30 arcmin to 11.97 arcsec (I refer to Table 4.1 for further observational details).

I perform the calibration of all the data in `CASA` (McMullin et al. 2007) package version 4.7.2 using the standard calibration pipelines provided at data delivery. A direct inspection of the reduced data sets did not highlight any significant issue with the calibration. I hence adopt the nominal value of 5% for the fiducial uncertainty on the ACA absolute calibration[2].

All the interferometric images presented in this chapter are generated using the `tclean` task in `CASA` version 5.6.1. To better highlight the SZ features in the maps, I do not correct for the primary beam attenuation. The fields are cut off at the standard 0.2 gain level of the ACA antenna pattern. I note that, as the study is entirely performed on the raw interferometric data, the ACA maps are included only for display purposes. No deconvolution is performed to reduce the effects of sidelobes on the reconstructed dirty maps.

[1] http://www.mmarray.org

[2] https://almascience.nrao.edu/documents-and-tools/cycle4/alma-technical-handbook

Cluster ID	Obs. date	Time (hours)	RMS (mJy)	uv range (kλ)	Resolution (arcsec)	MRS (arcmin)
MOO J0129−1640	2017-08-27	2.78	0.061	1.70 – 17.20	17.8×12.4	2.02
MOO J0345−2913	2017-09-03	3.15	0.055	1.91 – 17.03	18.2×10.6	1.80
MOO J0903+1310	2017-07-27	3.05	0.087	1.75 – 14.69	17.2×11.4	1.96
MOO J0917−0700	2017-05-09	2.08	0.069	2.13 – 16.51	19.4×9.5	1.61
MOO J1139−1706	2017-09-07	2.14	0.081	2.52 – 17.22	19.9×9.6	1.36
MOO J1223+2420	2017-05-08	3.07	0.061	2.09 – 13.67	16.7×13.2	1.64
MOO J1342−1913	2017-08-18	2.46	0.071	1.74 – 17.19	17.9×9.9	1.98
MOO J1414+0227	2017-09-03	3.09	0.066	1.73 – 16.30	17.0×9.6	1.99
MOO J2146−0320	2017-08-03	1.37	0.101	1.87 – 16.41	19.3×10.9	1.84
MOO J2147+1314	2017-08-19	2.61	0.062	1.54 – 14.98	18.5×9.6	2.23

Table 4.1: Summary of the observational properties of the VACA LoCA sample of MaDCoWS galaxy clusters. The reported noise RMS is the average noise level as measured from naturally-weighted dirty images. The corresponding dirty beam is reported in the table as the nominal data resolution. The MRS is instead derived from the minimum projected baseline in the full-bandwidth measurements.

4.2 Analysis technique

As broadly discussed in the previous chapters, spatial filtering due to the incomplete sampling of the Fourier modes of the observed sky may represent a severe challenge in the analysis of radio-interferometric measurements of galaxy clusters. To provide a sense of the net effects of ACA filtering on the SZ signal from a galaxy cluster, in Figure 4.2 I compare the model and filtered SZ profiles for a cluster with a mass of $2.5 \cdot 10^{14}$ $M_\odot$ at a redshift $z = 1.00$.

While the missing flux issue is commonly solved by means of deconvolution techniques (at the expense of introducing correlation in the image-space noise; see Section 1.2 for a discussion), it is possible to include short spacings only by complementing the interferometric data with external information on larger scales, e.g., from single-dish telescopes as for Chapter 2. However, these large-scale observations should have sensitivities comparable to the corresponding interferometric measurements, a condition that is difficult to realise in the case of SZ data.

In order to circumvent any of the challenges introduced by the interferometric filtering, I perform a Bayesian forward-modelling analysis directly on the visibilities of the ACA MaDCoWS sample. This allows for inferring the cluster masses from the raw interferometric data, accounting for the exact sampling function of the visibility plane, as well as providing a strong leverage on possible contamination from unresolved (point-like) sources. Both the modelling methodology and implementation are the same employed in the previous chapters of this thesis.

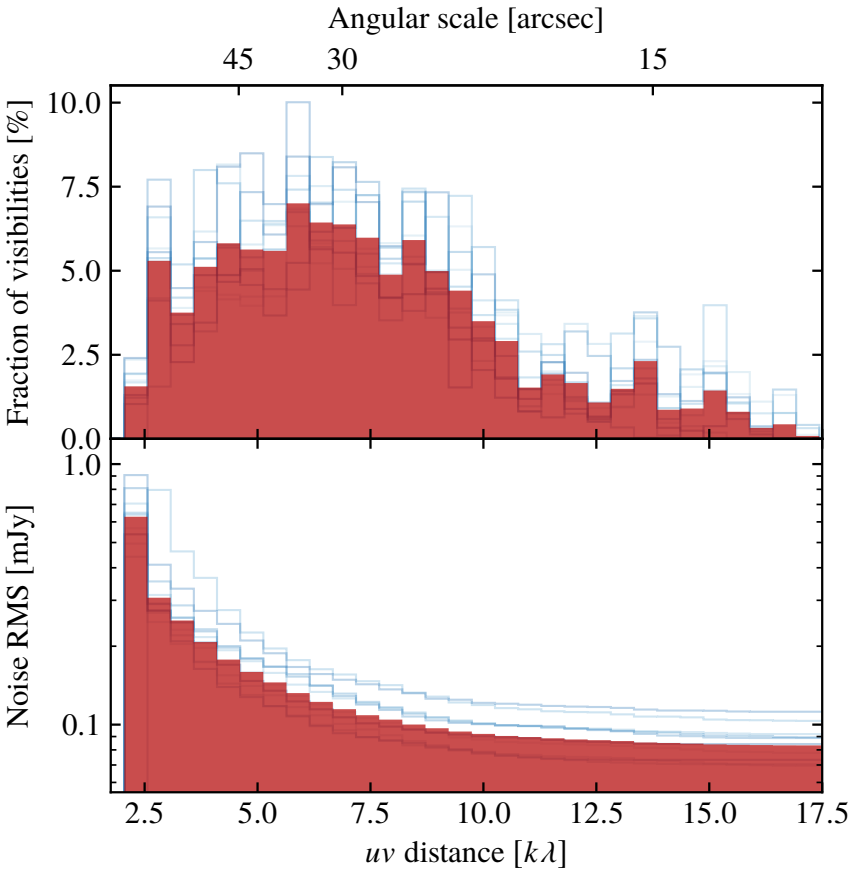

Figure 4.1: Fraction of visibility points for given bin of uv distances (top) and corresponding cumulative noise root-mean-square (bottom). The blue lines correspond to the individual fields, while the red shaded region to their average. The clear flattening of the cumulative noise curve for uv distance larger than around 10 kλ suggests the sensitivity budget is overall dominated by short baselines (i.e. large-scale modes).

4.2.1 Estimating cluster masses

As for the analyses presented in the previous chapters, the pressure distribution of the electrons within the intracluster medium is modelled as

$$P_{\mathrm{e}}(\xi) = P_{500} \times p(\xi), \tag{4.1}$$

where the scaled pressure profile $p(\xi)$ is defined by the gNFW profile,

$$p(\xi) = P_0 \, \xi^{-c} \, [(1 + \xi^a)]^{(c-b)/a} \, . \tag{4.2}$$

As in Chapter 3, P_0 acts a simple normalisation factor. Again, the parameters a, b, and c are respectively the radial slopes at intermediate, large, and small scales with respect to a scale radius r_s, while $\xi = r/r_{\mathrm{s}}$ is the radial distance r from the pressure centroid in units of r_s.

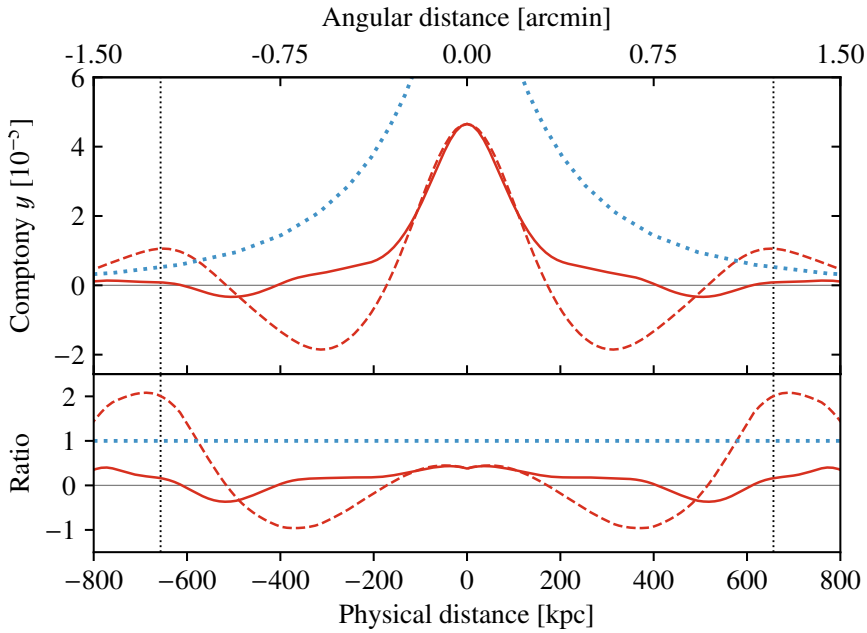

Figure 4.2: Simulated SZ profile for a cluster with mass of $2.5 \cdot 10^{14}$ $M_\odot$ and redshift $z = 1.00$, analogous to the MaDCoWS targets previously reported in Gonzalez et al. (2019). The top panel shows a comparison of the input SZ model (i.e. the true profile; dotted blue line), and the corresponding profiles after application of the interferometric transfer function (i.e. the filtered, observed profiles; red lines). These clearly shows how the fraction of missing flux is significant already well within the r_{500} of the simulated cluster (see Section 4.2.1 for a definition; vertical lines). The two filtered profiles are measured along directions at constant right ascension or declination (respectively dashed and solid lines). Their difference reflects the asymmetry in the uv coverage. The lower panel reports the ratio of the filtered and raw profiles. The line style is the same as the upper panel, corresponding to the ratio of the filtered (observed) profiles to the unfiltered (true) profile. The blue dotted line indicates unity (i.e. no filtering).

Following Arnaud et al. (2010), the scaling parameter P_{500} is defined as

$$P_{500}(M_{500}, z) = 1.65 \cdot 10^{-3}\, E(z)^{8/3} \left[\frac{M_{500}}{3 \cdot 10^{14} M_\odot}\right]^{2/3+a_p(\xi)} \text{keV cm}^{-3} \tag{4.3}$$

where $E(z)$ is the ratio of the Hubble constant at redshift z to its present value H_0, and M_{500} is the mass enclosed within the radius r_{500} at which the average cluster density is 500× the critical density $\rho_c(z)$ of the Universe at the redshift of the cluster. Under the assumption of spherical symmetry, the radius r_{500} can be easily expressed as a function of a given mass M_{500} and redshift z as

$$r_{500}(M_{500}, z) = \left[\frac{3}{4\pi} \frac{M_{500}}{500 \rho_c(z)}\right]^{1/3}. \tag{4.4}$$

This can then be related to the scale radius r_s of the normalised gNFW profile in Eq. (4.2) by adding a concentration parameter c_{500} as $r_s = r_{500}/c_{500}$.

	universal	cool core	disturbed	*Planck*	MD14
P_0	8.40	3.25	3.20	6.41	$3.47^{+1.09}_{-0.67}$
c_{500}	1.18	1.13	1.08	1.81	$2.59^{+0.37}_{-0.38}$
a	1.05	1.22	1.41	1.33	$2.27^{+0.89}_{-0.40}$
b	5.49	5.49	5.49	4.13	$3.48^{+0.60}_{-0.39}$
c	0.31	0.77	0.38	0.31	$0.15^{+0.13}_{-0.15}$
a_0	0.22	0.22	0.22	0.00	0.22

Table 4.2: Best-fit parameters of the gNFW pressure models from Arnaud et al. (2010), Planck Collaboration V (2013), and McDonald et al. (2014, referred to here as MD14).

Finally, the running slope $a_{\rm P}(\xi)$ is introduced to account for any departure from self-similarity in the innermost regions of galaxy clusters,

$$a_{\rm P}(\xi) = a_0/[1 + 8\xi^3] \tag{4.5}$$

In this analysis, the self-similarity deviation parameter a_0, the pressure normalisation P_0, the concentration parameter c_{500}, and the gNFW slopes a, b, and c are kept fixed. In fact, the parameters a_0, P_0, and c_{500} are degenerate with the mass parameter M_{500}, and unconstrained fittings would significantly affect the recovery of the cluster masses. On the other hand, test fittings with free gNFW slopes have shown all the three parameter a, b, and c would remain entirely unconstrained, as well as suffer of strong degeneracies with any of the other gNFW parameters and mass M_{500}. This is a direct consequence of the limited dynamic range of angular scales probed by ACA which, in combination with the modest sensitivity of the VACA LoCA observations, limits the information available for reconstructing pressure profiles for the individual fields

Hence, I set the above gNFW parameters alternatively to the best-fit values reported in Arnaud et al. (2010) for the universal pressure profile, or for the sub-samples of cool-core and morphologically-disturbed clusters. For a comparison, I additionally consider gNFW parameters derived in Planck Collaboration V (2013) from the joint fit of *XMM-Newton* and *Planck*-selected sample of galaxy clusters, as well as the high-redshift *Chandra* gNFW model by McDonald et al. (2014). The different set of parameters adopted in the analysis are summarised in Table 4.2.

At each iteration of the posterior sampling, I then compute the expected thermal SZ signal by integrating the pressure model defined in Eq. (4.1) for a given value of M_{500} and redshift z. The resulting variation in the CMB surface brightness $\delta i_{\rm tSZ}(\boldsymbol{x}, \nu)$ in a direction $\boldsymbol{x}$ on the plane of the sky and at a frequency ν is computed as in Equation 1.1 and 1.2. The integral along the line-of-sight coordinate ℓ is computed from 0 up to the fiducial value of $5r_{500}$ (Arnaud et al. 2010). For simplicity, I neglect any temperature-dependent corrections arising from the fully relativistic treatment of the thermal SZ effect. In fact, the ACA observations cover a frequency band that is not sufficiently broad, nor deep enough, to constrain any relativistic contribution to the SZ spectrum and, hence, for getting direct constraints on the average temperature of the electron populations within the observed clusters (Challinor & Lasenby 1998, Itoh et al. 1998, Sazonov & Sunyaev 1998). Further, the correction to the non-relativistic thermal signal for the

ACA MaDCoWS clusters is expected[3] to be on average less than $\sim 5\%$. Although this will bias the reconstructed masses systematically to lower values, the effect will be at most of the same order as the flux uncertainties discussed in Section 4.1.1, and well within the modelling statistical uncertainties (see Section 4.3 below).

Similarly, the ACA frequency coverage is not wide enough to allow for retrieving any information about the bulk velocities of the observed clusters (or parts of them). Therefore, I assume any contributions from a possible kinematic SZ component (Sunyaev & Zeldovich 1980 and Section 1.1.3) to be sub-dominant with respect to the thermal effect and neglect it in this analysis.

4.2.2 Unresolved sources

Contamination from point-like radio sources may limit and significantly affect the reconstruction of a cluster model from SZ observations (Gobat et al. 2019, Mroczkowski et al. 2019b). In order to assess the level at which the unresolved flux might have contributed to the estimates of the masses of VACA LoCA clusters, I performed blind searches of point-like components over the entire field of views of the ACA observations and simultaneously with the SZ analysis. I assumed the unresolved components to be described by a Dirac-δ model with flat spectrum over the entire ACA band. In fact, the long-baseline data range, most sensitive to the signal from compact sources, is the less-densely parsed region of the visibility plane (see Figure 4.1). This results in high noise on the smaller angular scales, hence limiting the possibility of constraining the spectral properties of the unresolved sources in the observed fields. The point-like model thus simplifies to (Equation A.14)

$$V(\boldsymbol{u}, \nu) = i_{\rm PS} e^{2\pi j \boldsymbol{u}\cdot\boldsymbol{x}_{\rm PS}}, \tag{4.6}$$

given a set of interferometric data with visibility coordinates $\boldsymbol{u}$. The position $\boldsymbol{x}_{\rm PS}$ and the source flux $i_{\rm PS}$ were left free to vary.

Due to the limited information provided by the ACA data about the population of unresolved sources in the VACA LoCA fields, I here consider them as nuisance model components and generally marginalise over them. A future analysis with higher-resolution, multi-frequency observations will be key for their proper characterisation.

4.2.3 Parameter priors

The comparison of cluster positions identified through the MaDCoWS search and the galaxy distribution centroids measured by *Spitzer* are found to deviate by $\sigma_{\rm RA} = 14.3$ arcsec in right ascension and $\sigma_{\rm Dec} = 15$ arcsec in declination (Gonzalez et al. 2019). I thus assume normal priors with standard deviations of $\sigma_{\rm ra}$ and $\sigma_{\rm Dec}$ on the right ascension and declination coordinates of the cluster centroids, respectively.

[3]The average relativistic correction reported in the text is computed employing the formulation by Itoh & Nozawa (2004). The average electron temperature is inferred from the core-excised temperature-redshift-mass scaling relation in Bulbul et al. (2019). To keep a conservative upper limit, I consider an extreme case of a galaxy cluster with the same mass as the most massive object identified in the MaDCoWS survey (Ruppin et al. 2020) at a redshift equal to the largest value in the ACA sample.

The mass parameter M_{500} and the redshift z are heavily degenerate, as they both enter in the determination of the pressure model through the pressure normalisation P_{500} and the scale radius r_{500}. In order to alleviate the degeneracy, I adopt split-normal priors (Wallis 2014) on the redshifts z based on the photometric constraints on the cluster members from *Spitzer* (Gonzalez et al. 2019). When fitting the gNFW profile from McDonald et al. (2014), the gNFW parameters were also assigned split-normal priors, with standard deviations given by the respective parameter uncertainties in Table 4.2.

To account for the ACA flux uncertainties in the recovered masses (Section 4.1.1), I introduce a normalisation hyperparameter as detailed in Section 2.1.5. In particular, I consider a scaling parameter characterised by a normal prior distribution with unitary mean value and standard deviation equal to the inherent calibration uncertainty.

Finally, I assumed wide uninformative priors on all the point-source parameters apart from the position. For the blind search, this was bound to vary uniformly within the region defined by the first null of the ACA primary beam. Data-free runs for each of the analysed data sets (see Section 2.2 for a definition) showed no biases in the parameter inference related to choice in the prior distributions.

4.3 Results and discussion

A summary of the masses of the VACA LoCA pilot sample is presented in Table 4.3. The results presented in previous MaDCoWS papers (Brodwin et al. 2015, Decker et al. 2019, Gonzalez et al. 2019) were derived adopting the universal profile by Arnaud et al. (2010) for describing the electron pressure distribution. For consistency, I here report only the masses estimated under the same assumption. A discussion about the impact of model choice on the inferred masses is however presented in Section 4.3.4.

I quantify the detection significance of the SZ signal in the VACA LoCA observations by comparing the log-evidences of the full modelling runs $\mathcal{Z}_1$ with the ones considering only the point-source model component $\mathcal{Z}_0$ by means of Jeffreys' scale[4] (Jeffreys 1961). To get a more immediate handle on the significance of each detection, I report in Table 4.3 the number of effective standard deviations $\sigma_{\rm eff}$ between the model with and without an SZ component. This can be computed as $\sigma_{\rm eff} \simeq \sqrt{2\Delta \log \mathcal{Z}}$ given a log-Bayes factor $\Delta \log \mathcal{Z} = \log (\mathcal{Z}_1/\mathcal{Z}_0)$ (Trotta 2008). This differs from the approach taken in the CARMA SZ follow-up papers (Brodwin et al. 2015, Gonzalez et al. 2015, Decker et al. 2019) in that it is more statistically robust, as it properly accounts for the change between different models in the number of parameters and respective priors. I note that $\sigma_{\rm eff}$ is to be interpreted in a merely heuristic manner, as I am not accounting for the different degrees of freedom or prior volumes between the models. According to Jeffreys' criterion, introduced above, a value of $\sigma_{\rm eff} \gtrsim 3$ is indicative of a robust detection.

Overall, I significantly detect the SZ effect toward seven out of the ten clusters of the VACA LoCA sample, while the presence of SZ signal is only weakly favoured for MOO J1223+2420 and MOO J2147+1314. For the single case of MOO J0903+1310, the analysis favours the

[4]As a reference, I consider a cluster to be significantly, weakly, or not detected if the corresponding model has a Bayes factor $\mathcal{Z}_1/\mathcal{Z}_0$ respectively larger than 100, between 1 and 100, or less than 1.

Cluster ID	$z_{\rm phot}$ –	λ –	r_{500} (Mpc)	θ_{500} (arcmin)	$Y_{\rm sph}(<r_{500})$ 10^{-5} Mpc^2	$Y_{\rm cyl}(<r_{500})$ 10^{-5} Mpc^2	M_{500} ($10^{14}\,M_\odot$)	$\sigma_{\rm eff}$ –
Significant detection								
MOO J0129−1640	$1.05^{+0.04}_{-0.05}$	49 ± 7	$0.67^{+0.09}_{-0.08}$	$1.38^{+0.03}_{-0.21}$	$2.13^{+0.01}_{-0.66}$	$2.34^{+0.01}_{-0.72}$	$2.57^{+0.30}_{-0.30}$	7.77
MOO J0345−2913	$1.08^{+0.03}_{-0.04}$	53 ± 7	$0.57^{+0.02}_{-0.03}$	$1.17^{+0.05}_{-0.07}$	$1.04^{+0.25}_{-0.26}$	$1.15^{+0.27}_{-0.29}$	$1.78^{+0.20}_{-0.29}$	5.32
MOO J0917−0700[a]	$1.10^{+0.05}_{-0.05}$	58 ± 7	$0.55^{+0.04}_{-0.05}$	$1.11^{+0.08}_{-0.08}$	$0.97^{+0.40}_{-0.33}$	$1.07^{+0.44}_{-0.37}$	$1.66^{+0.31}_{-0.38}$	4.26
			$0.58^{+0.04}_{-0.04}$	$1.19^{+0.08}_{-0.09}$	$1.48^{+0.54}_{-0.49}$	$1.63^{+0.59}_{-0.53}$	$2.13^{+0.40}_{-0.49}$	
MOO J1139−1706	$1.31^{+0.03}_{-0.05}$	53 ± 7	$0.56^{+0.02}_{-0.03}$	$1.10^{+0.05}_{-0.05}$	$1.51^{+0.38}_{-0.25}$	$1.66^{+0.41}_{-0.27}$	$2.24^{+0.36}_{-0.52}$	3.81
MOO J1342−1913	$1.08^{+0.04}_{-0.05}$	41 ± 6	$0.59^{+0.03}_{-0.03}$	$1.20^{+0.08}_{-0.07}$	$1.22^{+0.39}_{-0.29}$	$1.34^{+0.42}_{-0.32}$	$1.95^{+0.31}_{-0.31}$	4.53
MOO J1414+0227	$1.02^{+0.07}_{-0.06}$	41 ± 7	$0.67^{+0.04}_{-0.04}$	$1.40^{+0.09}_{-0.08}$	$2.29^{+0.50}_{-0.43}$	$2.52^{+0.55}_{-0.48}$	$2.75^{+0.32}_{-0.32}$	6.99
MOO J2146−0320[a]	$1.16^{+0.05}_{-0.05}$	50 ± 7	$0.57^{+0.05}_{-0.05}$	$0.94^{+0.11}_{-0.05}$	$1.19^{+0.45}_{-0.40}$	$1.32^{+0.49}_{-0.44}$	$1.86^{+0.34}_{-0.52}$	5.35
			$0.55^{+0.05}_{-0.05}$	$1.09^{+0.06}_{-0.05}$	$1.43^{+0.64}_{-0.56}$	$1.58^{+0.71}_{-0.62}$	$2.04^{+0.42}_{-0.56}$	
Weak detection								
MOO J1223+2420[b]	$1.09^{+0.04}_{-0.04}$	51 ± 7	$0.49^{+0.04}_{-0.07}$	$0.99^{+0.09}_{-0.14}$	$0.49^{+0.18}_{-0.29}$	$0.54^{+0.19}_{-0.32}$	$1.17^{+0.27}_{-0.38}$	2.40
MOO J2147+1314	$1.01^{+0.06}_{-0.07}$	38 ± 6	$0.59^{+0.05}_{-0.04}$	$1.22^{+0.08}_{-0.12}$	$1.01^{+0.40}_{-0.43}$	$1.11^{+0.44}_{-0.48}$	$1.82^{+0.34}_{-0.42}$	1.26
Non detection								
MOO J0903+1310	$1.26^{+0.05}_{-0.08}$	29 ± 5	$0.30^{+0.05}$	$0.59^{+0.10}$	$0.04^{+0.06}$	$0.05^{+0.07}$	$0.30^{+0.18}$	–

Table 4.3: Inferred quantities for the VACA LoCA sample clusters under the assumption of a universal pressure profile (Arnaud et al. 2010). See Section 4.3 for more details about the effective significance estimate $\sigma_{\rm eff}$. The photometric redshift $z_{\rm phot}$ and infrared richness λ are taken from Gonzalez et al. (2019).

[(a)] The two mass values provided for MOO J0917−0700 and MOO J2146−0320 correspond to the masses of each of the individual SZ components detected in the analysis.

[(b)] The SZ signal from MOO J1223+2420 has significant contamination from an FR II radio galaxy at the centre of the cluster (see Section 4.3.3).

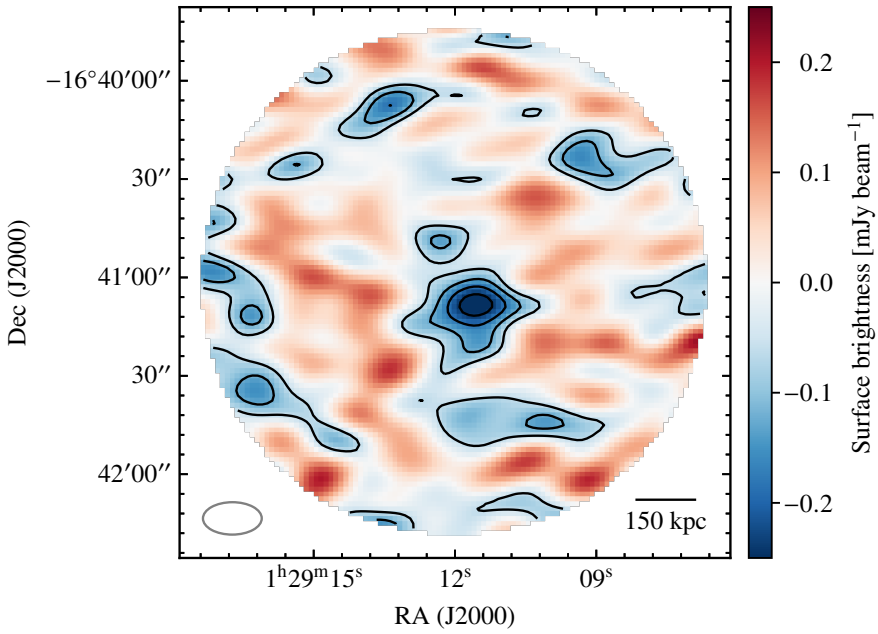

Figure 4.3: Dirty image of MOO J0129−1640 generated from point source-subtracted visibilities. The point-source components are identified as the peaks in the joint posterior probability distribution point-source position parameters. The contours correspond to the 1σ, 2σ, 3σ, and 4σ significance levels of the SZ signal, with $\sigma = 0.061$ mJybeam^{-1}. Although the integrated SZ decrement is detected at $\sigma_{\rm eff} = 7.77$ (Table 4.3), the peak SZ amplitude has a significance only slightly larger than 4σ when measured in image space.

model without the SZ component, thus resulting in a non-detection. Reported in Table 4.3 is the estimated upper limit for the cluster mass.

As for the analyses presented in Brodwin et al. (2015), Gonzalez et al. (2015), and Decker et al. (2019) of CARMA data, the fitting of ACA data is performed entirely in *uv*-space. Along with the advantages discussed in Section 4.2, this provides an approach to cluster detection in interferometric SZ data that avoids the drawbacks of image-space analysis, in particular, the biased reconstructions produced by the `CLEAN` algorithm (see Section 1.2.2 for a discussion). For a comparison, I show in Figure 4.3 the dirty image of the most significant detection in the sample, MOO J0129−1640. The peak of the SZ decrement has an amplitude of −0.24 mJy beam^{-1}, corresponding to a statistical significance of 4.06σ, which is lower than the cluster detection $\sigma_{\rm eff} = 7.77$ (Table 4.3). Of course, this is not surprising, as $\sigma_{\rm eff}$ is measuring the significance of the total SZ signal. However, in addition to the fact that the SZ signal is resolved, the reason for this discrepancy also resides in the fact that the interferometric images are affected by heavily correlated noise. As a consequence, the resulting fluctuations may attenuate the measured signal and limit the confidence of its detection. On the other hand, side lobes further contaminate interferometric images. As already discussed in Section 1.2.2, this is generally solved by applying `CLEAN`-like deconvolution techniques to the data (Högbom 1974, Thompson et al. 1986). However, these are specifically devised for reducing the effects of the incomplete sampling

of the visibility plane on the overall quality of the reconstructed image (see Section 1.2.2), and would not provide any serious improvement in the significance of the observed SZ signal. In fact, it is worth noting any deconvolved image would still provide a heavily high-pass filtered view of the very core of a galaxy cluster, as ACA is not measuring the SZ signal on scales larger than the maximum recovered scale (Table 4.1).

Another important remark is that the dirty map shown in Figure 4.3 is generated only after subtraction from the visibility data of the most significant point-like sources detected by the modelling algorithm, allowing for a cleaner identification of the SZ signal in the cluster image. In fact, the presence of very bright compact sources may completely hide any SZ effect component, as either their signal would be super-imposed to the one from the galaxy cluster or the side lobes would be blended with the SZ feature.

4.3.1 Mass-richness relation

Figure 4.4 shows a comparison of the mass-richness scaling for the VACA LoCA sample and the CARMA measurements previously reported by Gonzalez et al. (2019). Although there is good consistency between the VACA LoCA estimates and the MaDCoWS mass-richness scaling, the VACA LoCA mass-richness distribution is systematically below the expected correlation. I quantify the average scaling by fitting the VACA LoCA data points with a linear function with the slope constrained to that of the mass-richness scaling in Gonzalez et al. (2019) but free normalization parameter (which translates to an offset in the logarithmic relation). I find that the VACA LoCA cluster masses are down-scaled by a factor $0.56^{+0.13}_{-0.05}$ with respect to the CARMA-derived mass-richness scaling when considering all the VACA LoCA clusters. The resulting scatter of the ACA masses with respect to the reconstructed relation is $\sigma^{\rm ACA}_{\log M|\lambda} = 0.25^{+0.06}_{-0.02}$, broader than the scatter observed in the CARMA measurements. However, if I exclude the non-detection from the analysis, the scatter decreases to a value comparable with the CARMA measurement, $\sigma^{\rm ACA}_{\log M|\lambda} = 0.18^{+0.02}_{-0.01}$, while the relative normalization remains statistically consistent with the previous estimate ($0.58^{+0.15}_{-0.05}$). This suggests that the non-detection is a major actor in the increase of the measured scatter, possibly representing an outlier from the richness-mass relation. The observed deviation from the nominal mass-richness relation may imply an overall systematic mis-estimation of the cluster masses. On the other hand, a joint fit of both the CARMA and VACA LoCA samples provides an overall scatter of $\sigma^{\rm JOINT}_{\log M|\lambda} = 0.17^{+0.05}_{-0.02}$. It may thus be possible that a scatter intrinsic to the mass-richness distribution or arising due to the limited size of studied sample may dominate the calibration of the mass-richness relation. Further observations of the SZ footprint of galaxy clusters spanning a broader richness range will be key in improving the current constraints on the MaDCoWS mass-richness scaling relation.

The fact that ACA can only provide a high-pass filtered view of the SZ signal (coupled with possible deviations from the fiducial average pressure profile; see discussion below) may be among the main causes of the slight discrepancy of the VACA LoCA masses with respect to the scaling relation obtained using SZ measurements from CARMA. In fact, CARMA probed the SZ signal out to scales larger the r_{500} values of the observed clusters, hence accessing spatial information crucial to mass determination within a cosmologically relevant overdensity. In contrast, though the ACA observations have improved sensitivity on sub-arcminutes scales, the

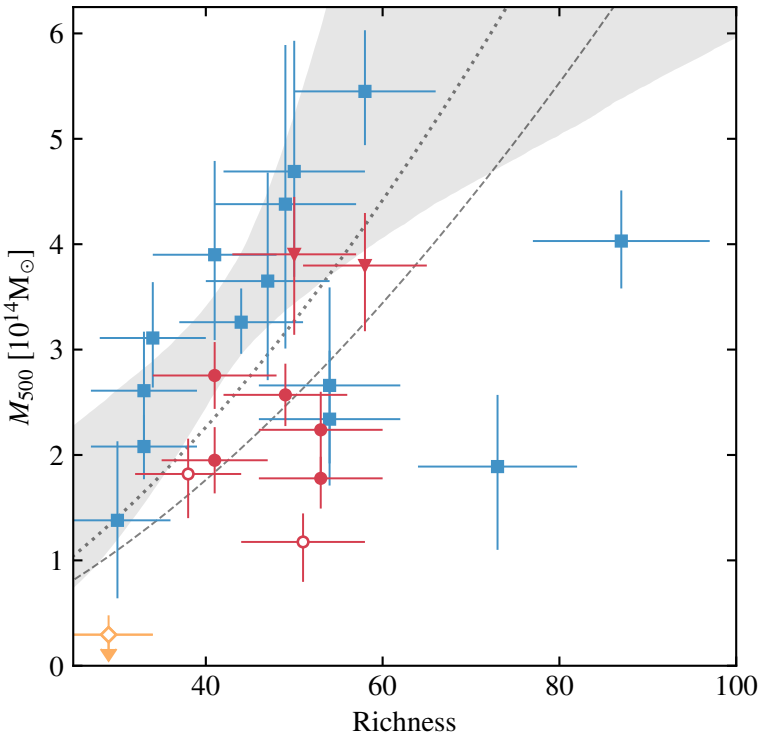

Figure 4.4: Mass vs. richness relation for all the MaDCoWS clusters with SZ-based mass estimates. The blue squares correspond the CARMA MaDCoWS cluster sample from Gonzalez et al. (2019). In solid and open red are the clusters from this chapter with significant or weak detection, respectively, while the upper limit for non-detected MOO J0903+1310 is denoted with a yellow open diamond. I use circles and triangles for the clusters with single or double SZ features, respectively. In the latter case, the plot reports the sum of the masses of the individual SZ components. The shaded region is the 68% confidence interval for the mass-scaling relation reported in Gonzalez et al. (2019). The VACA LoCA distribution is observed to sit below the mass-richness relation previously reported, highlighting potential systematics in the mass reconstruction from either or both the CARMA and ACA observations. The dashed and dotted lines correspond to the mass-richness scaling derived in Section 4.3.1 respectively from the VACA LoCA points only (excluding the non-detection) and from the joint modelling of the VACA LoCA and CARMA measurements.

reconstructed masses are derived by extrapolating the assumed pressure profile from the very core regions of the clusters. In order to assess whether filtering effects play a major role in biasing the cluster masses low, I re-run the modelling by forcing the model mass M_{500} to be equal to the value expected from the mass-richness relation by Gonzalez et al. (2019), and fit for the normalisation P_0 by assuming a wide uninformative prior. Once again, to be consistent with previous studies, I only consider the universal profile case. If the mass-richness relation provides an unbiased estimate of the cluster masses for the measured richnesses, I should then expect the respective SZ model to well describe the ACA *uv* data, and the inferred estimates of P_0 to be consistent with the nominal value in Table 4.2. To facilitate interpretation, I here limit the analysis to the clusters

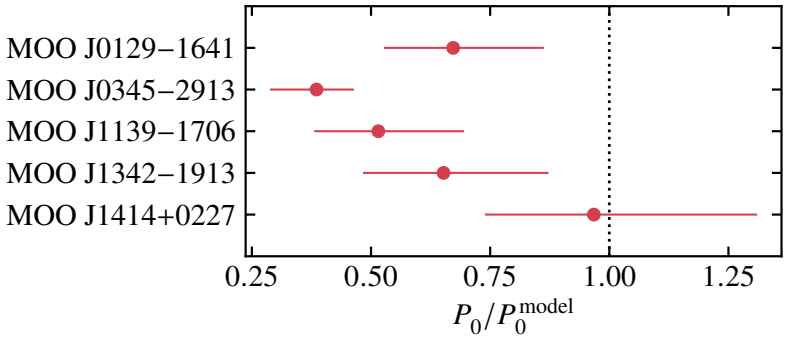

Figure 4.5: Inferred pressure normalisation P_0 when assuming a cluster mass derived using the mass-richness relation from Gonzalez et al. (2019) and a universal pressure profile (Arnaud et al. 2010). The ratios reported here are normalised by the nominal value for P_0 given in Table 4.2. As discussed in Section 4.3.1, the observed scatter indicates a true discrepancy, which could be due to deviations from the Gonzalez et al. (2019) mass-richness scaling, or to deviations from the Arnaud et al. (2010) ensemble-average pressure profile. If ACA filtering were driving the mass reconstruction, I would expect a uniformly low value for the ratio, which is not observed. I note that the error bars for each of the point incorporates both statistical uncertainties and scatter intrinsic to MaDCoWS mass-richness scaling relation.

with a single SZ feature with a strong significance. As shown in Figure 4.5, the results are in qualitative agreement with the overall low-mass trend observed in the mass-richness distribution of the VACA LoCA sample cluster. Nevertheless, it is not possible to highlight any evident systematic effect common to all the data points. I thus conclude that the interferometric filtering is unlikely to play a major role in biasing the mass reconstruction to lower masses.

This of course presumes that the universal pressure model by Arnaud et al. (2010) can successfully describe the electron pressure distribution of such systems. However, departures from self-similarity due to, e.g., an actual evolution of the average pressure profile with the cluster redshift (McDonald et al. 2014) or the disturbed state of any of the studied clusters may significantly affect the mass reconstruction (see Ruppin et al. 2019a, for a cosmological application).

4.3.2 Multiple SZ features

The marginalised posterior distribution for the centroids of the galaxy clusters MOO J0917−0700 and MOO J2146−0320 manifest a clear bimodal behaviour (respectively top and bottom panels of Figure 4.6). I checked that they are neither dependent on the assumed prior on the position of the cluster centroid nor on the inclusion of point-like model components.

It may be possible that the individual posterior modes are actually related to distinct SZ components. These may arise, for example, due to the presence of a cluster pair in an early/mid merging phase (the situation is similar, both in terms of cluster masses and separation, to the merging system 1E 2216.0-0401/1E 2215.7-0404; Akamatsu et al. 2016). In such cases, however,

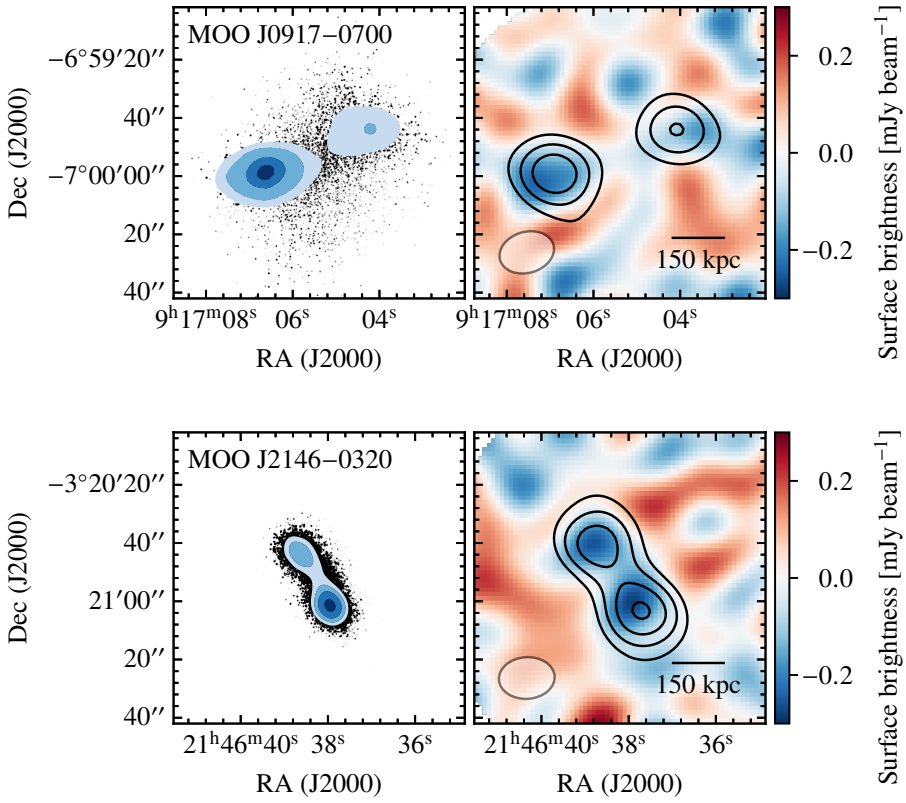

Figure 4.6: Marginalised posterior for the cluster centroids and dirty images (left and right panels, respectively) of the two VACA LoCA clusters characterised by multiple SZ features, MOO J0917−0700 and MOO J2146−0320 (top and bottom panels). The posterior contours correspond, from the inner to the outermost, to 38%, 68%, 87%, and 95% credibility levels. Contours on the right panels show the 1σ, 1.5σ, and 2σ statistical significance levels of the filtered model with respect to the map noise RMS. To better highlight the SZ effect, I subtract from the visibility data the most significant point-like sources as in Figure 4.3, and apply a 10 kλ taper to the data.

the electron pressure distribution will deviate significantly from the average gNFW models adopted in this analysis (Wik et al. 2008, Sembolini et al. 2014, Yu et al. 2015, Ruppin et al. 2019b). In particular, I expect the resulting pressure distribution to be shallower than for the case of a relaxed cluster, hence resulting in an SZ signal more affected by the interferometric short-spacing filtering (see discussion in Section 4.2). Similarly, non-thermal effects may play a central role in providing pressure support to the system (e.g., Battaglia et al. 2012, Shi et al. 2015, Biffi et al. 2016, Ansarifard et al. 2020). As a consequence, I might expect the reconstructed masses to be greatly biased toward values lower than the true ones.

On the other hand, the elongation observed in the marginalised posterior probability for the cluster centroid may be a consequence of the combined effect of an elliptical geometry of the core region of the intracluster medium and residual contributions from unresolved sources (see

discussion in Section 4.3.3 below). In any case, the non-regular electron pressure distribution would indicate tha the clusters may be highly disturbed, again inducing a potential bias in the reconstructed masses.

Unfortunately, the low spatial resolution of the available ACA data does not allow for a proper characterisation of the dynamical state of the two systems.

4.3.3 Unresolved sources

As already briefly mentioned in the previous section, a possible systematic effect that may prevent the proper estimation of the cluster masses from the modelling of ACA data is any residual contamination from emissions that have not been accounted for. Along with radio synchrotron sources, I expect dusty galaxies to contribute to the overall confusion noise (see discussion in Section 2.1.1). However, although I have been able to locate and constrain a number of unresolved components, the lack of high-resolution data (from, e.g., the main 12-meter array) may in fact have limited the identification to the brightest end of the source population contaminating the SZ signal.

On the other hand, the poor resolution and sensitivity do not allow for separating with reasonable confidence the SZ effect from any possible diffuse radio components. Indeed, studies by Moravec et al. (2019, 2020) show that a large fraction of the sources belonging to the population of radio-loud AGNs within the MaDCoWS clusters exhibit extended morphologies. In this regard, external data may be key in complementing information about radio contaminants. Unfortunately, the available radio surveys offer only partial coverage of the VACA LoCA sample.

In particular, I first checked the NRAO VLA Sky Survey (NVSS; Condon et al. 1998) for possible radio components. The inspection of the NVSS images of the VACA LocA fields does not however highlight any significant radio sources, either point-like nor diffuse.

I further inspect the VLA Faint Images of the Radio Sky at Twenty-Centimeters (FIRST; Becker et al. 1995) survey, which provides coverage for only five of the VACA LoCA pilot sample. One low-significance source is found in each of the MOO J0917−0700 and MOO J1414+0227 fields, both coinciding with bright point-like sources identified by the blind search over the ACA data (Section 4.2.2). On the other hand, the FIRST image of MOO J1223+2420 field is the only one to show a clear radio source. This exhibits a double-lobed feature, identified by van Velzen et al. (2015) as belonging to the radio jets from a central FR II radio galaxy. This corresponds to a strong radio source detected near the centre of MOO J1223+2420 ACA field, which may be the cause of the inferred mass well below the value predicted from MaDCoWS mass-richness scaling relation. In fact, although I model any possible contribution from unresolved radio emission from the central regions of the cluster, any residual contributions (e.g., from extended structures) from may still limit the ability to retrieve an accurate estimate of the cluster mass. Unfortunately, the resolution of the ACA observation of MOO J1223+2420 does not allow for discriminating if the model describes the signal from the central galaxy, the radio lobes, or a blend of these two forms of emission (see Figure 4.7).

More recently, the Very Large Array Sky Survey (VLASS; Lacy et al. 2020) completed its first epoch of observations covering the entire sky north of $\delta = -40$ in S-Band (2-4 GHz), which offers the advantage of sharing the same sky coverage as the full MaDCoWS sample but at much higher resolution than NVSS. The first epoch maps reach a depth of ≈ 120 μJy RMS on average.

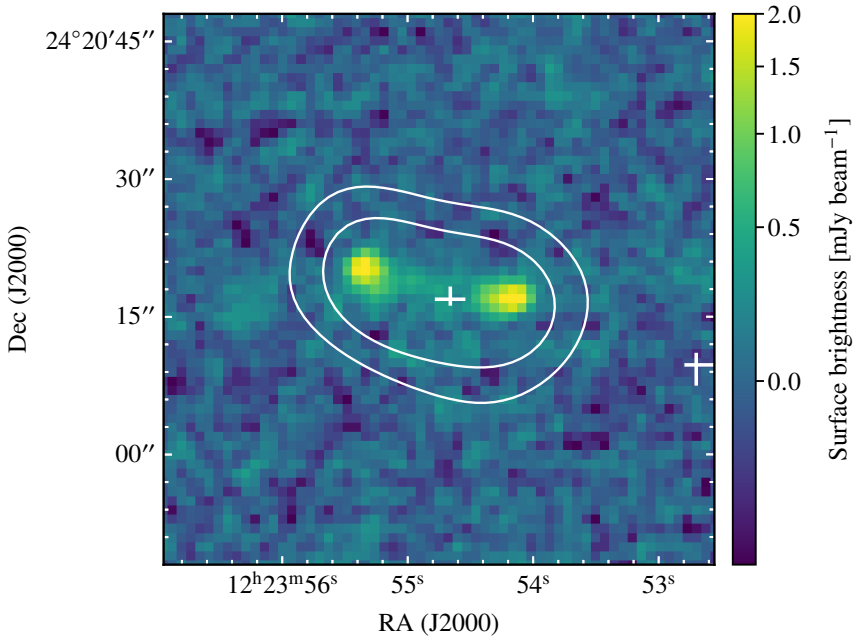

Figure 4.7: VLASS map of the radio structure in MOO J1223+2420. Overplotted are the contours from the same image smoothed to ACA resolution (the levels correspond to the arbitrary values of 0.10 and 0.05 mJy beam^{-1}). The white crosses denote the position of the most significant point sources and respective uncertainties from the 68% credibility interval around each posterior peak. Regardless of the accuracy in the determination of the position of any point-like sources, the low resolution of ACA does not allow for resolving the possible different contributions from the jets and the central galaxy.

Surprisingly, the only sources I have been able to confirm at $> 3\sigma$ significance are those also seen in the FIRST data on MOO J1414+0227 and MOO J1223+2420.

4.3.4 Dependence on the assumed pressure model

As already mentioned in Section 4.2.1, I further test the mass reconstruction against different versions of the gNFW pressure profiles. In Figure 4.8, I provide a direct comparison of the masses and respective effective significance levels for the VACA LoCA clusters with strong detections. The full list with the estimates of the cluster masses for all the profiles considered in Table 4.2 can be found in Table 4.4.

Not unexpectedly, the specific value for the cluster mass is highly dependent on the specific profile assumed to describe the pressure distribution. As shown in the *uv* radial profile of Figure 4.9, most of the SZ flux is not probed by ACA, making it sensitive only to the pressure distribution within the inner region of galaxy clusters. This can also be inferred by comparing the values for the MRS in each observation to $2 \times \theta_{500}$ using Tables 4.1 and 4.3, respectively. This effect couples with the primary beam attenuation of the edges of the ACA fields, which drives the characteristic radius of the gNFW profile to be of the same of order of the antenna pattern half-

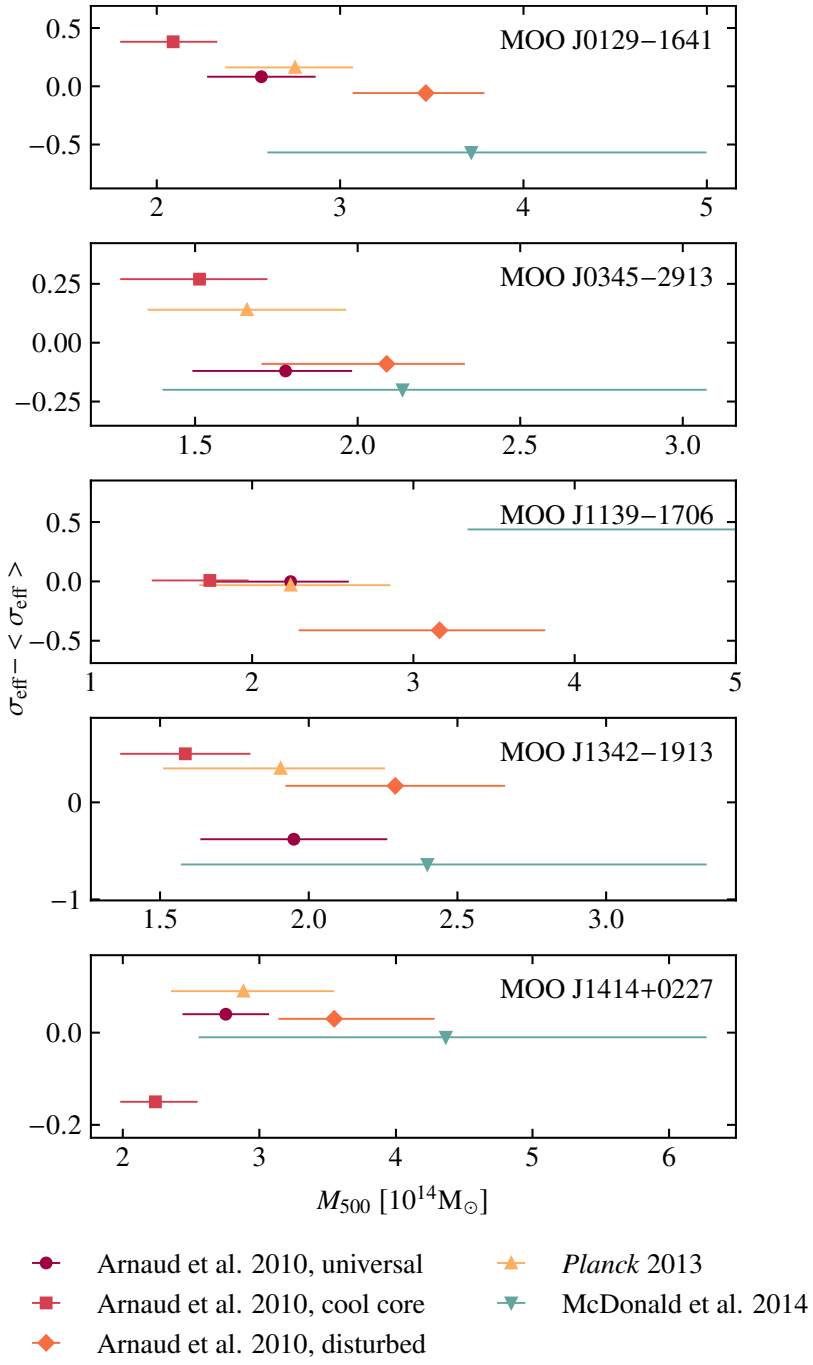

Figure 4.8: Deviations from average significance levels for the best-detected galaxy clusters of the VACA LoCA pilot sample. The points correspond to the mass estimates obtained by assuming different versions of the gNFW pressure profile. The variations in $\sigma_{\rm eff}$ are always less than 3 (see Section 4.3), which, according to Jeffreys' model selection criterion, implies that no pressure model is strongly favoured over the others for any of the VACA LoCA clusters. I note that the large uncertainties on the masses derived assuming the profile by McDonald et al. (2014) are due to the large uncertainties on the respective best-fit gNFW parameters.

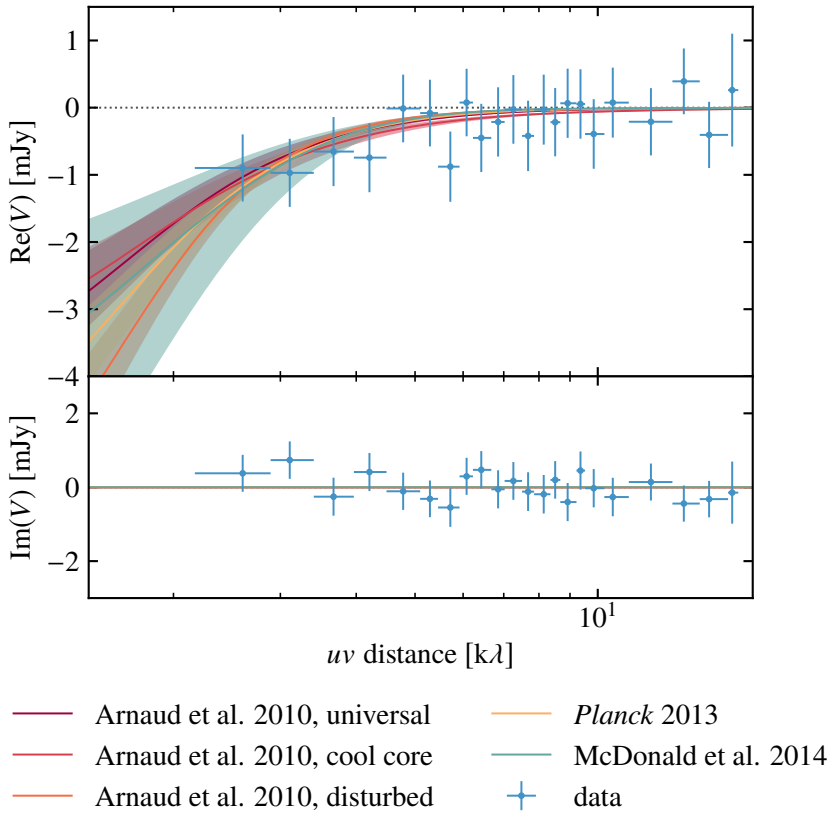

Figure 4.9: Comparison of the real (top) and imaginary (bottom) parts of ACA point source-subtracted visibilities $V = V(u, v)$ for MOO J0129−1640, the most significant detection, and the uv radial profiles for the different flavours of gNFW (Table 4.2). The data are binned so that each bin contains the same number of visibilities (here set to 2500 for plotting purposes). Before averaging, I shifted the phase centre to the position of the cluster centroid to minimise the ringing effect due to non-zero phases. As a result, the imaginary part of the visibilities are overall consistent with zero. Any significant deviations would be symptomatic of, e.g., residual off-center point-like sources, or asymmetries in the cluster SZ signal that are unaccounted for in the analysis.

width-half-maximum, and thus affecting the mass reconstruction. As a result, the model based on the gNFW parametrization from McDonald et al. (2014) and for the morphologically-disturbed sample in Arnaud et al. (2010) present masses systematically larger than the other profiles, as a direct consequence of their flatter radial trend at small radii. Conversely, the strongly-peaked cool-core profile by Arnaud et al. (2010) allows for easily fitting low-mass (and, then, very compact) cluster model to the observed SZ signal. Nevertheless, as I have not been able to infer any of the parameters defining the gNFW pressure profile in Eq. (4.2), the small scatter in the effective significance for each of the different pressure models does not allow for selecting or ruling out any of the mass estimates.

The impossibility of discriminating between different gNFW scenarios is an immediate con-

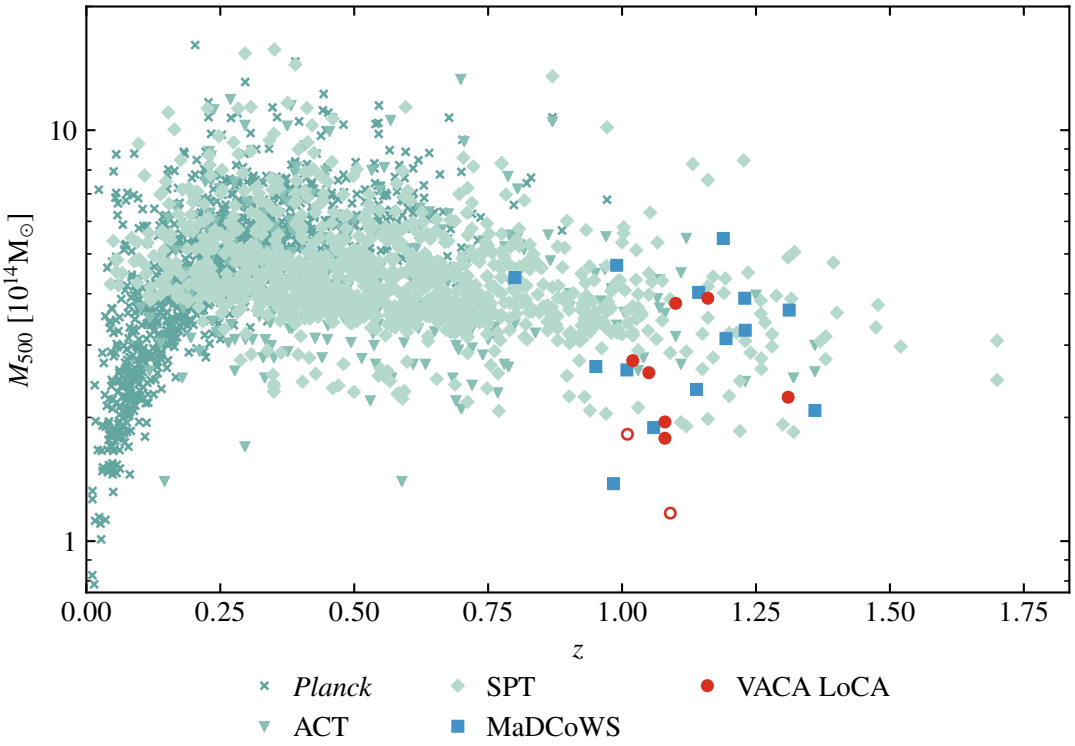

Figure 4.10: Mass vs. redshift distribution of galaxy clusters in the VACA LoCA pilot sample (red circles). As for Figure 4.4, the solid and open points denote respectively the significant and weak detections. For comparison, I include the mass estimates of previously reported MaDCoWS clusters (blue squares; Gonzalez et al. 2019), as well as the samples from *Planck* (mint crosses; Planck Collaboration XXVII 2016), ACT (mint triangles; Marriage et al. 2011, Hasselfield et al. 2013, Hilton et al. 2018), and SPT (mint diamonds; Bocquet et al. 2019, Huang et al. 2020, Bleem et al. 2020) SZ surveys. All the MaDCoWS clusters with SZ data are found to be comparable in mass with the clusters detected by the aforementioned surveys over the same range of redshifts.

sequence of the limited sensitivity of the ACA observations I am analysing, along with the lack of information on large angular scales. Figure 4.9 shows the *uv* radial plot for the different gNFW best-fit models for the most significantly detected cluster of the VACA LoCA sample, MOO J0129−1640. Although they all succeed in describing the long baseline data, they also present a non-negligible scatter over angular scales larger than the maximum recovered scale in the observation. As discussed in Chaper 2 and Perrott et al. (2019), the joint analysis of interferometric measurements and lower-resolution, single-dish observations provides a straightforward solution for improving the reconstruction of models of the SZ signal from galaxy clusters. CMB experiments designed to detect clusters at arcminute resolution, such as the Atacama Cosmology Telescope (ACT; see, e.g., Hilton et al. 2018) or the South Pole Telescope (SPT; see, e.g., Bleem et al. 2015, 2020) could fulfil the needs of complementary large-scale data, and the VACA LoCA clusters are comparable in mass to some of the high-redshift systems detected by those surveys (see Figure 4.10). However, the publicly available data do not cover the portion of the sky

comprising the VACA LoCA fields.

Additionally, Gonzalez et al. (2019) compares the *Planck* mass-redshift relation to the masses inferred for the entire MaDCoWS sample, and finds that they predominantly lie below the mass selection function of *Planck*. For the VACA LoCA sample of MaDCoWS clusters, I find that no useful constraint on the integrated Compton parameter Y can be obtained from *Planck* maps, due to beam dilution and limited sensitivity. In all but the most extreme case, the integrated SZ signal for each clusters would fall within a single $10'$ resolution element of *Planck*. Extrapolating the fits to the VACA LoCA sample, each member should have an average Compton Y value $\langle Y \rangle \lesssim 1.6 \times 10^{-6}$ over an area of 100 square arcminutes, while the RMS noise level in the *Planck* maps is $\approx 1.7 \times 10^{-6}$ on average (Planck Collaboration XXII 2016). This indicates that the most massive clusters in VACA LoCA may be on the order of 1σ significance in the *Planck* maps, while the rest are well below that, and even a stacked measurement using the 10 members of the pilot sample would be marginal.

It is worth noting that the small range of inferred $\sigma_{\rm eff}$ implies that ACA is able to provide robust detections of the SZ signal from the VACA LoCA sample clusters independent of assumptions about the underlying pressure electron distribution.

4.4 Summary

In this chapter, I analyse a pilot sample of ACA observations of ten high-redshift galaxy clusters representative of the typical richness of the MaDCoWS catalogue. This was mainly aimed at directly testing the capability of the ACA in Band 3 for measurements of the SZ signal from high-redshift systems. In summary, the main findings are:

- The ACA can provide robust and relatively straightforward validation of galaxy cluster identifications through the detection of the SZ signal from the intracluster gas. I note that the on-source integration times are typically $\lesssim 3$ hours per target. Most importantly, the detection significance is not affected by the specific choice of pressure distribution model.

- The limited sensitivity and angular dynamic range probed by the observations limit the accuracy of the mass estimates. The mass estimates within r_{500} are strongly dependent on the specific choice of pressure model, as the maximum recoverable scale in the observations is smaller than the typical radius within which one would like to probe the integrated SZ signal, θ_{500} (see Tables 4.1 and 4.3, respectively).

- Related to the point above, a thorough characterisation of the cluster dynamical state cannot be achieved, as the ACA angular resolution and limited sensitivity do not constrain small-scale features in the intracluster medium within the observed galaxy clusters. However, the analysis does reveal two potentially exciting merging cluster candidates that merit more detailed follow-up.

- The *uv*-space analysis of ACA data is crucial for separating the SZ signal from unresolved sources of contamination. However, the reconstruction of a proper and exhaustive model is limited by the aforementioned sensitivity, resolution, and maximum recoverable scale.

Data at higher angular resolution than ACA, e.g., from the ALMA 12-meter array, would provide a dramatic improvement in the identification and characterisation of point-like sources populating the cluster fields. Further, multi-frequency coverage of the cluster fields would provide fundamental insight, as well as better constraints, on the spectral properties of any contaminant source, and thus better disentangle its signal from the underlying SZ effect.

On the other hand, as discussed in Section 4.3.4, the possibility of complementing interferometric observations with single-dish measurements of the same targets will be key in gaining a better description of the electron pressure distribution out to large scales and, hence, a more accurate reconstruction of the cluster masses.

This work made use of the following ALMA data: ADS/JAO.ALMA#2016.2.00014.S. ALMA is a partnership of ESO (representing its member states), NSF (USA) and NINS (Japan), together with NRC (Canada), MOST and ASIAA (Taiwan), and KASI (Republic of Korea), in cooperation with the Republic of Chile. The Joint ALMA Observatory is operated by ESO, AUI/NRAO and NAOJ.

4.5 Supplementary material

4.5.1 Mass estimates

Table 4.4 reports the inferred cluster masses when employing the different gNFW models proposed in Arnaud et al. (2010), Planck Collaboration V (2013), and McDonald et al. (2014). A summary of the profile parameters is provided in Table 4.2.

4.5.2 *uv* plots and dirty images

I here provide the *uv* radial plots of the data and respective gNFW models for all the VACA LoCA clusters (Figure 4.11). As discussed in Section 4.3, all the model profiles show a fairly good agreement with data over the range of probed angular scales, while being affected by a large scatter at short baselines due to the lack of large-scale information. MOO J0345−2913 and MOO J0917−0700 clearly manifest positive modes at small *uv*-scales, while the data points for MOO J2146−0320 are positively offset with respect to the models. These may arise due to off-centre SZ components unaccounted for by the model, or due to extended (positive) emission. However, in the case of MOO J0345−2913, the discrepancy is on the level of 1σ. On the other hand, the SZ signal from both MOO J0917−0700 and MOO J2146−0320 show a complex structure (see Section 4.3.2), and deviations from a gNFW model are not unexpected.

To get a more immediate sense of the reconstructed models, I show in Figure 4.12 the dirty images of VACA LoCA observations. As there are no sensible differences between the model and residual dirty images generated with different gNFW models, I here consider only the case of a universal pressure profile (Arnaud et al. 2010). I again emphasise that all the images reported here are only for illustrative purposes, and were not used in this analysis.

Cluster ID	$z_{\rm phot}$ –	λ –	M_{500} ($10^{14}\,M_\odot$)	$\sigma_{\rm eff}$ –	M_{500} ($10^{14}\,M_\odot$)	$\sigma_{\rm eff}$ –	M_{500} ($10^{14}\,M_\odot$)	$\sigma_{\rm eff}$ –	M_{500} ($10^{14}\,M_\odot$)	$\sigma_{\rm eff}$ –	M_{500} ($10^{14}\,M_\odot$)	$\sigma_{\rm eff}$ –
			universal		cool-core		disturbed		*Planck*		McDonald et al. 2014	
Significant detection												
MOO J0129−1640	$1.05^{+0.04}_{-0.05}$	49 ± 7	$2.57^{+0.30}_{-0.30}$	7.77	$2.09^{+0.24}_{-0.29}$	8.07	$3.47^{+0.32}_{-0.40}$	7.63	$2.75^{+0.32}_{-0.38}$	7.85	$3.72^{+1.28}_{-1.11}$	7.12
MOO J0345−2913	$1.08^{+0.03}_{-0.04}$	53 ± 7	$1.78^{+0.20}_{-0.29}$	5.32	$1.51^{+0.21}_{-0.24}$	5.71	$2.09^{+0.24}_{-0.38}$	5.35	$1.66^{+0.31}_{-0.31}$	5.58	$2.14^{+0.94}_{-0.74}$	5.24
MOO J0917−0700	$1.10^{+0.05}_{-0.05}$	58 ± 7	$1.66^{+0.31}_{-0.38}$	4.26	$1.48^{+0.22}_{-0.32}$	4.49	$1.93^{+0.49}_{-0.67}$	3.68	$1.55^{+0.38}_{-0.45}$	4.20	$1.77^{+0.85}_{-0.93}$	3.41
			$2.13^{+0.40}_{-0.49}$		$1.83^{+0.26}_{-0.38}$		$2.67^{+0.56}_{-0.84}$		$2.13^{+0.49}_{-0.60}$		$2.67^{+1.39}_{-1.47}$	
MOO J1139−1706	$1.31^{+0.03}_{-0.05}$	53 ± 7	$2.24^{+0.36}_{-0.52}$	3.81	$1.74^{+0.24}_{-0.36}$	3.82	$3.16^{+0.66}_{-0.87}$	3.40	$2.24^{+0.62}_{-0.57}$	3.78	$6.76^{+3.89}_{-3.42}$	4.35
MOO J1342−1913	$1.08^{+0.04}_{-0.05}$	41 ± 6	$1.95^{+0.31}_{-0.31}$	4.53	$1.58^{+0.22}_{-0.22}$	5.42	$2.29^{+0.37}_{-0.37}$	5.09	$1.91^{+0.35}_{-0.39}$	5.27	$2.40^{+0.94}_{-0.83}$	4.25
MOO J1414+0227	$1.02^{+0.07}_{-0.06}$	41 ± 7	$2.75^{+0.32}_{-0.32}$	6.99	$2.24^{+0.31}_{-0.26}$	6.80	$3.55^{+0.74}_{-0.41}$	6.98	$2.88^{+0.66}_{-0.53}$	7.04	$4.37^{+1.91}_{-1.81}$	6.94
MOO J2146−0320	$1.16^{+0.05}_{-0.05}$	50 ± 7	$1.86^{+0.34}_{-0.52}$	5.35	$1.58^{+0.27}_{-0.34}$	5.55	$2.58^{+0.56}_{-0.66}$	5.73	$1.95^{+0.47}_{-0.61}$	5.62	$5.13^{+4.57}_{-3.29}$	5.94
			$2.04^{+0.42}_{-0.56}$		$1.67^{+0.31}_{-0.40}$		$3.49^{+0.78}_{-1.14}$		$2.29^{+0.69}_{-0.79}$		$4.44^{+2.52}_{-3.39}$	
Weak detection												
MOO J1223+2420	$1.09^{+0.04}_{-0.04}$	51 ± 7	$1.17^{+0.27}_{-0.38}$	2.40	$0.94^{+0.21}_{-0.35}$	2.54	$1.33^{+0.34}_{-0.61}$	2.54	$0.90^{+0.32}_{-0.44}$	2.53	$1.52^{+0.86}_{-0.92}$	2.23
MOO J2147+1314	$1.01^{+0.06}_{-0.07}$	38 ± 6	$1.82^{+0.34}_{-0.42}$	1.26	$1.56^{+0.26}_{-0.38}$	1.34	$1.62^{+0.43}_{-0.52}$	1.59	$2.06^{+0.51}_{-0.50}$	1.23	$2.27^{+1.10}_{-1.26}$	1.35
Non detection												
MOO J0903+1310	$1.26^{+0.05}_{-0.08}$	29 ± 5	$0.30^{+0.18}$	–	$0.29^{+0.17}_{-0.20}$	0.83	$0.27^{+0.16}_{-0.16}$	0.88	$0.27^{+0.18}_{-0.18}$	0.61	$0.32^{+0.22}$	–

Table 4.4: Estimated masses of the VACA LoCA sample clusters. See Section 4.3 for more details about the effective significance estimate $\sigma_{\rm eff}$. The two mass values provided for MOO J0917−0700 and MOO J2146−0320 correspond to the masses of each of the individual SZ components detected.

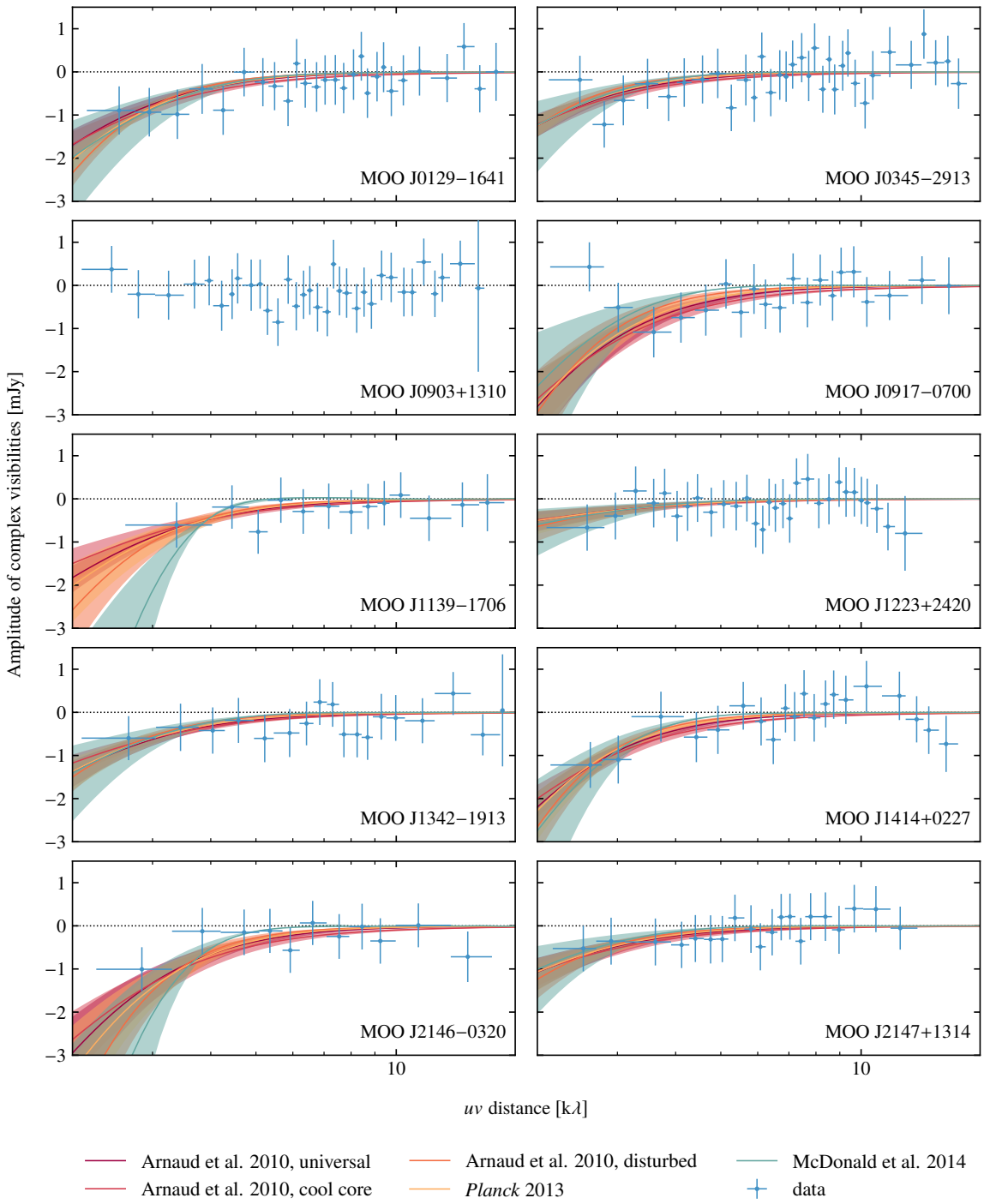

Figure 4.11: Comparison of the *uv* profiles of all the gNFW flavours adopted in the analysis of the VACA LoCA data. The data are binned so that each bin contains the same number of visibilities (here set to 2500 for plotting purposes). Before averaging, I shifted the phase centre to the position of cluster centroid to minimise the ringing effect due to non-zero phases. I do not plot any model profile for MOO J0903+1310 as the SZ signal is not detected.

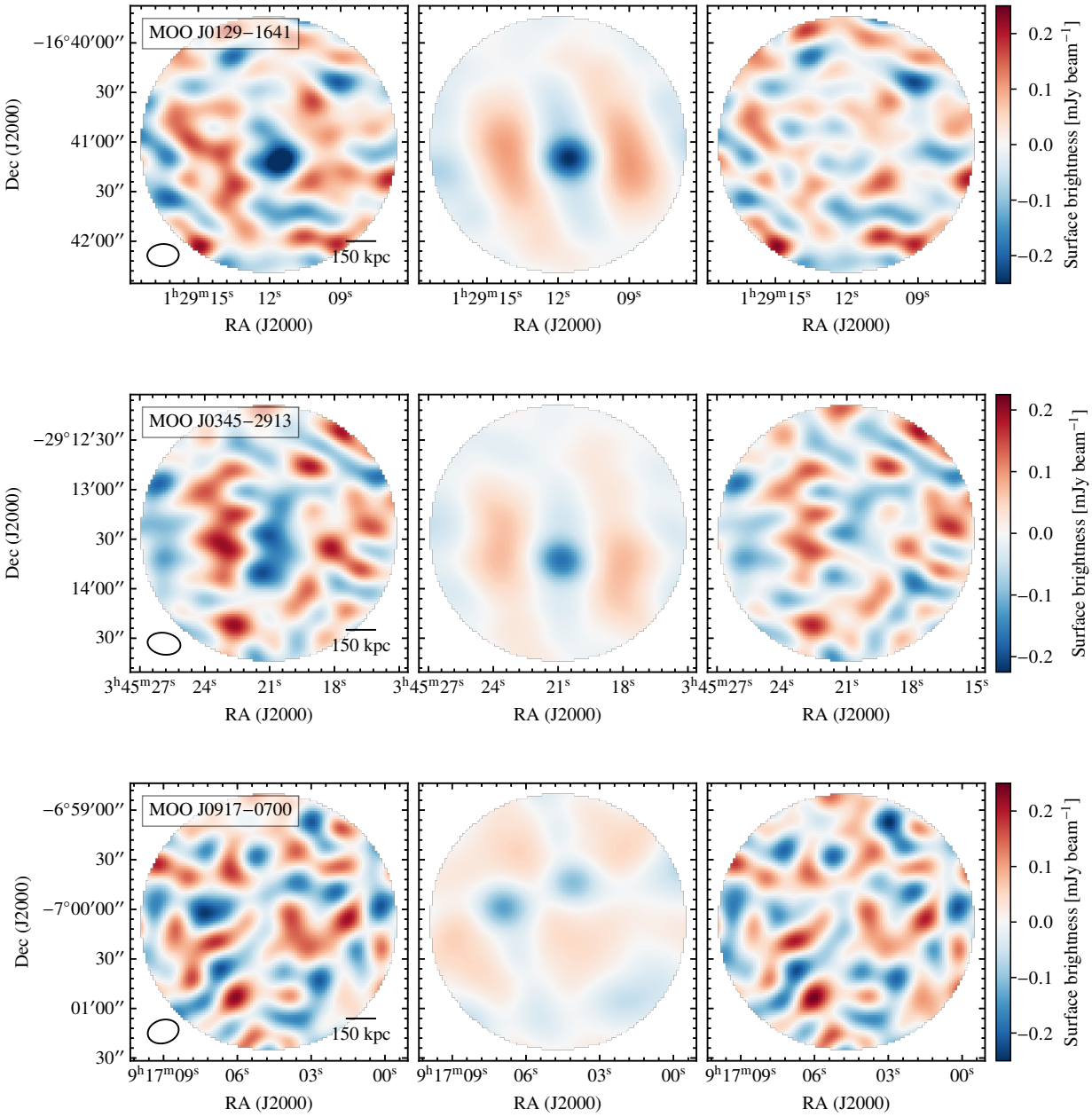

Figure 4.12: Dirty images of the raw (left), model (center), and residual (right) data of VACA LoCA observations. All the images are generated by applying a multi-frequency naturally-weighted, imaging scheme, and extend out to where the ACA primary beam reaches 20% of its peak amplitude. To better highlight the SZ features in each field, I apply a 10 kλ taper but do not correct for the primary beam attenuation. Further, as for Figure 4.3, I removed the most significant point-like sources from the raw interferometric data.

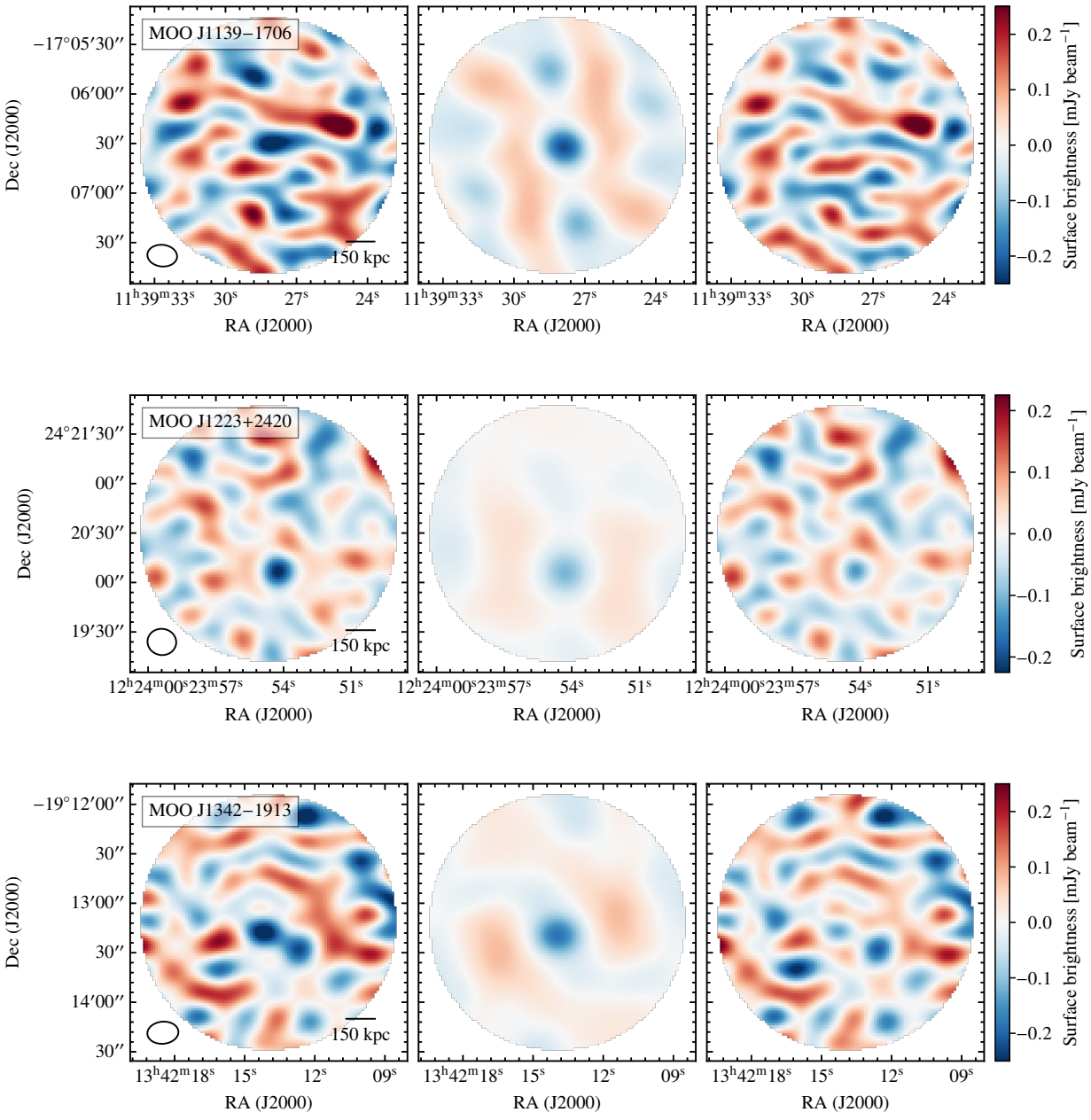

(continued from Figure 4.12)

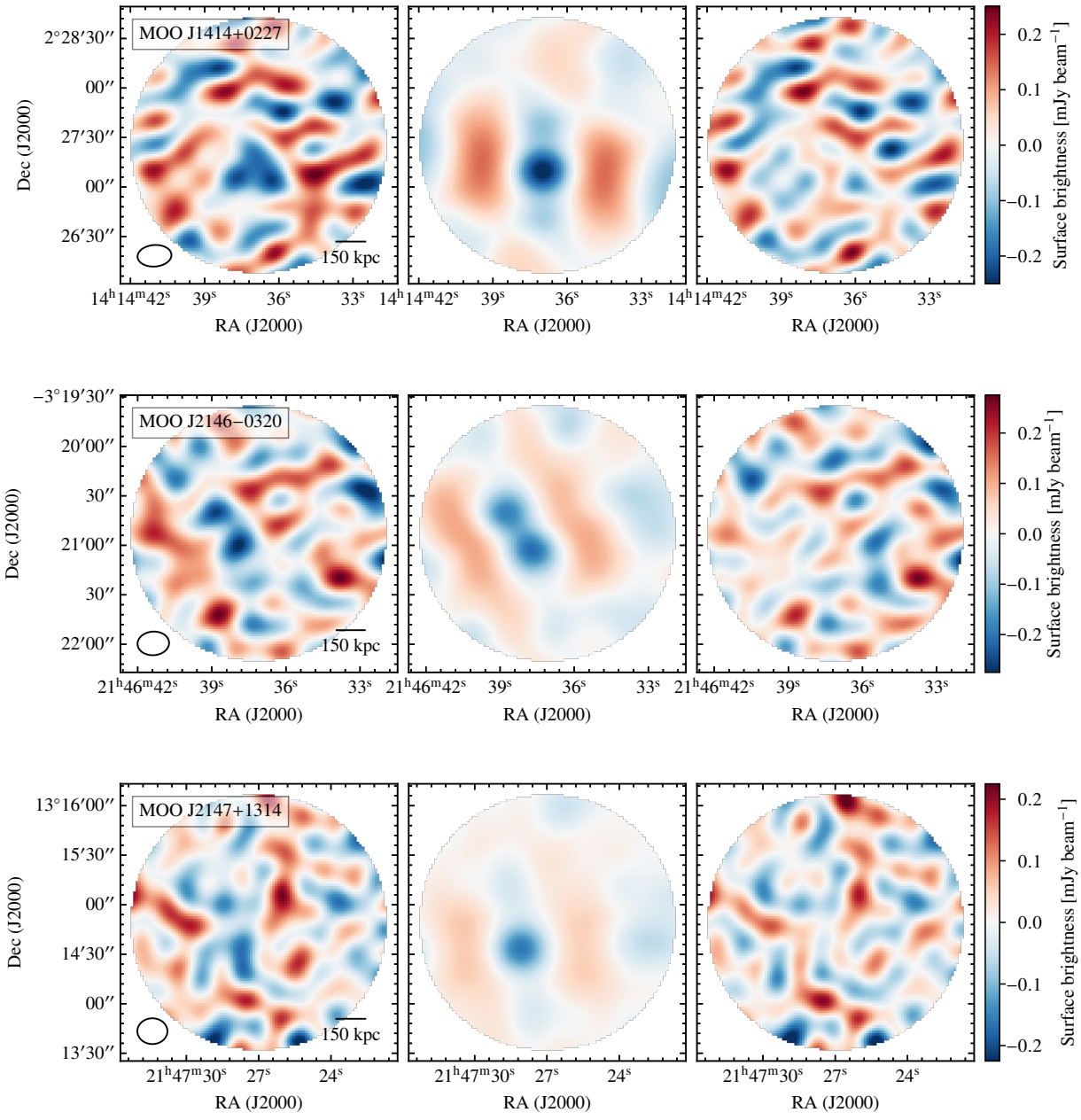

(continued from Figure 4.12)

Chapter 5

Conclusions

At present, ALMA+ACA is the only millimetre/submillimetre facility that can provide measurements of the SZ effect at an angular resolution better than ~ 8 arcsec. This thesis is devoted to understanding in detail ALMA+ACA potentialities for the study of the physics of galaxy clusters over an unprecedented range of spatial scales. In particular, central to this doctoral work has been the exploration of the novel opportunities offered by the measurements of the SZ signal as a window both independent and complementary to X-ray observations on the complex phenomenology exhibited by the intracluster medium. A summary of the main results presented in the previous chapters is reported below.

- The joint analysis of single-dish and interferometric observations of the SZ effect can provide a straightforward answer to the issues related to interferometric filtering as well as limited resolution of single-dish facilities. The techniques have been applied to a combination of measurements of the SZ effect from RX J1347.5–1145. Previous X-ray-motivated SZ studies of RX J1347.5–1145 have highlighted the presence of an excess SZ signal south-east of the X-ray peak. The joint SZ image-visibility pressure model, when centred at the X-ray peak, confirms this. However, the presence of two almost equally bright giant elliptical galaxies separated by ~ 100 kpc makes the choice of the cluster centre ambiguous, and allows for considerable freedom in modelling the structure of the galaxy cluster. For instance, the SZ signal can be well-described by a single smooth ellipsoidal generalised NFW profile, where the best-fitting centroid is located between the two brightest cluster galaxies. This leads to a considerably weaker excess SZ signal from the south-eastern substructure. Further, the most prominent features seen in the X-ray can be explained as predominantly isobaric structures, alleviating the need for highly supersonic velocities, although overpressurised regions associated with the moving subhaloes are still observed.

- The combination of deep, high-resolution interferometric SZ effect observations with priors from an independent X-ray analysis allowed for getting constraints on the mechanism governing electron heating across the shock front in the Bullet Cluster. In the case of instantaneous electron-ion temperature equilibration, the shock Mach number is found to be $\mathcal{M} = 2.08^{+0.12}_{-0.12}$, in $\approx 2.4\sigma$ tension with the independent constraint from *Chandra*, $\mathcal{M}_{\rm X} = 2.74 \pm 0.25$. The assumption of purely adiabatic electron temperature change

across the shock leads to $\mathcal{M} = 2.53^{+0.33}_{-0.25}$, in better agreement with the X-ray estimate $\mathcal{M}_X = 2.57 \pm 0.23$ derived for the same heating scenario. The analysis is however limited by systematics related to the overall cluster geometry and the complexity of the post-shock gas distribution.

- The analysis of the VACA LoCA sample provided significant detections of the SZ effect from seven out of the ten VACA LoCA clusters, two weak detections and only one non-detection. Remarkably, this result is largely independent of the specific model assumed for describing the cluster pressure profiles. However, the limited angular dynamic range of the ACA alone, short observational integration times, and possible contamination from unresolved sources limit the detailed characterisation of the cluster properties and the inference of the cluster masses within scales appropriate for the robust calibration of mass-richness scaling relations.

On the one hand, all results listed above highlight how ALMA+ACA can play a central role in yielding tremendous progress in our understanding of the physical processes ongoing within galaxy clusters. From a purely observational point of view, the possibility of discriminating between contaminant sources and the SZ effect at high angular resolution is key for getting a clean view of the small-scale features in the pressure distribution of the intracluster medium. In turn, the characterisation of the physical and thermodynamic properties of intracluster pressure substructures through SZ measurements and the combination with X-ray-derived information represent an unparalleled observational tool for getting deep insights in the extreme physics of the intracluster plasma. Further, the extraordinary angular resolution and sensitivity of ALMA+ACA allows for overcoming the limitations of current wide-field SZ surveys in detecting faint and high-redshift clusters due to their significant beam smearing effect. Thus, although the mapping speed is clearly not competitive when compared to the one of other ground-based survey facilities, the combination of ALMA and ACA further provides the means for observing the evolution of clusters and proto-clusters in the distant Universe.

On the other hand, the limitations introduced by the radio-interferometric observations are evident. First, the lack of short-spacing information makes ALMA+ACA-only studies of the SZ effect impractical in the case of nearby systems. In order to get sensible constraints on the pressure distribution of the intracluster medium, any analyses have to rely on external large-scale data, either SZ or X-ray. Second, in the case of more distant systems, the limited dynamic range of probed scales allows one to access the SZ signal only in the direction of the very central region of galaxy clusters, potentially biasing the inference of their global properties.

Both improved spatial and spectral resolution, larger instantaneous field of view, and the ability to recover zero-spacing information will vastly improve future SZ studies. In the next few years, ALMA Bands 1 (35-51 GHz; Di Francesco et al. 2013, Huang et al. 2016) and 2 (67-116 GHz; Yagoubov et al. 2020) will further increase the maximum recoverable scale and thus the sensitivity of ALMA and the ACA to diffuse, low surface brightness signals on arcminute scales. At the same time, new thermal and kinematic SZ imaging possibilities with bolometric/photometric arrays such as TolTEC on the 50m Large Millimeter Telescope (Bryan et al. 2018), MUSTANG-2 on the 100m GBT (Dicker et al. 2014), and NIKA2 on the IRAM 30-meter telescope (Adam

et al. 2018a) will deliver such data through targeted cluster observations. However, in order to provide sufficient overlap with the interferometric data in Fourier space, while also probing higher frequencies and spatial scales >10′, a new wide-field (> 1°) single-dish facility, such as the Atacama Large Aperture Submm/mm Telescope (AtLAST; see, e.g., Klaassen et al. 2019, Mroczkowski et al. 2019a) or the Large Submillimeter Telescope (LST; Kawabe et al. 2016), is required.

5.1 Future prospects

All the works based on ALMA+ACA observations of the SZ effect that are currently published (Kitayama et al. 2016, Basu et al. 2016, Ueda et al. 2018, Kitayama et al. 2020, Gobat et al. 2019, Lacy et al. 2019, Brownson et al. 2019), as well as the ones presented in this thesis, mainly represent exploratory studies of ALMA+ACA capabilities in measuring the SZ effect from a variety of astrophysical environments. High-resolution imaging and detection of the SZ effect is however slowly becoming a tool routinely employed for probing the warm and hot Universe. Here, I provide an overview of future works and potential applications of ALMA+ACA measurements of the SZ effect.

5.1.1 Merger physics

As a consequence of the severe filtering affecting the ALMA+ACA data, the analysis of the bow shock in the Bullet Cluster presented in Chapter 3 heavily relied on X-ray prior information for setting the normalisation of the upstream electron pressure. However, the X-ray data were crucial also for constraining the plane-of-sky geometry of the shock front, as well as the azimuthal variation of the shock Mach number. The field of view the ALMA+ACA measurements in fact limited the study of the shock properties only to the region just around its nose. To gain a more comprehensive description of the shock geometry, I have been awarded 36.2 hours of on-source observing time with ACA (project ID: 2019.2.00081.S). The observation is aimed at mapping a more extended region of the shock front, providing an SZ-only view of the off-axis properties of the shock. A deeper understanding of the shock geometry and the azimuthal variability of the shock Mach number will be key for improving the current constraints on the shock properties. As broadly discussed in Section 3.3, the joint analysis of X-ray and SZ data will represent a fundamental step towards the proper characterisation of the temperature jump condition across the front and, then, of the electron heating scenario. Further, the joint modelling will allow for breaking (or at least reducing) the degeneracy between the line-of-sight geometry of the shock front and its Mach number.

The requested mosaic will further cover the region corresponding to the bright cold front behind the shock in the Bullet Cluster. In principle, no significant jump is expected to be observed in the SZ signal. Since cold fronts form as a result of subsonic bulk motion of gas, the electron pressure is in fact predicted to be continuous across the contact discontinuity. However, as introduced in Section 1.2.1, non-thermal pressure support due to ram pressure or magnetic fields may introduce local deviations from the pressure equilibrium. As a consequence

of the uncertain line-of-sight dependence, the standard assumption of pressure continuity cannot however be tested with X-ray data alone. The proposed observations will hence be important for providing an additional, valuable test of shock dynamics.

5.1.2 Galaxy proto-clusters studies

As highlighted before, ALMA+ACA resolution allows us to get a direct of view of the warm/hot plasma within large-scale structures at high redshifts. The cosmic time at $z \gtrsim 2$ is central in the assembly history of the clusters and cluster galaxies we see today. This epoch corresponds to when the build-up of the intracluster medium first happens, along with the onset of its heating and metal enrichment mechanisms, the formation of BCGs, and enhancements of AGN and star-formation activities within the hot gaseous haloes. Galaxy proto-clusters result from the most active phase of such structure formation activity, and their study can play a transformative role in improving our understanding of cluster and galaxy formation (see Miley & De Breuck 2008 and Overzier 2016 for a review).

As the proto-cluster regions are expected to accrete large amounts of hot, ionized gas, we should be able to observe their X-ray emission due to thermal bremsstrahlung as well as their SZ signature. I am thus now involved in the a first exploratory study of the environment surrounding the Spiderweb galaxy, generally recognised as the archetypal galaxy proto-cluster, aimed at detecting the hot intracluster medium via the thermal SZ effect. Both cosmological hydrodynamic simulations (Saro et al. 2009) and observations (Carilli et al. 2002, Miley et al. 2006) strongly support the presence of a diffuse, ionised atmosphere in quasi-hydrostatic equilibrium filling a volume with a radius of $\sim$ 0.2 Mpc. Currently, my work is focused on an extension of the modelling tool employed for providing the results presented in this thesis. In particular, most of the efforts is in the development of an analysis routine able to handle the exceptional dynamic range of angular scales probed by the available ALMA+ACA data set (project ID: 2018.1.01526.S, PI: A. Saro), so to reconstruct a map of the SZ signal with an unparalleled spatial resolution of $\sim$ 2 kpc. Further, the measurements of the SZ effect from the Spiderweb proto-cluster would represent the first, direct detection of the SZ signal from a proto-cluster complex, providing first hints about the thermodynamic and environmental properties of the intracluster medium in massive systems at $z \sim 2$.

5.1.3 Follow-up with pointed SZ observations

The large volume that will be probed in the next four years by the state-of-art X-ray wide-field survey satellite, the Extended ROentgen Survey with an Imaging Telescope Array (eROSITA; Merloni et al. 2012) on the Russian-German Spectrum-Roentgen-Gamma (SRG) satellite, will result in the discovery of $\sim 10^5$ new galaxy clusters, extending even beyond $z > 1$ (Pillepich et al. 2012). Campaigns aimed at systematically following-up a representative sample of clusters from the survey will be essential. The improved constraints on the masses of individual clusters, as well as on their physical and thermodynamic state will in fact be central for gaining an accurate cross-calibration of X-ray- and SZ-based mass-observable scaling relations and for studying the redshift evolution of the cluster properties.

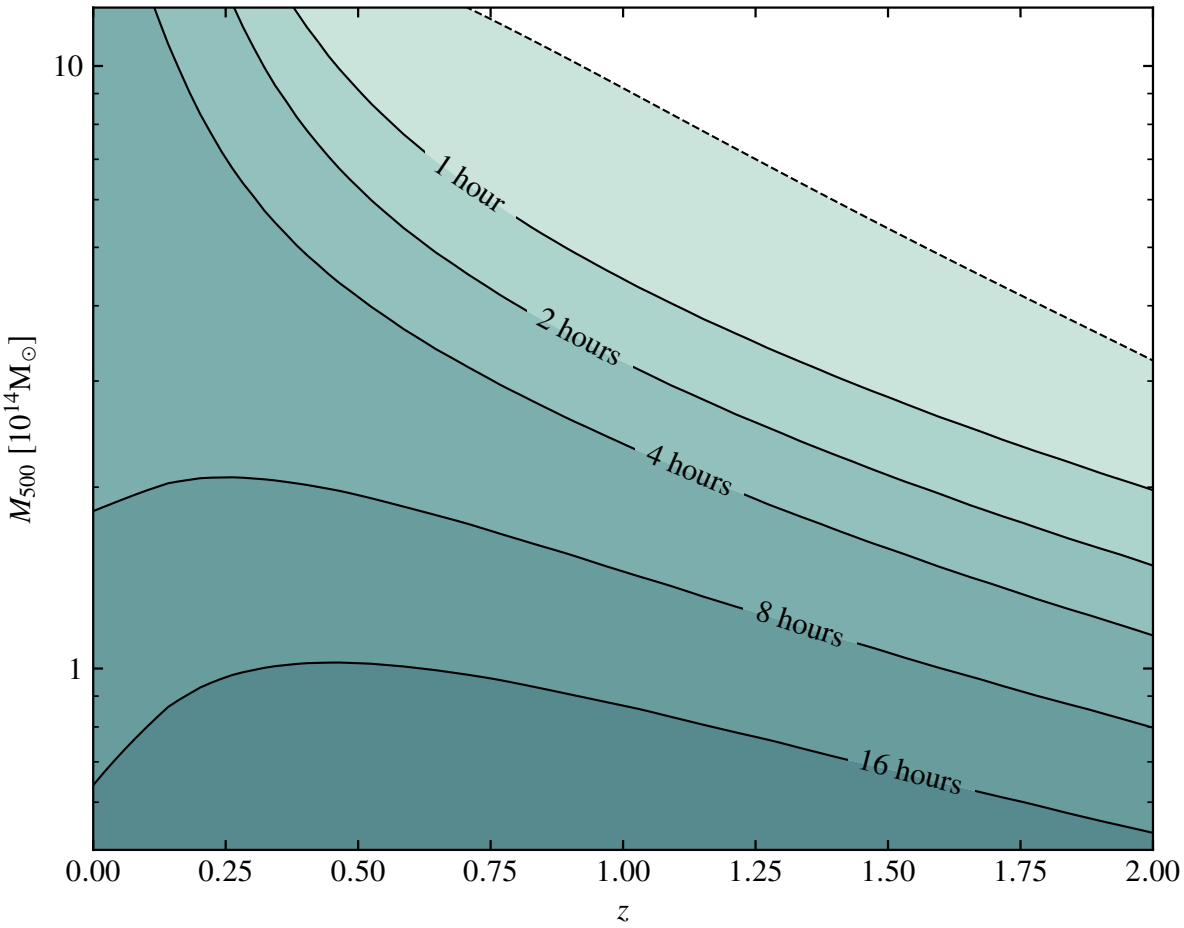

Figure 5.1: ACA integration time required to measure the integrated SZ signal from a galaxy cluster with a significance of 5σ as a function of the cluster mass and redshift. The simulations comprise a broad-band spectral coverage as for typical Band 3 observations of the SZ effect (i.e., four spectral windows with bandwidth of 2 GHz and covering the frequency ranges 84 – 88 GHz and 96 – 100 GHz). Further, the SZ signal is computed by considering a universal pressure profile (Arnaud et al. 2010) as model of the electron pressure distribution. The cluster centroid is set to coincide with the maxi of the primary beam pattern, in turn corresponding with the phase reference direction of the synthetic visibilities. Finally, the cluster is assumed to be observed at transit, thus to reduce the asymmetry in the *uv*-coverage (Thompson et al. 1986). See Appendix C for a more extended discussion. The white region above the dashed line (upper right) denotes the range of masses at every redshift for which the full-sky cluster number count is smaller than unity.

The limited mapping speed of ALMA+ACA does not allow for surveying large fractions of the sky, and single-dish CMB experiments like ACT (Hilton et al. 2018) and SPT (Bleem et al. 2015, 2020) will play a key role in complementing the comprehensive eROSITA cluster survey by extending the already vast catalogue of SZ-identified sources. However, the improved angular resolution offered by ALMA+ACA makes it highly competitive for providing single-target

follow-ups of a representative sub-sample of galaxy clusters discovered by eROSITA. As already discussed, this will offer the unique opportunity to get a combined SZ+X-ray view of the physical properties of high-redshift systems, as well as an observationally inexpensive confirmation of the presence of hot intracluster medium. In Figure 5.1, I provide an estimate of the integration time required by ACA[1] in Band 3 to measure the integrated SZ signal from a galaxy cluster at 5σ significance level as a function of the mass and redshift. For comparison, I introduce a high-mass cut representing the highest cluster mass one should expect to observe at any given redshifts. For each value of z, the threshold $M_{500,\mathrm{th}}$ is estimated as the one for which the volume integral of the cumulative number density of clusters with masses above $M_{500,\mathrm{th}}$ is unitary. In the computation, I employed the parametrisation derived by Bocquet et al. (2016) for defining the input halo mass function.

Overall, the detection significance of a cluster at a given mass increases (i.e., the integration time required to reach a given significance level decreases) as a function of the cluster redshift. This is not unexpected in the case of galaxy clusters observed via the SZ effect. The mass employed in the prediction is indeed defined with respect to the value of the critical density of the Universe at the redshift of the cluster, whose redshift evolution is reflected in an increase of the SZ surface brightness of a cluster with given mass M_{500}. This couples with the redshift independence of the SZ surface brightness, thus providing an effective improvement of the signal-to-noise ratio for distant systems. On the other hand, as a result of the increase of the angular diameter distance with the redshift (till the approximate flattening in the redshift range $1 \lesssim z \lesssim 2$), the large-scale SZ signal from the furthest clusters is better probed by ACA, as the measurements become less affected by the short-spacing limitations (see Section 1.2.2). Consequently, the integrated SZ flux for fixed cluster mass and array configuration and, hence, the cluster detectability are also increasing functions of cluster redshift. The same effect can be observed for the lowest masses, as a smaller M_{500} would correspond to a smaller cluster diameter (Equation 4.4), resulting in the cluster SZ signal to be measured by an interferometer on a broader range of physical scales.

It is worth noting that the sensitivity estimates in Figure 5.1 do not account for the expected decrease in the significance of the SZ effect detection due to presence of unresolved or extended radio emission. As broadly discussed in Chapter 4, these can in fact strongly contaminate the SZ signal from a galaxy cluster, and, consequently, limit the possibility of its robust characterisation. Further effects potentially contributing to an effective variation of the measured signal-to-noise ratio are discussed in Appendix C.

[1] Although ALMA has a total collecting area $\sim$ 12 times larger than ACA and, hence, a much greater sensitivity, ALMA observations are critically affected by the filtering of any angular scale important for detecting the bulk of the extended SZ signature of a galaxy cluster. This would limit the possibility of obtaining a firm confirmation of the SZ signal. As a result, any predictions for the respective signal-to-noise ratio would not be entirely reliable, and are not included in the plot.

Appendix A

Joint image-visibility analysis

The content of this chapter is based on the appendix to the work originally published as ***Di Mascolo, L.****, Churazov, E., & Mroczkowski, T., 2019, MNRAS, 487, 4037*

In this appendix, I present the salient features of the image and visibility analyses employed in this work. As already stated in Chapter 2, the flexibility of the modelling technique makes it extensible to SZ data from any instruments, as well as to non-SZ interferometric, bolometric, photometric, and spectroscopic observations from the radio to the millimetre/submillimetre regime.

A.1 Model description

Suppose to obtain a data set $\boldsymbol{d}$, which provides a measure of the true sky/astronomical signal $\boldsymbol{s}$. In the case of a real experiment, this consists only of a filtered view of the real sky, due to the instrumental response and any pre-processing step applied to the data. Moreover, any measurement is inevitably contaminated by experimental noise. Assuming this to be characterised only by an additive component $\boldsymbol{n}$, the data set $\boldsymbol{d}$ can be written as

$$\boldsymbol{d} = \mathsf{T}\,\boldsymbol{s} + \boldsymbol{n}. \tag{A.1}$$

where the transfer operator T is introduced to account for any instrument-specific filtering effects.

The description of the sky signal is of course independent of the specific observations employed in the modelling process, and any instrument-specific effect enters the overall model $\boldsymbol{m}$ only through the transfer operator T. I now focus on describing the signal $\boldsymbol{s}$, considered as the surface brightness distribution in a collection of directions on the sky, and introduce a model for the main astrophysical components that are dominant when observing galaxy clusters at millimetre wavelengths.

A.1.1 Thermal Sunyaev–Zeldovich effect

As broadly discussed in Section 1.1.1, the variation imprinted in the CMB surface brightness in the direction of a galaxy cluster is

$$\delta i_{\rm tSZ}(\nu) = i_{\rm CMB}\, g_{\rm tSZ}(\nu)\, [1 + \delta_{\rm tSZ}(\nu, T_{\rm e})]\, y. \tag{A.2}$$

Here, the term $g_{\rm tSZ}(\nu)$ represents the frequency-dependent scaling of the non-relativistic thermal SZ effect,

$$g_{\rm tSZ}(\nu) = \frac{x^4 {\rm e}^x}{({\rm e}^x - 1)^2} \left(x \frac{{\rm e}^x + 1}{{\rm e}^x - 1} - 4 \right), \tag{A.3}$$

while $\delta_{\rm e}(\nu, T_{\rm e})$ quantifies the respctive correction due to relativistic effects. Throughout this thesis, correction coefficient has been computet using the formulation by Itoh & Nozawa (2004).

A.1.2 Unresolved sources

Strong contamination may arise in the measured SZ effect due to the presence of point-like sources in the direction of the observed galaxy cluster. These may be due to radio emission from the cluster member galaxies, as well as foreground or background compact objects, which are bright at millimetre and submillimetre wavelengths. On the other hand, the presence of an underlying SZ component may bias the estimate of the source flux and spectral properties, thus affecting its removal from the analysed data.

When modelling an unresolved source, the general approach consists in exploiting the scale separation between the extended SZ effect component and the contaminating source, which is supposed to dominate the overall signal at the smallest scales. This is particularly suitable when analysing interferometric data, for which it is possible to take advantage of the natural spatial scale filtering for discriminating between the extended and point-like components. However, the choice of the scale range over which the fitting should be performed is fairly arbitrary. In order to avoid such freedom and, thus, possible misinterpretations of the results of the fit, any observed point-like objects are more consistently modelled jointly with the extended SZ signal.

Being point-like on the scales probed by the observations, an unresolved source can be described as a Dirac delta function at a position on the sky $\boldsymbol{x}_{\rm PS} = (x_{\rm PS}, y_{\rm PS})$ with flux density $i_{\rm PSi}$ at a given reference frequency $\nu_{\rm PS}$,

$$i_{\rm PS}(\boldsymbol{x}, \nu) = \delta_{\rm D}(\boldsymbol{x} - \boldsymbol{x}_{\rm PS})\, i_{\rm PSi}\, g_{\rm PS}(\nu). \tag{A.4}$$

where $g_{\rm PS}(\nu)$ represents the frequency spectrum of the point-source model. In this thesis, I adopt a simple power-law dependence with spectral index $\alpha_{\rm PS}$, yielding

$$g_{\rm PS}(\nu) = (\nu/\nu_{\rm PS})^{\alpha_{\rm PS}}. \tag{A.5}$$

A.1.3 Other components

The above procedure only makes sense for those objects characterised by a flux density above the threshold set by the instrument sensitivity (or, potentially, by the confusion limit of the

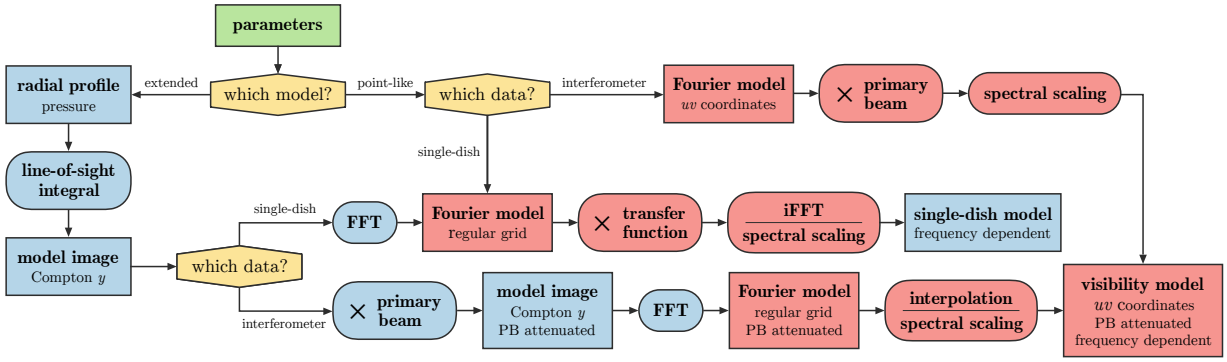

Figure A.1: Schematic flow diagram of the algorithm for modelling single-dish and interferometric data. The solid rectangles represent the data products employed in the computations, while the specific operations are indicated in rounded rectangles. I highlight in blue and in red all the quantities and functions defined respectively in image- and Fourier-space.

observations if not enough constraints are available to model it). On the other hand, faint, undetected radio sources identified using ancillary radio catalogues may be subtracted a priori from the input data sets if their fluxes can be accurately estimated. However, uncertainties in the spectral model may result in the wrong extrapolation of the source fluxes at the required frequencies. Moreover, residual unresolved sources near or below the confusion limit may still contribute to the total measured signal and affect the analysis of the SZ effect by introducing significant contamination. It is then possible to account for the resulting bias in terms of additional uncertainties in the measured flux density.

Similarly, the amplitude of the primary CMB anisotropies at scales comparable to the angular size of a given galaxy cluster may be non-negligible with respect to the thermal SZ flux density. A statistical description of the overall impact of the CMB on the measured SZ signal can be derived from the power spectrum of CMB fluctuations.

I include the overall effect of both point-like sources and CMB contamination in the noise model. In practice, the covariance matrix employed in the computation of the likelihood function of the model can be generalised to

$$\mathbf{C} = \mathbf{C}_{\mathrm{N}} + \mathbf{C}_{\mathrm{PS}} + \mathbf{C}_{\mathrm{CMB}} \tag{A.6}$$

Here, $\mathbf{C}_{\mathrm{N}}$, $\mathbf{C}_{\mathrm{PS}}$, and $\mathbf{C}_{\mathrm{CMB}}$ define the instrumental, unresolved-source, and CMB covariance matrices, respectively. For simplicity, I assumed that neither the compact sources nor CMB are spatially correlated with the SZ signal.

A.2 Data likelihood

As shown in Eq. (A.1), the proper comparison of a parametric representation of an astrophysical signal to any input measurement relies on the characterisation of the effects of the transfer function

on the observed sky. Here, I detail how they can be taken into account differently in the case of single-dish and interferometric observations. A schematic representation of the derivation of the data models is presented in Figure A.1. For the sake of readability, I omit hereafter the subscript denoting the specific subset of data and the respective model unless strictly required. All the quantities discussed here can be generalised to each of the individual observations.

A.2.1 Image-space observations

For a set of image-domain data, the effect of the transfer operator in Eq. (A.1) can be summarized in terms of a combination of the smoothing due to the finite angular resolution of the telescope, and some large-scale filtering as a consequence of the scanning and map-making strategies. It acts on the true signal as a convolution kernel, making it computationally more convenient to be treated in Fourier space. By applying the convolution theorem, the map of a generic model component can be written as

$$\boldsymbol{m}_{\rm img}(\boldsymbol{x},\nu) = [\mathbf{T}_{\rm img} * \boldsymbol{s}](\boldsymbol{x},\nu) = \int [\tilde{\mathbf{T}}_{\rm img}\,\tilde{\boldsymbol{s}}](\boldsymbol{u},\nu)\,\mathrm{e}^{-2\pi j \boldsymbol{u}\cdot\boldsymbol{x}}\mathrm{d}\boldsymbol{u}, \tag{A.7}$$

where I denote with a tilde the Fourier transform of a given function. As before, $\boldsymbol{x}$ represents the vectorial direction on the sky of the observed signal, while $\boldsymbol{u}$ describes the Fourier-space coordinates.

The unfiltered model for the extended thermal SZ signal over a set of directions $\boldsymbol{x}$ is computed as

$$\boldsymbol{s}_{\rm tsz}(\boldsymbol{x},\omega) = i_{\rm CMB}\,\bar{g}_{\rm tsz}(\omega, T_{\rm e})\,y(\boldsymbol{x}), \tag{A.8}$$

where I introduced the bandpass function $\omega = \omega(\nu)$. Indeed, a real instrument observes the sky over a given range of frequencies with non-uniform spectral response, due to a combination of instrumental effects and atmospheric transmission. The frequency dependence of the measured SZ effect is then expressed by the bandpass-averaged spectral function

$$\bar{g}_{\rm tsz}(\omega, T_{\rm e}) = \frac{\int \omega(\nu')\,g_{\rm tsz}(\nu')[1+\delta_{\rm tsz}(\nu', T_{\rm e})]\,\mathrm{d}\nu'}{\int \omega(\nu')\,\mathrm{d}\nu'}, \tag{A.9}$$

In the specific case of a point-like source, I can employ the sifting property of the Dirac delta function to immediately define its model as being equal to the convolution kernel $\mathbf{T}_{\rm img}$ centred at the position of the source and scaled by the source amplitude at the frequency ν of the given observation. From Eq. (A.4), considering bandpass-averaged quantities,

$$[\mathbf{T}_{\rm img} * \boldsymbol{s}_{\rm PS}](\boldsymbol{x},\omega) = \bar{g}_{\rm PS}(\omega)\,\boldsymbol{s}_{\rm PS}(\boldsymbol{x}_{\rm PS})\,\mathbf{T}_{\rm img}(\boldsymbol{x}-\boldsymbol{x}_{\rm PS},\omega). \tag{A.10}$$

where $\bar{g}_{\rm PS}$ is defined analogously to Eq. (A.9) for the case of a power-law spectral model. By using the Fourier shift theorem, the transfer term on the right-hand side of the above equation can then be computed as

$$\mathbf{T}_{\rm img}(\boldsymbol{x}-\boldsymbol{x}_{\rm PS},\omega) = \int \left[\tilde{\mathbf{T}}_{\rm img}(\boldsymbol{u},\omega)\,\mathrm{e}^{2\pi i \boldsymbol{u}\cdot\boldsymbol{x}_{\rm PS}}\right]\mathrm{e}^{-2\pi j \boldsymbol{u}\cdot\boldsymbol{x}}\mathrm{d}\boldsymbol{u}. \tag{A.11}$$

The total model map $\boldsymbol{m}_{\rm img}$ employed for evaluating the image likelihood function can then be easily obtained by summing over all the arbitrary number of components of the parametric model.

The generalised covariance matrix required for computing the data likelihood may be strongly non-diagonal in the case of image-space data (for a discussion, I refer to, e.g., Condon 1974, and Knox et al. 2004). Even omitting the effects of gravitational lensing and of the spatial clustering of the sources, the component of the covariance matrix associated with the confusion noise shows off-diagonal terms due to the spatial correlation induced by the finite resolution. On the other hand, from the properties of the spherical harmonics, the elements of the CMB covariance matrix associated with any two pixels at a given angular separation $\theta_{\rm ij}$ can be written as

$$[\mathbf{C}_{\rm CMB}]_{\rm ij} = \sum_{l} \frac{2l+1}{4\pi} C_l \, P_l(\cos\theta_{\rm ij}), \tag{A.12}$$

where C_l is the value at the multipole l of the primary CMB power spectrum and P_l the Legendre polynomial of order l.

A.2.2 Interferometric data

Following the discussion in Section 1.2.2 and using a notation analogous to the one in the previous sections, the model for the interferometric data can be defined as

$$\tilde{\boldsymbol{m}}_{\rm vis}(\boldsymbol{u}, \nu) = \tilde{\mathbf{T}}_{\rm vis}(\boldsymbol{u}, \nu) \int \mathbf{A}(\boldsymbol{x}, \nu)\, \boldsymbol{s}(\boldsymbol{x}, \nu)\, \mathrm{e}^{2\pi i \boldsymbol{u}\cdot\boldsymbol{x}} \mathrm{d}\boldsymbol{x}. \tag{A.13}$$

where $\tilde{\mathbf{T}}_{\rm vis}(\boldsymbol{u}, \nu)$ accounts for the incomplete sampling of the uv-space.

The visibilities for extended model components are computed by resampling the regularly gridded Fourier transform of the corresponding model map onto the coordinates of the sparse interferometric data. The input, unsmoothed model image is produced as for the case of the image-domain fitting described earlier. However, instead of applying any filtering, it is only attenuated by the input primary beam pattern before being Fourier transformed.

Unlike for extended sources, the modelling of unresolved sources is straightforward, since, as mentioned in the previous section, they can immediately be defined in Fourier space. Substituting the signal model in Eq. (A.13) with the expression for a point-like component of Eq. (A.4), one obtains

$$[\tilde{\boldsymbol{m}}_{\rm vis}(\boldsymbol{u}, \omega)]_{\rm PS} = \tilde{\mathbf{T}}_{\rm vis}(\boldsymbol{u}, \omega) \mathbf{A}(\boldsymbol{x}_{\rm PS}, \omega)\, i_{\rm PSi}\, \bar{g}_{\rm PS}(\omega)\, \mathrm{e}^{2\pi i \boldsymbol{u}\cdot\boldsymbol{x}_{\rm PS}}. \tag{A.14}$$

It follows that any residual unresolved sources result in an offset term in the complex amplitude of the interferometric data. Therefore, it is possible to avoid including the confusion term inside the generalised noise covariance matrix and treat it as a constant level in the Fourier-space model to be subtracted during the parametric reconstruction.

On the other hand, CMB power declines significantly when considering ever smaller scales as a consequence of Silk diffusion damping (Silk 1968), implying that CMB contamination affects mainly the visibilities with the shortest spacings. Moreover, since it represents the effect of a

spatially defined astrophysical signal, it generates correlated visibilities and, then, a non-diagonal covariance matrix. The computation of the CMB covariance for interferometric observations is presented in Hobson & Maisinger (2002). However, the filtering effect resulting from the missing short spacings can make the contribution to noise from CMB fluctuations generally negligible even at large scales when compared to the instrumental component. This is assumed to be uncorrelated, leading to a diagonal noise covariance matrix. It follows that, in such a case, the exponent of the interferometric likelihood reduces to

$$\left[(\boldsymbol{d}-\boldsymbol{m})^{\dagger}\mathbf{C}^{-1}(\boldsymbol{d}-\boldsymbol{m})\right]_{\mathrm{vis}} \approx \tilde{\boldsymbol{w}}_{\mathrm{vis}} \cdot |\tilde{\boldsymbol{d}}_{\mathrm{vis}} - \tilde{\boldsymbol{m}}_{\mathrm{vis}}|^2, \tag{A.15}$$

where the factor $\tilde{\boldsymbol{w}}_{\mathrm{vis}}$ represents the set of theoretical post-calibration visibility weights, equal to the inverse of the noise variance of the corresponding interferometric measurement (Wrobel & Walker 1999). Here, the dagger symbol is used to denote the conjugate transpose.

A.2.3 Integrated Compton parameter

Additional constraints on the pressure profile may be introduced by including information about the integrated thermal SZ flux obtained from the aperture photometry of the cluster Compton y map. This is proportional to the volume integral of the ICM pressure distribution and, hence, it is a fundamental proxy of the total thermal energy and mass of a galaxy cluster (see, e.g., Mroczkowski et al. 2019b).

It is possible to define the cylindrically integrated Compton parameter Y_{cyl} as the surface integral over a given solid angle Ω_{max} of the cluster Compton parameter y distribution,

$$Y_{\mathrm{cyl}} = \int_{\Omega_{\mathrm{max}}} y \, \mathrm{d}\Omega. \tag{A.16}$$

In the analyses, instead of characterising possible contributions arising from considering images with given finite angular resolution and large-scale filtering properties, I compare the integrated Compton parameter Y_{cyl} measured from a map characterised by the transfer operator $\mathbf{T}_{\mathrm{int}}$ with the respective value obtained from a filtered version of the model Compton y map, $[\mathbf{T}_{\mathrm{int}} * \boldsymbol{s}_{\mathrm{tsz}}]$. The corresponding likelihood function is then combined with the ones obtained by modelling the image and interferometric data.

A.3 A note on the computation of visibility models

In order to actually compute a model that best-fits the radio-interferometric data employed in a given analysis, it is necessary to convert the model signal distribution $\boldsymbol{s}(\boldsymbol{x}, \nu)$ to uv-space. In principle and as already detailed in Section A.2.2 above, a model visibility function can be defined by means of an exact evaluation of the interferometric integral in Equation 1.8 (or Equation 1.9 in the limit of flat-sky approximation). This would correspond to computing the direct Fourier transform of $\boldsymbol{s}(\boldsymbol{x}, \nu)$ at the M positions of the sampled uv-points. Assuming $\boldsymbol{s}(\boldsymbol{x}, \nu)$ to be approximated by a discrete representation over a collection of N pixels, it follows that the direct

estimation of Equation 1.8 would require $O(MN)$ computations. However, both the requirement of images at high angular resolution and the fact that typical radio-interferometric data sets comprise more than 10^6 visibilities are making such operations computationally prohibitive.

A common solution consists in approximating the direct Fourier transform by a non-uniform fast Fourier transform. This practically consists of a combination of the application of a fast Fourier transform to the regularly gridded image-space model, and a subsequent interpolation of the sparse visibilities off the Fourier grid, hence reducing the overall computational complexity to $O(M + N \log N)$. Convolutional interpolation techniques (Jackson et al. 1991) represent the common choice for approaching gridding and de-gridding problems in radio-interferometric imaging (Thompson et al. 1986), but are based slow, non-local convolution operations. This may put a strong limitation in their application in the framework of MCMC analyses as the ones presented in this thesis, for which a large number of model estimations are required. On the other hand, bilinear interpolation (Press et al. 1989) provides a computationally inexpensive and accurate alternative for projecting a Fourier model on a regular grid onto the sampled positions in the uv-plane. As visibilities are complex quantities, the interpolation process has to be applied separately on their complex components, i.e., their real and imaginary parts.

For sources far off the phase reference direction of the measured visibilities, or for extended signals as galaxy clusters, the interpolation from the gridded Fourier transform may however cause a dangerous flux loss. This is simply caused by the highly fluctuating nature of the real and imaginary parts of the complex visibilities in the case of a signal at relatively large distances from the centre of the observed field. The interpolation of visibility amplitudes and phases offers a direct alternative. This is however also limited by the fact the complex phase is generally evaluated as the argument of a complex number over the interval $(-\pi, \pi]$. As for the real and imaginary components, this may result in strong variations of the phases in neighbour pixels. The net consequence would be a miscalculation of the interpolated phases and, then, of the position of source model.

I found that a simple but effective solution to the above issues is provided by a combination of the two interpolation alternatives. The Fourier-transform amplitudes are not affected by any ringing effects induced by the fast variating phases, so that the amplitude of the sparse visibilities can be derived by interpolating the one of the Fourier grid to the position of the sampled uv points. On the other hand, the real and imaginary components depend in the same way on the complex phase. The computation of the visibility phases as the arctangent of the interpolated real and imaginary components can thus minimise the systematic issue on the phase interpolation. As this approach requires an additional interpolation step with respect to the real-imaginary or amplitude-phase cases, it of course comes at the expense of an overall performance loss in the generation of model visibilities[1].

[1]I point to the Github thread https://github.com/mtazzari/galario/pull/132 for a discussion about the specific implementation of the bilinear interpolation in GALARIO, one of the main libraries employed for deriving all results presented in this thesis.

Appendix B

Triaxial ellipsoidal profile

This appendix was originally published in ***Di Mascolo, L.****, Churazov, E., & Mroczkowski, T., 2019, MNRAS, 487, 4037*

Any radial pressure profile can be easily extended to describe a triaxial ellipsoidal distribution. Indeed, the information about the different characteristic extents of the ellipsoid principal axes can be included in a generalised dimensionless radius ξ, which can then be considered instead of the ratio $(r/r_{\rm s})$ for computing the pressure profile in Eq. (2.2). Since it is not possible to recover information about the line-of-sight geometry of the pressure distribution using SZ data only, the main assumption in the computations in this thesis of the thermal SZ signal from an ellipsoidal cluster consists in considering two of the principal axes to lie on the plane of the sky and the other to be aligned with the line-of-sight direction. Furthermore, the extent of the latter is hard-coded with the assumption that it is equal to the inverse root mean square average of the plane-of-sky semi-axes. It follows

$$\xi = \frac{1}{r_{\rm s}} \left(r_{\rm a}^2 + \frac{1}{1-\varepsilon^2} r_{\rm b}^2 + \frac{1}{2} \frac{2-\varepsilon^2}{1-\varepsilon^2} r_{\rm c}^2 \right)^{1/2}, \tag{B.1}$$

where $r_{\rm a}$, $r_{\rm b}$, and $r_{\rm c}$ are the radii measured along the three principal axes of the ellipsoid, respectively, and ε is the eccentricity of the elliptical profile projected on the sky. If one denotes with δ_0 the position angle of the plane-of-sky major axis taken from north through east, it is possible to write

$$\begin{aligned} r_{\rm a} &= (x - x_0)\, \cos y_0\, \cos \delta_0 - (y - y_0)\, \sin \delta_0 \\ r_{\rm b} &= (x - x_0)\, \cos y_0\, \sin \delta_0 + (y - y_0)\, \cos \delta_0 \\ r_{\rm c} &= z - z_0, \end{aligned} \tag{B.2}$$

where $(x - x_0)$, $(y - y_0)$ and $(z - z_0)$ are differences in the right ascension, declination and line-of-sight distance of a given point with respect to the centre of the ellipsoidal profile with coordinates (x_0, y_0, z_0).

Appendix C

Expected SZ significance in a radio-interferometric observation

The plot in Figure 5.1 provides a prediction of the integration time required to achieve an integrated detection significance of 5σ for an ACA observation of the SZ effect from a galaxy cluster over a representative range of redshift and masses. Here, I briefly discuss a few key details.

The estimate of the significance level for given cluster mass, redshift, and observing time is obtained by minimising the χ^2 equation for the interferometric data with respect to a normalisation parameter A, representing the relative uncertainties on the reconstructed model normalisation,

$$\chi^2 = \sum_i w_i \left| V_i - A M_i \right|^2 . \tag{C.1}$$

Here, the sum runs over all the visibility points V_i of a given interferometric measurement, with statistical weights $w_i = 1/\sigma_i^2$ for a noise root-mean-square σ_i, and where the term M_i is assumed to represent an accurate model of the observed SZ effect. By definition, A is expected to have unitary expectation value, and its standard deviation provides. The significance level of the SZ signal $\sigma_{\rm SZ}$ is then simply obtained as the inverse of the standard deviation of the normalisation parameter A over a set of realisations of the measure process,

$$\sigma_{\rm SZ} = \langle |A - 1|^2 \rangle^{-1/2}. \tag{C.2}$$

where A follows from the minimization of the χ^2 equation,

$$A = \frac{\sum_i w_i V_i M_i}{\sum_i w_i M_i^2}. \tag{C.3}$$

In practice, $\sigma_{\rm SZ}$ is estimated by bootstrapping over several hundred realisations of an inteferometric observation of a galaxy cluster. The mock SZ signal is first computed by integrating a fiducial pressure model, and then projected onto the mock visibility data as detailed in Appendix A. Although the predictions shown in Figure 5.1 are consistent with the results presented in Chapter 4 and other studies (see, e.g., Gobat et al. 2019), there are a few caveats that are worth discussing:

- the pressure distribution model used to produce the map of the SZ signal for a cluster at a given redshift and of a given mass is described by a universal pressure profile of Arnaud et al. (2010). However, galaxy clusters may exhibit average pressure profiles that deviate from the universal assumption, e.g., due to the presence of a prominent cool core or if a cluster is undergoing a merger, or a result of potential evolution with the cluster redshift. In such scenarios, the resulting SZ signal may populate different uv-modes than the universal case, hence affecting the total SZ effect measured by the radio-interferometer.

- As already discussed in Chapter 4, the specific approach adopted for deriving the detection significance of a given observation SZ effect may have a major impact on the effective significance level one is able to measure.

- To maximise the amplitude of the SZ signal, the mock cluster is centred on the maximum of the primary beam pattern. Any offset between the centre of the field of view, i.e., where the antenna response is maximal, would however cause an effective reduction of the measured signal-to-noise ratio of a given system.

- The observation is assumed to be performed near transit. This produces a uv-coverage that is roughly circular. The result is a spatial response that is uniform in all directions, corresponding to a fairly circularly symmetric dirty beam. If a source is instead observed away from transit, the resulting uv-pattern would be elongated along the v axis. This may introduce an advantage for the observation of the SZ effect, as it would be possible to measure the signal over a broader range of uv-distances with the same array configuration. In particular, the resulting uv coverage would extend to spacings shorter than the one in case of an observation performed at transit. As more SZ flux at large scale would be recovered, this would then allow to get a better signal-to-noise ratio with the same observational set-up.

Bibliography

Abdulla, Z., Carlstrom, J. E., Mantz, A. B., et al. 2019, ApJ, 871, 195

Adam, R. et al. 2014, A&A, 569, A66

Adam, R. et al. 2015, A&A, 576, A12

Adam, R. et al. 2018a, A&A, 609, A115

Adam, R. et al. 2018b, A&A, 614, A118

Akamatsu, H., Gu, L., Shimwell, T. W., et al. 2016, A&A, 593, L7

Allen, S. W., Evrard, A. E., & Mantz, A. B. 2011, ARA&A, 49, 409

Allen, S. W., Schmidt, R. W., & Fabian, A. C. 2002, MNRAS, 335, 256

Andreon, S. 2015, A&A, 582, A100

Ansarifard, S., Rasia, E., Biffi, V., et al. 2020, A&A, 634, A113

Arévalo, P., Churazov, E., Zhuravleva, I., Forman, W. R., & Jones, C. 2016, ApJ, 818, 14

Arnaud, M. et al. 2010, A&A, 517, A92

Astropy Collaboration. 2018, AJ, 156, 123

Bahcall, N. A. & Cen, R. 1992, ApJ, 398, L81

Bahcall, N. A. & Fan, X. 1998, ApJ, 504, 1

Basu, K., Sommer, M., Erler, J., et al. 2016, ApJ, 829, L23

Battaglia, N., Bond, J. R., Pfrommer, C., & Sievers, J. L. 2012, ApJ, 758, 74

Becker, R. H., White, R. L., & Helfand, D. J. 1995, ApJ, 450, 559

Béthermin, M., Wu, H.-Y., Lagache, G., et al. 2017, A&A, 607, A89

Biffi, V., Borgani, S., Murante, G., et al. 2016, ApJ, 827, 112

Bleem, L. E., Bocquet, S., Stalder, B., et al. 2020, ApJS, 247, 25

Bleem, L. E., Stalder, B., de Haan, T., et al. 2015, ApJS, 216, 27

Bocquet, S., Dietrich, J. P., Schrabback, T., et al. 2019, ApJ, 878, 55

Bocquet, S., Saro, A., Dolag, K., & Mohr, J. J. 2016, MNRAS, 456, 2361

Böhringer, H. & Werner, N. 2010, A&A Rev., 18, 127

Bonafede, A. et al. 2018, MNRAS, 478, 2927

Bond, J. R., Kofman, L., & Pogosyan, D. 1996, Nature, 380, 603

Bracewell, R. 1978, The Fourier Transform and its Applications, 2nd edn. (Tokyo: McGraw-Hill Kogakusha, Ltd.)

Bracewell, R. N. 1958, Proceedings of the IRE, 46, 97

Bradač, M. et al. 2008, ApJ, 681, 187

Bradač, M., Clowe, D., Gonzalez, A. H., et al. 2006, ApJ, 652, 937

Brodwin, M., Greer, C. H., Leitch, E. M., et al. 2015, ApJ, 806, 26

Brownson, S., Maiolino, R., Tazzari, M., Carniani, S., & Henden, N. 2019, MNRAS, 490, 5134

Brüggen, M., Bykov, A., Ryu, D., & Röttgering, H. 2012, Space Sci. Rev., 166, 187

Brunetti, G. & Jones, T. W. 2014, International Journal of Modern Physics D, 23, 1430007

Bryan, S., Austermann, J., Ferrusca, D., et al. 2018, in Society of Photo-Optical Instrumentation Engineers (SPIE) Conference Series, Vol. 10708, eds. Proc. SPIE Conf. Ser. Vol. 10708, Millimeter, Submillimeter, and Far-Infrared Detectors and Instrumentation for Astronomy IX. SPIE, Bellingham, 107080J

Bulbul, E., Chiu, I. N., Mohr, J. J., et al. 2019, ApJ, 871, 50

Bykov, A. M., Churazov, E. M., Ferrari, C., et al. 2015, Space Sci. Rev., 188, 141

Carilli, C. L., Harris, D. E., Pentericci, L., et al. 2002, ApJ, 567, 781

Carlstrom, J. E., Holder, G. P., & Reese, E. D. 2002, ARA&A, 40, 643

Carlstrom, J. E., Joy, M., & Grego, L. 1996, ApJ, 456, L75

Challinor, A. & Lasenby, A. 1998, ApJ, 499, 1

Chluba, J., Dai, L., & Kamionkowski, M. 2014, MNRAS, 437, 67

Chluba, J., Nagai, D., Sazonov, S., & Nelson, K. 2012, MNRAS, 426, 510

Churazov, E., Arevalo, P., Forman, W., et al. 2016, MNRAS, 463, 1057

Churazov, E., Forman, W., Jones, C., & Böhringer, H. 2000, A&A, 356, 788

Churazov, E., Forman, W., Jones, C., & Böhringer, H. 2003, ApJ, 590, 225

Churazov, E., Vikhlinin, A., & Sunyaev, R. 2015, MNRAS, 450, 1984

Clowe, D., Bradač, M., Gonzalez, A. H., et al. 2006, ApJ, 648, L109

Cohen, J. G. & Kneib, J.-P. 2002, ApJ, 573, 524

Colafrancesco, S., Marchegiani, P., & Palladino, E. 2003, A&A, 397, 27

Condon, J. J. 1974, ApJ, 188, 279

Condon, J. J., Cotton, W. D., Greisen, E. W., et al. 1998, AJ, 115, 1693

Condon, J. J. & Ransom, S. M. 2016, Essential Radio Astronomy (Princeton University Press)

Cornwell, T. J. 2008, IEEE Journal of Selected Topics in Signal Processing, 2, 793

Decker, B., Brodwin, M., Abdulla, Z., et al. 2019, ApJ, 878, 72

Di Francesco, J., Johnstone, D., Matthews, B. C., et al. 2013, arXiv e-prints, arXiv:1310.1604

Dicker, S. R. et al. 2014, J. Low Temp. Phys., 176, 808

Eckert, D., Ettori, S., Coupon, J., et al. 2016, A&A, 592, A12

Enßlin, T. A. & Kaiser, C. R. 2000, A&A, 360, 417

Erler, J., Basu, K., Chluba, J., & Bertoldi, F. 2018, MNRAS, 476, 3360

Ettori, S. 2000, MNRAS, 311, 313

Evrard, A. E. 1997, MNRAS, 292, 289

Fabian, A. C. 1994, ARA&A, 32, 277

Fabian, A. C. 2012, ARA&A, 50, 455

Fazio, G. G., Hora, J. L., Allen, L. E., et al. 2004, ApJS, 154, 10

Feretti, L. & Giovannini, G. 2008, Clusters of Galaxies in the Radio: Relativistic Plasma and ICM/Radio Galaxy Interaction Processes, ed. M. Plionis, O. López-Cruz, & D. Hughes, Vol. 740, 24

Feretti, L., Giovannini, G., Govoni, F., & Murgia, M. 2012, A&A Rev., 20, 54

Feroz, F., Hobson, M. P., Zwart, J. T. L., Saunders, R. D. E., & Grainge, K. J. B. 2009, MNRAS, 398, 2049

Ferrari, C. et al. 2011, A&A, 534, L12

Fixsen, D. J. 2009, ApJ, 707, 916

Foreman-Mackey, D. et al. 2013, PASP, 125, 306

Forman, W., Kellogg, E., Gursky, H., Tananbaum, H., & Giacconi, R. 1972, ApJ, 178, 309

Fox, D. C. & Loeb, A. 1997, ApJ, 491, 459

Frigo, M. & Johnson, S. G. 2012, Astrophysics Source Code Library

Fusco-Femiano, R. & Lapi, A. 2014, ApJ, 783, 76

Gaspari, M. & Churazov, E. 2013, A&A, 559, A78

Geach, J. E. & Peacock, J. A. 2017, Nature Astronomy, 1, 795

Gitti, M., Brighenti, F., & McNamara, B. R. 2012, Advances in Astronomy, 2012, 950641

Gitti, M., Ferrari, C., Domainko, W., Feretti, L., & Schindler, S. 2007, A&A, 470, L25

Gitti, M. & Schindler, S. 2004, A&A, 427, L9

Gobat, R., Daddi, E., Coogan, R. T., et al. 2019, A&A, 629, A104

Gonzalez, A. H., Decker, B., Brodwin, M., et al. 2015, ApJ, 812, L40

Gonzalez, A. H., Gettings, D. P., Brodwin, M., et al. 2019, ApJS, 240, 33

Gonzalez, A. H., Sivanandam, S., Zabludoff, A. I., & Zaritsky, D. 2013, ApJ, 778, 14

Goodman, J. & Weare, J. 2010, Comm. App. Math. Comp. Sci., 5, 65

Gott, J. R., I. & Rees, M. J. 1975, A&A, 45, 365

Grainge, K., Jones, M., Pooley, G., Saunders, R., & Edge, A. 1993, MNRAS, 265, L57

Gu, L., Zhuravleva, I., Churazov, E., et al. 2018, Space Sci. Rev., 214, 108

Halverson, N. W., Lanting, T., Ade, P. A. R., et al. 2009, ApJ, 701, 42

Hasselfield, M., Hilton, M., Marriage, T. A., et al. 2013, J. Cosmology Astropart. Phys., 2013, 008

Higson, E., Handley, W., Hobson, M., & Lasenby, A. 2017, arXiv e-prints, arXiv:1704.03459

Hilton, M., Hasselfield, M., Sifón, C., et al. 2018, ApJS, 235, 20

Hobson, M. P., Bridle, S. L., & Lahav, O. 2002, MNRAS, 335, 377

Hobson, M. P., Lasenby, A. N., & Jones, M. 1995, MNRAS, 275, 863

Hobson, M. P. & Maisinger, K. 2002, MNRAS, 334, 569

Högbom, J. A. 1974, A&AS, 15, 417

Huang, N., Bleem, L. E., Stalder, B., et al. 2020, AJ, 159, 110

Huang, Y. D. T., Morata, O., Koch, P. M., et al. 2016, Society of Photo-Optical Instrumentation Engineers (SPIE) Conference Series, Vol. 9911, The Atacama Large Millimeter/sub-millimeter Array band-1 receiver, 99111V

Humphreys, E., Miura, R., Brogan, C. L., et al. 2016, in Proceedings of the 2016 ALMA Conference, 1

Hurier, G., Macías-Pérez, J. F., & Hildebrandt, S. 2013, A&A, 558, A118

Iguchi, S., Morita, K.-I., Sugimoto, M., et al. 2009, PASJ, 61, 1

Itoh, N., Kohyama, Y., & Nozawa, S. 1998, ApJ, 502, 7

Itoh, N. & Nozawa, S. 2004, A&A, 417, 827

Jackson, J. I., Meyer, C. H., Nishimura, D. G., & Macovski, A. 1991, IEEE Transactions on Medical Imaging, 10, 473

Jeffreys, H. 1961, Theory of Probability, 3rd edn. (Oxford, England: Oxford)

Johnson, R. E., Zuhone, J., Jones, C., Forman, W. R., & Markevitch, M. 2012, ApJ, 751, 95

Jones, M., Saunders, R., Alexander, P., et al. 1993, Nature, 365, 320

Köhlinger, F. & Schmidt, R. W. 2014, MNRAS, 437, 1858

Kaiser, N. 1986, MNRAS, 222, 323

Kawabe, R., Kohno, K., Tamura, Y., et al. 2016, in Proc. SPIE, Vol. 9906, Ground-based and Airborne Telescopes VI, 990626

Kellogg, E., Gursky, H., Tananbaum, H., Giacconi, R., & Pounds, K. 1972, ApJ, 174, L65

Keshet, U. & Naor, Y. 2016, ApJ, 830, 147

Khedekar, S., Churazov, E., Kravtsov, A., et al. 2013, MNRAS, 431, 954

Kitayama, T. 2014, Progress of Theoretical and Experimental Physics, 2014, 06B111

Kitayama, T., Ueda, S., Akahori, T., et al. 2020, PASJ, 72, 33

Kitayama, T. et al. 2016, PASJ, 68, 88

Klaassen, P., Mroczkowski, T., Bryan, S., et al. 2019, in BAAS, Vol. 51, 58

Knox, L., Holder, G. P., & Church, S. E. 2004, ApJ, 612, 96

Komatsu, E. et al. 2001, PASJ, 53, 57

Kompaneets, A. S. 1957, Soviet Phys. JETP, 4, 730

Korngut, P. M. et al. 2011, ApJ, 734, 10

Kravtsov, A. V. & Borgani, S. 2012, ARA&A, 50, 353

Kreisch, C. D., Machacek, M. E., Jones, C., & Rand all, S. W. 2016, ApJ, 830, 39

Lacy, M., Baum, S. A., Chandler, C. J., et al. 2020, PASP, 132, 035001

Lacy, M., Mason, B., Sarazin, C., et al. 2019, MNRAS, 483, L22

LaRoque, S. J., Bonamente, M., Carlstrom, J. E., et al. 2006, ApJ, 652, 917

Lin, K.-Y., Li, C.-T., Ho, P. T. P., et al. 2009, ApJ, 694, 1629

Lindner, R. R., Baker, A. J., Omont, A., et al. 2011, ApJ, 737, 83

Lu, T. et al. 2010, MNRAS, 403, 1787

Madhavacheril, M. S., Hill, J. C., Naess, S., et al. 2019, arXiv e-prints, arXiv:1911.05717

Markevitch, M. 2006, in ESA Special Publication, Vol. 604, The X-ray Universe 2005, ed. A. Wilson, 723

Markevitch, M., Gonzalez, A. H., Clowe, D., et al. 2004, ApJ, 606, 819

Markevitch, M., Gonzalez, A. H., David, L., et al. 2002, ApJ, 567, L27

Markevitch, M. & Vikhlinin, A. 2007, Phys. Rep., 443, 1

Marriage, T. A., Acquaviva, V., Ade, P. A. R., et al. 2011, ApJ, 737, 61

Martí-Vidal, I., Vlemmings, W. H. T., Muller, S., & Casey, S. 2014, A&A, 563, A136

Mason, B. S. et al. 2010, ApJ, 716, 739

Mazzotta, P. & Giacintucci, S. 2008, ApJ, 675, L9

McDonald, M., Benson, B. A., Vikhlinin, A., et al. 2014, ApJ, 794, 67

McMullin, J. P., Waters, B., Schiebel, D., Young, W., & Golap, K. 2007, in Astronomical Society of the Pacific Conference Series, Vol. 376, Astronomical Data Analysis Software and Systems XVI, ed. R. A. Shaw, F. Hill, & D. J. Bell, 127

McNamara, B. R. & Nulsen, P. E. J. 2007, ARA&A, 45, 117

McNamara, B. R. & Nulsen, P. E. J. 2012, New Journal of Physics, 14, 055023

Merloni, A., Predehl, P., Becker, W., et al. 2012, arXiv e-prints, arXiv:1209.3114

Miley, G. & De Breuck, C. 2008, A&A Rev., 15, 67

Miley, G. K., Overzier, R. A., Zirm, A. W., et al. 2006, ApJ, 650, L29

Miranda, M., Sereno, M., de Filippis, E., & Paolillo, M. 2008, MNRAS, 385, 511

Moffet, A. T. & Birkinshaw, M. 1989, AJ, 98, 1148

Moravec, E., Gonzalez, A. H., Stern, D., et al. 2019, ApJ, 871, 186

Moravec, E., Gonzalez, A. H., Stern, D., et al. 2020, ApJ, 888, 74

Mroczkowski, T. 2011, ApJ, 728, L35

Mroczkowski, T., Nagai, D., Andreani, P., et al. 2019a, in BAAS, Vol. 51, 124

Mroczkowski, T., Nagai, D., Basu, K., et al. 2019b, Space Sci. Rev., 215, 17

Mroczkowski, T. et al. 2009, ApJ, 694, 1034

Muchovej, S., Mroczkowski, T., Carlstrom, J. E., et al. 2007, ApJ, 663, 708

Mukhanov, V. 2005, Physical Foundations of Cosmology

Nagai, D., Kravtsov, A. V., & Vikhlinin, A. 2007, ApJ, 668, 1

Nelson, K., Lau, E. T., Nagai, D., Rudd, D. H., & Yu, L. 2014, ApJ, 782, 107

Ota, N. et al. 2008, A&A, 491, 363

Overzier, R. A. 2016, A&A Rev., 24, 14

Paraficz, D., Kneib, J.-P., Richard, J., et al. 2016, A&A, 594, A121

Peebles, P. J. E. 1980, The large-scale structure of the universe

Perrott, Y. C., Javid, K., Carvalho, P., et al. 2019, MNRAS, 486, 2116

Pillepich, A., Porciani, C., & Reiprich, T. H. 2012, MNRAS, 422, 44

Plagge, T. J. et al. 2013, ApJ, 770, 112

Planck Collaboration V. 2013, A&A, 550, A131

Planck Collaboration I. 2016, A&A, 594, A1

Planck Collaboration XIII. 2016, A&A, 594, A13

Planck Collaboration XXII. 2016, A&A, 594, A22

Planck Collaboration XXVII. 2016, A&A, 594, A27

Pointecouteau, E., Giard, M., & Barret, D. 1998, A&A, 336, 44

Pointecouteau, E., Giard, M., Benoit, A., et al. 2001, ApJ, 552, 42

Pratt, G. W., Arnaud, M., Biviano, A., et al. 2019, Space Sci. Rev., 215, 25

Press, W. H., Flannery, B. P., Teukolsky, S. A., & Vetterling, W. T. 1989, Numerical recipes in C. The art of scientific computing

Press, W. H. & Schechter, P. 1974, ApJ, 187, 425

Randall, S. W., Markevitch, M., Clowe, D., Gonzalez, A. H., & Bradač, M. 2008, ApJ, 679, 1173

Reese, E. D., Mohr, J. J., Carlstrom, J. E., et al. 2000, ApJ, 533, 38

Remazeilles, M., Delabrouille, J., & Cardoso, J.-F. 2011, MNRAS, 410, 2481

Rephaeli, Y. 1995, ARA&A, 33, 541

Rettura, A., Chary, R., Krick, J., & Ettori, S. 2018, ApJ, 867, 12

Ricker, P. M. & Sarazin, C. L. 2001, ApJ, 561, 621

Romero, C. E., Sievers, J., Ghirardini, V., et al. 2020, ApJ, 891, 90

Romero, C. E. et al. 2015, ApJ, 807, 121

Romero, C. E. et al. 2018, A&A, 612, A39

Ruppin, F., Mayet, F., Macías-Pérez, J. F., & Perotto, L. 2019a, MNRAS, 490, 784

Ruppin, F., McDonald, M., Brodwin, M., et al. 2020, ApJ, 893, 74

Ruppin, F., Sembolini, F., De Petris, M., et al. 2019b, A&A, 631, A21

Ruppin, F. et al. 2017, A&A, 597, A110

Russell, H. R., McNamara, B. R., Sanders, J. S., et al. 2012, MNRAS, 423, 236

Rybicki, G. B. & Lightman, A. P. 1979, Radiative processes in astrophysics

Rykoff, E. S., Koester, B. P., Rozo, E., et al. 2012, ApJ, 746, 178

Sarazin, C. L. 1986, Reviews of Modern Physics, 58, 1

Saro, A., Bocquet, S., Rozo, E., et al. 2015, MNRAS, 454, 2305

Saro, A., Borgani, S., Tornatore, L., et al. 2009, MNRAS, 392, 795

Sayers, J., Montaña, A., Mroczkowski, T., et al. 2019, ApJ, 880, 45

Sayers, J. et al. 2013, ApJ, 768, 177

Sayers, J. et al. 2016a, ApJ, 832, 26

Sayers, J. et al. 2016b, ApJ, 820, 101

Sazonov, S. Y. & Sunyaev, R. A. 1998, Astronomy Letters, 24, 553

Schindler, S., Hattori, M., Neumann, D. M., & Boehringer, H. 1997, A&A, 317, 646

Schindler, S. et al. 1995, A&A, 299, L9

Sehgal, N., Aiola, S., Akrami, Y., et al. 2019, in BAAS, Vol. 51, 6

Sembolini, F., De Petris, M., Yepes, G., et al. 2014, MNRAS, 440, 3520

Sereno, M., Ettori, S., & Baldi, A. 2012, MNRAS, 419, 2646

Shandarin, S. F. & Zeldovich, Y. B. 1989, Reviews of Modern Physics, 61, 185

Shi, X., Komatsu, E., Nelson, K., & Nagai, D. 2015, MNRAS, 448, 1020

Shimwell, T. W., Markevitch, M., Brown, S., et al. 2015, MNRAS, 449, 1486

Shinnaga, H., Humphreys, E., Indebetouw, R., et al. 2015, in Astronomical Society of the Pacific Conference Series, Vol. 499, Revolution in Astronomy with ALMA: The Third Year, ed. D. Iono, K. Tatematsu, A. Wootten, & L. Testi, 355

Shitanishi, J. A. et al. 2018, MNRAS, 481, 749

Silk, J. 1968, ApJ, 151, 459

Simionescu, A., Allen, S. W., Mantz, A., et al. 2011, Science, 331, 1576

Speagle, J. S. 2020, MNRAS, 493, 3132

Spitzer, L. 1962, Physics of Fully Ionized Gases

Springel, V. & Farrar, G. R. 2007, MNRAS, 380, 911

Stanimirovic, S. 2002, in ASP Conf. Ser., Vol. 278, Single-Dish Radio Astronomy: Techniques and Applications, ed. S. Stanimirovic et al., Astron. Soc. Pac., San Francisco, 375–396

Sunyaev, R. A. & Zeldovich, I. B. 1980, MNRAS, 190, 413

Sunyaev, R. A. & Zeldovich, Y. B. 1972, Comments on Astrophysics and Space Physics, 4, 173

Tadhunter, C. 2016, A&A Rev., 24, 10

Tazzari, M., Beaujean, F., & Testi, L. 2018, MNRAS, 476, 4527

Tchernin, C., Eckert, D., Ettori, S., et al. 2016, A&A, 595, A42

Thompson, A. R., Moran, J. M., & Swenson, G. W. 1986, Interferometry and Synthesis in Radio Astronomy (Wiley-Interscience, New York), 000–000

Thompson, R., Davé, R., & Nagamine, K. 2015, MNRAS, 452, 3030

Trotta, R. 2008, Contemporary Physics, 49, 71

Tulin, S. & Yu, H.-B. 2018, Phys. Rep., 730, 1

Ueda, S., Kitayama, T., & Dotani, T. 2017, ApJ, 837, 34

Ueda, S. et al. 2018, ApJ, 866, 48

van Cittert, P. H. 1934, Physica, 1, 201

van Velzen, S., Falcke, H., & Körding, E. 2015, MNRAS, 446, 2985

van Weeren, R. J., de Gasperin, F., Akamatsu, H., et al. 2019, Space Sci. Rev., 215, 16

Verdugo, M., Lerchster, M., Böhringer, H., et al. 2012, MNRAS, 421, 1949

Vikhlinin, A., Forman, W., & Jones, C. 1997, ApJ, 474, L7

Vikhlinin, A., Kravtsov, A. V., Burenin, R. A., et al. 2009, ApJ, 692, 1060

Vikhlinin, A. A., Kravtsov, A. V., Markevich, M. L., Sunyaev, R. A., & Churazov, E. M. 2014, Physics Uspekhi, 57, 317

Vink, J., Broersen, S., Bykov, A., & Gabici, S. 2015, A&A, 579, A13

Voges, W. et al. 1999, A&A, 349, 389

Voit, G. M. 2005, Reviews of Modern Physics, 77, 207

Walker, S., Simionescu, A., Nagai, D., et al. 2019, Space Sci. Rev., 215, 7

Wallis, K. F. 2014, Statist. Sci., 29, 106

Wang, Q. H. S., Giacintucci, S., & Markevitch, M. 2018, ApJ, 856, 162

White, S. D. M. & Frenk, C. S. 1991, ApJ, 379, 52

White, S. D. M., Navarro, J. F., Evrard, A. E., & Frenk, C. S. 1993, Nature, 366, 429

White, S. D. M. & Rees, M. J. 1978, MNRAS, 183, 341

Wik, D. R., Sarazin, C. L., Ricker, P. M., & Rand all, S. W. 2008, ApJ, 680, 17

Wittman, D., Golovich, N., & Dawson, W. A. 2018, ApJ, 869, 104

Wootten, A. & Thompson, A. R. 2009, IEEE Proceedings, 97, 1463

Wright, E. L. 1979, ApJ, 232, 348

Wright, E. L., Eisenhardt, P. R. M., Mainzer, A. K., et al. 2010, AJ, 140, 1868

Wrobel, J. M. & Walker, R. C. 1999, in ASP Conf. Ser., Vol. 180, Synthesis Imaging in Radio Astronomy II, ed. G. B. Taylor, C. L. Carilli, & R. A. Perley, Astron. Soc. Pac., San Francisco, 171

Yagoubov, P., Mroczkowski, T., Belitsky, V., et al. 2020, A&A, 634, A46

Yu, L., Nelson, K., & Nagai, D. 2015, ApJ, 807, 12

Zeldovich, Y. B. & Raizer, Y. P. 1966, Elements of gasdynamics and the classical theory of shock waves

Zeldovich, Y. B. & Sunyaev, R. A. 1969, Ap&SS, 4, 301

Zemcov, M., Aguirre, J., Bock, J., et al. 2012, ApJ, 749, 114

Zernike, F. 1938, Physica, 5, 785

Zhang, C., Churazov, E., Forman, W. R., & Jones, C. 2019, MNRAS, 482, 20

Zhang, C., Yu, Q., & Lu, Y. 2015, ApJ, 813, 129

Zhang, C., Yu, Q., & Lu, Y. 2018, ApJ, 855, 36

Zhuravleva, I., Churazov, E., Arévalo, P., et al. 2016, MNRAS, 458, 2902

Zitrin, A., Fabris, A., Merten, J., et al. 2015, ApJ, 801, 44

ZuHone, J. A., Markevitch, M., Brunetti, G., & Giacintucci, S. 2013, ApJ, 762, 78

Zuhone, J. A. & Roediger, E. 2016, Journal of Plasma Physics, 82, 535820301

Zwart, J. T. L., Barker, R. W., Biddulph, P., et al. 2008, MNRAS, 391, 1545

Acknowledgments

To Eugene, my advisor. For finding a moment every time I knocked at your door, for the immeasurable patience in guiding me through all my mistakes and for allowing me the freedom to make those. From you I learned how to look for new questions after every answer.

To Tony, my half-supervisor. For teaching me how to see the world in Fourier space, for relentlessly supporting me, for all the coffee breaks, more than often taking too much of our time. Thanks a lot for adopting me, and showing me how human and kind this crazy academic world could be. To you goes my sincere gratitude.

To Rashid. It has been a real privilege to walk my first scientific steps with you. Thank you for your enduring enthusiasm for my work, it has meant a lot to me.

To Chiara, Cristiano, Elena, Giulia, Luca, Simona. For listening to my never-ending chatters, for the one-man concerts, the hipster movies, Sanremo. Thanks for always being there for me, despite I constantly stood you up. *Daje, ci*!

To Luigi, my life-long friend. No matter of the distance between us, I know that having your hotel sleepers around my place will always make me feel I am your Sandra, you my Raimondo.

To Dalida and Elio, my parents. For being understanding, encouraging, and supportive, way more than I could have ever expected. For the smiles on the other side of the screen, the long awaited embraces, the fights.

To Francesca, my everything, for everything. For making me question my certainties and find in you new ones, for setting my thoughts and my heavy heart free, for teaching me not to be happy with “anything less than hundred percent".

Grazie.